A Thermally and Mechanically Stable Structure For XRIstel, the X-Ray Interferometric Space Telescope

MSc Thesis

Joran Blom

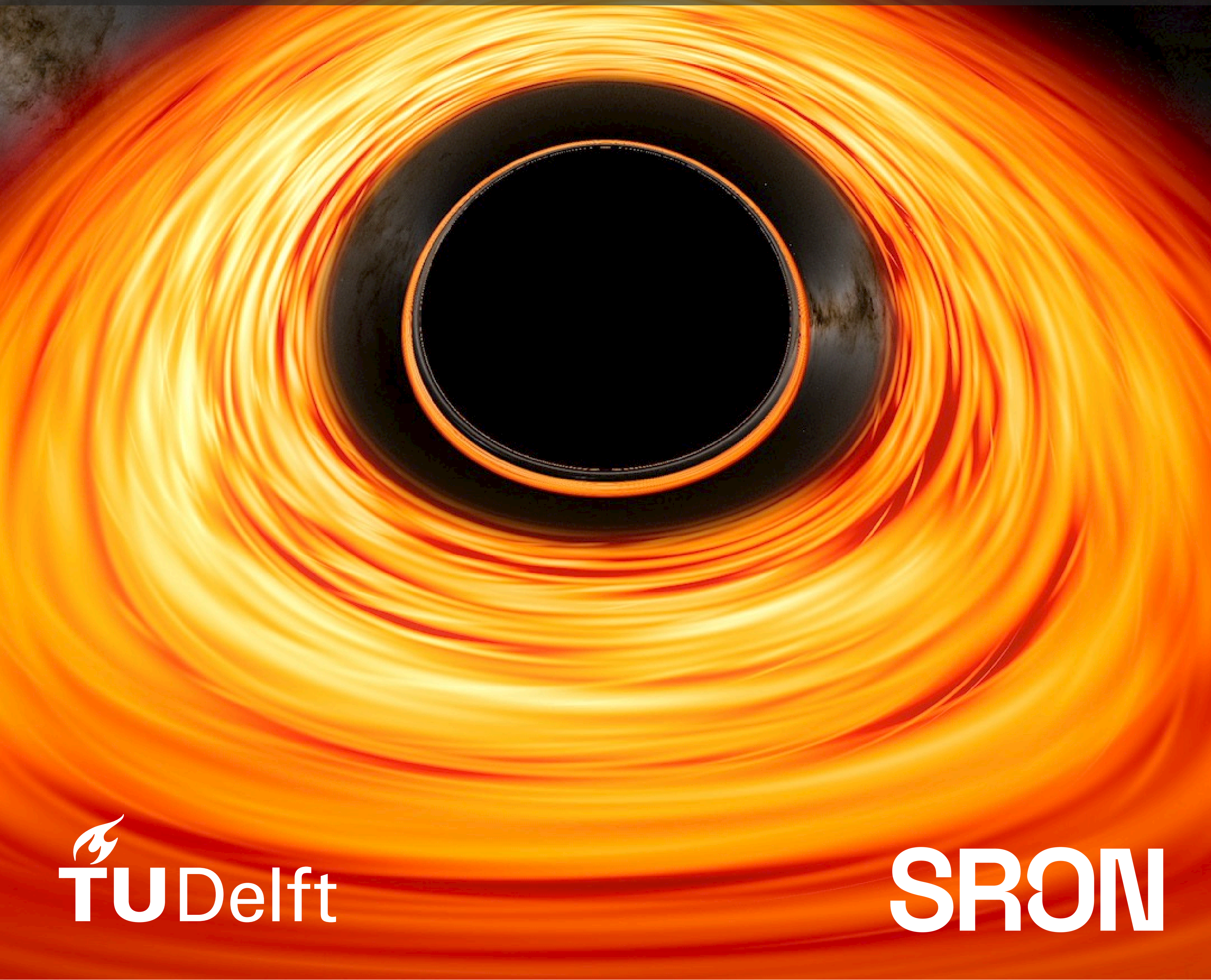

A Thermally and Mechanically Stable Structure For XRIstel, the X-Ray Interferometric Space Telescope

by

Joran Blom

to obtain the degree of Master of Science
at the Delft University of Technology,
to be defended publicly on Friday September 4, 2026 at 10:00 AM.

Student number:	5872898	
Project duration:	January, 2026 – September, 2026	
Organisation:	SRON – Space Research Organisation Netherlands	
Faculty:	Aerospace Engineering, Delft	
Thesis committee:	Dr. I. Akay,	TU Delft, responsible supervisor
	Dr. J. Bouwmeester,	TU Delft, committee chair
	Dr. D.M.J. Peeters,	TU Delft, external examiner
	Dr. R. den Hartog,	SRON, external examiner

Cover: Scientific accurate black hole visualization resulting from months of work of the team led by Jeremy Schnittman at NASA's Goddard Space Flight Center in Greenbelt, Maryland. Image Credit: NASA

An electronic version of this thesis is available at `http://repository.tudelft.nl/`.

TU Delft SRON

Preface

As part of my MSc Aerospace Engineering degree, I took part in an external thesis at Space Research Organisation Netherlands (SRON). Over the course of eight months, from January 2026 till September 2026, I had the opportunity to be part of the XRIstel mission at SRON. Being able to use my engineering knowledge at an institute like SRON, in a team that is working on the future of space observatories, is the chance that I had been looking for.

During my thesis, I have made use of many tools, including COMSOL Multiphysics for modelling and different types of analyses. Python for initial concept generation, material calculations, and implementation of analytical comparisons, and Latex for writing my thesis. For the sake of transparency, I think it is important to note the usage of Artificial Intelligence (AI) tools in an ever-growing AI interwoven society. Additional to the above-mentioned software, I have used tools such as ChatGPT, Gemini, and Claude for Latex/Overleaf support, with Gemini also utilized for COMSOL/Python specific debugging. Lastly, NotebookLM has been utilized to extract information from specific sources. To add to this, any use of AI tools have been merely in a supporting capacity. Hence, every word within this thesis is my own and AI has not been part of any conceptual or critical elements of this thesis.

The results of this thesis would not have been possible if not for many great colleagues, discussions, presentations, and supervision from within SRON and the TU Delft. Therefore, in the first place I would like to extend my appreciation to Dr. Roland den Hartog and Dr. Iklim Akay, who have both supervised me throughout these eight months. The bi-weekly meetings with Iklim have provided me valuable feedback on the thesis progress and on technical details. I would like to thank the entire XRIstel team, Roland den Hartog, Henk Hoevers, Phil Uttley, Aditya Garde, Philipp Stöcker, and Daan Peeters for the insightful weekly meetings to support my thesis, while educating me about the many more aspects regarding X-ray interferometry. Throughout these meetings and discussion, I have learned a lot more about engineering, physics, astronomy, and about general mission development. To enable me to use the DelftBlue High-Performance Computing (HPC) center, I would like to thank the entire DelftBlue team, but especially Dr. Dennis Palagin, who spent time and effort to help me with installing the right software on DelftBlue, allowing me to run detailed simulations. Lastly, my appreciation also goes out to the engineering department for allowing me to present my work during their weekly meeting and providing me with valuable feedback and insights.

Joran Blom
Leiden, August 2026

Abstract

The X-Ray Interferometric Space Telescope (XRIstel) is a proposed single-spacecraft mission designed for high-resolution astrophysics. It targets angular resolutions on the order of 100 µas, representing an $O(10^4)$ spatial resolution improvement over existing X-ray observatories. This capability enables direct imaging and spectro-astrometric observations of compact sources, such as supermassive black holes (SMBHs) and X-ray binaries. Operating in a Lissajous orbit around the Sun-Earth L2 point, the spacecraft undergoes a controlled rolling motion, while its optical payload relies on grazing-incidence and slatted beam combining mirrors operating at wavelengths between 1.24 and 8.68 nm.

Maintaining interference fringe visibility requires optical path length differences between optics and detector to remain within 0.1 to 1.0 nm. Conventional spacecraft structures prioritize strength and stiffness, but lack sub-nanometer thermo-mechanical stability. This study addresses the design and evaluation of an ultra-stable primary structure for XRIstel. The objective is to achieve sub-nanometer stability while satisfying Ariane 6 launch constraints, mass envelopes, and outgassing limitations.

Building on design approaches from heritage missions like LISA and JWST, a Python framework was developed for conceptual structural sizing. The tool evaluated candidate beam geometries, global topologies, and materials, including CFRP laminates, C/C-SiC, Aluminium 7075-T6, and CF/PEEK. Classical Laminate Theory (CLT) was applied to determine the quasi-isotropic properties for composite laminates. Candidate concepts were then modelled in COMSOL Multiphysics using (mostly) shell elements. Finite element simulations evaluated static launch accelerations, linear buckling stability, natural frequencies, thermal environment behaviour, sinusoidal excitation responses, and micrometeoroid impact analyses.

Thin-walled circular beams demonstrated superior behaviour compared to octagonal beam profiles, while a CFRP material consisting of Toray M40J fibres and PMT-F33 cyanate ester resin outperformed other material candidates. A multi-criteria trade-off identified an eight-beam CFRP structure with five support rings as the optimal baseline for detailed design. The concept yielded mass savings while meeting the strict outgassing requirements and launch constraints. A detailed design was developed, including further parameter refinements on wall thicknesses, beam diameters, number of support rings, additional support structures (local and global) such as diagonal beams, cross-volume structures, and the inclusion of multi-layer insulation and solar panels.

Detailed design analyses identify the multi-octagon structural configuration (MO-BR) as the best performing structure, fully satisfying launch survivability with margin and outperforming the single-octagon regarding all metrics. These include the stress levels, eigenfrequencies, total mass, CoG location, and sinusoidal excitation response. Nearly all requirements are satisfied, either fully or marginally, while the spacecraft lid design and the CFRP/aluminium connective joints are identified as a source remaining local stress concentrations and unwanted longitudinal response behaviour.

This study confirms the feasibility of developing a single-spacecraft XRI mission with an ultra-stable spacecraft structure based on CFRP as primary material. The optimized multi-octagon composite structure combines launch survivability with a realistic baseline for further development towards a sub-nanometer thermo-mechanical stable spacecraft.

Future steps of the structural design process are recommended to include the identification and evaluation of the thermal environment and the structure's response during operation. Additionally, the inclusion of optical benches, realistic connective joints, and a detailed spacecraft lid design are recommended in near-future design iterations.

Nomenclature

Abbreviations

Abbreviation	Definition	Abbreviation	Definition
AI	Artificial Intelligence	LOS	Line-of-Sight
AIT	Assembly, Integration, and Testing	LSI	Liquid Silicon Infiltration
AOCS	Attitude and Orbit Control System	LUVOIR	Large Ultraviolet Optical Infrared Surveyor
BAM	Basic Angle Monitoring	MLI	Multi-Layer Insulation
CBF	Critical Buckling Factor	MoS	Margin of Safety
CCD	Charge-Coupled Device	NASA	National Aeronautics and Space Administration
CFRP	Carbon-Fibre Reinforced Polymer	NTE	Negative Thermal Expansion
CLT	Classical Laminate Theory	OBM	Optical Bench Metrology
CoG	Center of Gravity	OPD	Optical Path Difference
CTE	Coefficient of Thermal Expansion	PEEK	Polyetheretherketon
CVCM	Collected Volatile Condensible Material	PMBSS	Primary Mirror Backplane Support Structure
ECSS	European Cooperation for Space Standardization	PSD	Power Spectral Density
EOF	End-Of-Flight	PSF	Point Spread Function
ESA	European Space Agency	RLG	Ring Laser Gyroscope
FEA	Finite Element Analysis	RML	Recovered Mass Loss
FEM	Finite Element Method	ROM	Rule of Mixtures
FEP	Fluorinated Ethylene Propylene	SMBH	Super-Massive Black Hole
FoS	Factor of Safety	SR	Soft Requirement
FOV	Field of View	SRON	Space Research Organisation Netherlands
Gaia	Global Astrometric Interferometer for Astrophysics	STOP	Structural-Thermal-Optical Performance
GAS	Geometric Anti-Spring	TA	Telescope Assembly
GFRP	Glass-Fibre Reinforced Polymer	TC	Thermal Conductivity
HR	Hard Requirements	TML	Total Mass Loss
HWO	Habitable World Observatory	UD	Uni-Directional
ISIM	Integrated Science Instrument Module	ULE	Ultra-Low Expansion
JWST	James Webb Space Telescope	UTS	Ultimate Tensile Strength
KDF	Knock-Down-Factor	XMM	X-ray Multi-Mirror
LISA	Laser Interferometer Space Antenna	XRI	X-Ray Interferometry
LORRI	Long Range Reconnaissance Imager	XRIstel	X-Ray Interferometric Space Telescope

Symbols

Symbol	Definition	Unit
α	Coefficient of thermal expansion	1/K
α_{abs}	Solar absorptivity	–
ε	Thermal emissivity	–
λ	Thermal conductivity	$W/(m \cdot K)$
ν	Poisson’s ratio	–
π	Mathematical constant	–
ρ	Density	kg/m^3
σ_c	Compressive strength	N/m^2
σ_t	Tensile strength	N/m^2
σ_u	Ultimate strength	N/m^2
σ_y	Yield strength	N/m^2
φ_{solid}	Solid volume fraction	–
ω_{spin}	Angular spin	rad/s

Contents

List of Figures

List of Tables

1 Introduction

Supermassive black holes (SMBHs) are among the most energetic and captivating objects in the universe. The physical processes occurring in these black holes and in their immediate vicinity is poorly understood, similarly to binary black hole systems and neutron stars. Improving the general understanding of accretion physics, jet formation, and binary behaviour is essential for scientific progress. Observations in X-rays are particularly interesting due to the large amounts of X-ray radiation originating from hot plasma near these objects. The X-Ray Interferometric Space Telescope (XRIstel) is a mission proposal that aims to use the vast X-ray expulsion of these objects through space-based X-ray interferometry on a single spacecraft. XRIstel aims to provide an $O(10^4)$ improvement in spatial resolution compared to current X-ray observatories.

Enabling these scientific goals imposes challenging requirements and constraints on the spacecraft design. Due to the space-based nature of the mission, the spacecraft is exposed to a challenging launch and a harsh thermal environment. The interferometric principle of XRIstel relies on extreme control and stability of the optical elements, making the dimensional stability in the thermo-mechanical environment a primary design driver. These thermo-mechanical instabilities due to temperature gradients, material behaviour, and structural interactions must be mitigated throughout operation. The spacecraft structure thus fulfils a dual-purpose, serving as primary load carrying structure, as well as support for the optical benches containing the optical assemblies.

The XRIstel mission is in early development stages, with key technologies still under investigation. Early development of the spacecraft structure is one of the natural next steps in the process, providing insights in possibilities and limitations of bringing XRI to space. Major hurdles for a spacecraft structure include launch survivability, and in this case, the extreme dimensional stability required for observations. This study focuses on the conceptual and preliminary design of the spacecraft structure, of which an earlier visualisation can be seen in Figure 1.1.

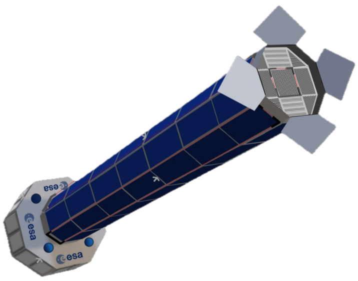

Figure 1.1: Initial visualization of the XRIstel spacecraft design. Image credits: Aditya Garde & Roland den Hartog

Based on the objective of this study, the primary research question can be formulated as: *How can a large spacecraft structure be designed to achieve ultra-high thermo-mechanical stability, while satisfying launch survivability, mass, and optical accessibility requirements?*

To answer this question, this study follows a structured design approach, with an initial literature review as first step. A derivation of system requirements and identification of main design drivers follows, after which multiple structural concepts are generated and evaluated during the conceptual design phase. The selected concept is further developed through more detailed design and analysis, after which its performance is verified against the mission requirements. Finally, conclusions and recommendations are based on the obtained insights and provide a pathway for future developments.

2
Research Scope

This chapter discusses several aspects of the research proposal, including a brief explanation of the general mission, the study specific problem statement, research objectives and questions, the scope, and an initial summary of the requirements.

2.1. XRI Space Telescope

The proposed X-ray mission, XRIstel, aims to develop a single-spacecraft X-ray interferometric space telescope capable of achieving angular resolutions in the order of 100 µas. This angular resolutions at X-ray wavelengths exceeds the performance of past, current, and planned X-ray observatories (Uttley et al. [1], Hartog [2]). As a proposed ESA Voyage 2050 M-class mission, its primary scientific objective is to enable direct imaging and spectro-astrometric measurements of extremely compact and energetic cosmic sources, such as accreting stellar-mass black holes, SMBHs, X-ray binaries, and neutron stars. Additionally, the mission serves as a demonstrator for key technologies required for future X-ray interferometric missions.

The mission concept is largely based around Willingale's compact interferometer design, discussed in Appendix A, which allows for a wide variety of baselines on a single spacecraft. The design utilizes grazing-incidence mirrors and slatted beam-combining mirrors (Uttley et al. [1], Hartog [2]), allowing interference fringes to form directly on a large-area detector without the need for multiple spacecrafts. Spatial information is sampled through multiple baselines during the spacecraft's controlled rolling motion, enabling image reconstruction through Fourier interferometric principles. Simulations demonstrate that such a mission could resolve stellar surfaces, accretion flows, and structures the size of event-horizon scales. The proposed spacecraft aims for an effective collecting area of at least 1500 cm^2, comparable to XMM-Newton.

The scientific objectives impose unique and stringent requirements on optical path length and pointing stability, as X-ray fringe visibility is highly sensitive to nanometer-scale optical path difference (OPD) variations and pointing jitter at the level of tens of µas (Uttley et al. [1], Hartog [2]). Pointing and dimensional stability are fundamentally inseparable, because the spacecraft attitude changes and baseline deformations produce equivalent fringe shifts on the detector. The derived absolute pointing knowledge requirement is approximately 20 picoradian, corresponding to mirror position variations of $\leqslant 1$ nm and a front-end spacecraft displacement of approximately 0.4 nm. Relative pointing errors must remain below 185 µas (0.9 nanoradians) for a minimum of 95% of the observation time.

At the current mission phase, the pointing knowledge and stability are considered the most critical technical challenges, exceeding the difficulty associated with mirror surface quality (Uttley et al. [1], Hartog [2]). Consequently, the attitude and orbit control system (AOCS) forms a critical element of the mission design, with ultra-high-precision ring laser gyroscopes (RLGs) identified as the sole sensor technology capable of meeting the required performance. Target gyroscope specifications include sensitives better than 20 prad/s in a 1 Hz bandwidth, noise levels below 10 prad/s/$\sqrt{\text{Hz}}$, and a bias stability better than 30 frad/s over 100 ks, with direct mechanical integration onto the optical benches (Hartog [2]).

Besides the scientific return, XRIstel is positioned as technology demonstrator for future X-ray interferometry missions. Demonstrating a stable single-spacecraft X-ray interferometer significantly reduces mission complexity in comparison to multi-spacecraft formation flying. Simultaneously, XRIstel will validate technologies such as ultra-stable structural integration of RLGs, precision alignment, high-precision attitude reconstruction, and in-flight X-ray interferometry.

2.2. Problem Statement

XRIstel's performance objectives impose stringent requirements on the spacecraft structure. Achieving an $O(10^4)$ improvement in spatial resolution requires extreme stability of the interferometry baselines and optical path lengths, aiming for deviations well below target wavelength. XRIstel utilizes a collection of soft/hard interferometers operating between 1 and 7 keV, corresponding to wavelengths of approximately 1.24 – 8.68 nm. Optical path differences between the entrance mirrors and detector must thus remain within 0.1 – 1 nm during fringe acquisition (100 – 1000 s). The spacecraft's structure acts primarily as load carrying structure, while also providing the interface between the spacecraft and the modular optical benches. Thermo-mechanical behaviour of the spacecraft structure acts as a set of boundary conditions imposed on the design and integration of the optical benches, with deformations affecting the design of the benches. At the same time, the structure must ensure that the spacecraft survives launch conditions and maintains a stability throughout the thermal environment at L2, while rotating with 2π per 1700 - 23400 seconds.

Conventional spacecraft structures are generally optimized for strength, stiffness, and minimized mass, but are not designed to maintain thermo-mechanical stability at the nanometer level. Previous missions requiring above-average stability include Gaia and LISA Pathfinder, which demonstrated that such performance requirements require specialized structural designs and careful thermo-mechanical coupling, while utilizing advanced materials. Conventional and novel materials may contribute to the realization of an ultra-stable structure, with heritage materials such as aluminium and carbon-fibre reinforced polymers (CFRP) offering well-known performance and manufacturing capabilities. Novel materials such as C/C-SiC represent a unique set of characteristics worth investigating.

The problem addressed in this study is the design of a large spacecraft structure that in the first place survives the launch environment, and also satisfies the stringent requirements. This process includes the determination of a suitable material. The performance of the structure is to be compared and verified against the imposed requirements to gain insights into the behaviour.

2.3. Research Objective, Questions, and Hypothesis

The research objective indicates the goal that naturally comes from the problem statement, and can thus be formulated as:

- **The primary objective of this research is to design and evaluate an ultra-stable spacecraft structure for the XRIstel mission that satisfies the launch survivability and mission constraints, while minimizing thermo-mechanical deformations during operation.**

Based on the objective of this study, research questions can be posed as following:

1. ***How can a large spacecraft structure be designed to achieve ultra-high thermo-mechanical stability, while satisfying launch survivability, mass, and optical accessibility requirements?***
    - What structural topology is most suitable for realizing an ultra-stable XRIstel spacecraft structure?
    - To what extent do joints and structural interfaces influence the structure's stability?
    - To what extent does the proposed structural design satisfy the imposed thermo-mechanical requirements and launch survivability?
2. ***To what extent can material selection enable a large ultra-stable spacecraft structure for the XRIstel mission?***
    - What material properties are most influential to the stability of the spacecraft structure?
    - How does material anisotropy affect the structural design and stability performance?

The following hypothesis is flowing from the literature review discussed in chapter 3, the above-mentioned research objectives, and the requirements discussed in section 2.4.

- **It is hypothesized that a spacecraft structure based on advanced composite materials, combined with an optimized structural configuration and a minimized need for connective joints, can satisfy the launch survivability, mass, and volume constraints of the XRIstel proposal while achieving the thermo-mechanical stability.**

2.4. Research Scope and Requirements

The scope that has been defined for design study is summarized in Table 2.1. Based on the project definition, the problem statement, and the stringent performance requirements of XRIstel, a summary of the requirements can be defined as shown in Table 2.2. Additional important requirements can be defined, but are not immediately related to this design study, they can be found in Table B.1

Table 2.1: Bullet point summary of the scope of this design study, including the main tasks that are part of this thesis.

Research component	**Included (Yes/No)**	**Additional remarks**
Literature review	Yes	Includes a review on relevant literature topics, clearly defining the state-of-the-art and knowledge gaps.
XRI structure design	Yes	Detailed structural configuration of the final iterations, including 3D models.
Thermal analysis	Yes	Includes computer-based simulation analyses of the thermal behaviour and stability of the final design, with analytical verification where possible.
Mechanical analysis	Yes	Includes computer-based simulation analyses of the mechanical behaviour and stability of the final design, with analytical verification where possible.
Vibrational analysis	Yes	Includes computer-based simulation analysis of sinusoidal excitation. Includes micrometeoroid impact analyses.
Selected material analysis	Yes	Includes a detailed evaluation of the selected structural material, highlighting the advantages and limitations of the material for ultra-stable spacecraft structures.
Spacecraft bus design	No	The geometry, properties, and specifications of the spacecraft bus are not included and are assumed to be fixed and generalized according to the provided documentation and internal discussion.
Solar panel design	No	The specifications, design, and properties of the solar panels are considered to be outside of the scope of this thesis. They will be treated as generalized components.
Optical element design	No	None of the optical elements or experimental components are within the scope of this study.
Optical element mounts	No	Connective structural elements bridging the structure and the optical benches and mirror assemblies are outside of the scope, as the optical benches are yet to be designed.
Structure cost estimate	No	The cost of the structure, manufacturing, and AIT is not within the scope of this study.

Table 2.2: System requirements and constraints for the XRIstel spacecraft structure. HR = Hard Requirement, SR = Soft Requirement.

ID	Title	Description
HR-001	Launch loads	The spacecraft must withstand an acceleration of 2.0 times the maximum launch acceleration. Ariane 6 user's manual dictates the launch environment, most extreme during the aerodynamic and end-of-flight (EOF) phases. EOF: maximum longitudinal acceleration of 6g with a ± 1.0g lateral acceleration. During aerodynamic phase, the maximum longitudinal acceleration is 3.6g with a ± 1.8g lateral acceleration (ArianeSpace [3]).
HR-002	Lateral frequencies	The fundamental frequency in the lateral axis of the spacecraft must be $\geqslant 6$ Hz with no secondary mode lower than the first primary mode (ArianeSpace [3]).
HR-003	Longitudinal frequencies	The fundamental frequency in the longitudinal axis of the spacecraft must be $\geqslant 20$ Hz with no secondary mode below the first primary mode (ArianeSpace [3]).
HR-004	Plastic deformation	No plastic deformation allowed beyond 0.1 nm/m after launch to ensure operational requirements and dictate the boundary conditions on optical bench integration.
HR-005	Mechanical stability	During operation (2π rotation) the ΔD change in baseline direction must be $\leqslant$ 0.1 nm.
HR-006	Thermal stability	Thermal fluctuations due to rotation in the Lissajous orbit at L2 must meet HR-005. Thermal gradients are to satisfy dictated mechanical deviations and dimensional variations.
HR-007	Spacecraft CoG	The center of gravity (CoG) of the spacecraft must satisfy the ArianeSpace design requirements as defined by: $0.2 + 0.14 \times M < H_{CoG}(m) < 2.85 + 0.2 \times M$, where M is the mass of the spacecraft in tonnes (ArianeSpace [3]).
HR-008	Acoustic vibration in flight	The spacecraft must be able to withstand in flight acoustic dB levels as specified by ArianeSpace. Especially during lift-off and the transonic phase the acoustic levels due to in flight phenomena can reach high levels, up to 139.5 dB (ArianeSpace [3]).
HR-009	Sinusoidal excitation	The spacecraft must be able to withstand the sinusoidal excitation as provided by ArianeSpace (ArianeSpace [3]).
HR-010	Aerothermal flux after fairing jettisoning	The spacecraft must withstand an aerothermal flux of up to 1135 W/m^2 (ArianeSpace [3]).
HR-011	Spacecraft length	The total spacecraft length must be $\leqslant 16.3$ m, of which the initial spacecraft bus requires 1.3 m (ArianeSpace [3]).
HR-012	Structure diameter	The diameter of the structure must be $\leqslant 2.33$ m at the tip of the 16.3 m length, based on the available fairing volume (ArianeSpace [3]).
HR-013	Spacecraft mass	The total spacecraft mass must be $\leqslant 6900$ kg. The mass envelope for the entire spacecraft is 6900 kg, with a yet to be determined envelope for the structure specifically.

ID	Title	Description
HR-014	Spacecraft material (1)	The spacecraft material must have a total mass loss (TML) $\leqslant 1\%$ and a collected volatile condensible material (CVCM) $\leqslant 0.1\%$. The selected materials for the spacecraft structures must satisfy the design requirements as provided by (ArianeSpace [3], ECSS [4]).
HR-015	Spacecraft material (2)	The spacecraft material must have a recovered mass loss (RML) $\leqslant 0.1\%$ and a collected volatile condensible material (CVCM) $\leqslant 0.01\%$. The given requirement is applied to spacecraft components in the vicinity of optical devices, which the selected materials must satisfy (ECSS [4]). Specified in section 5.2.1.2 of the ECSS standards.
HR-016	Spacecraft static unbalance	The spacecraft must satisfy ArianeSpace's static unbalance requirements. This means that for a spun-up spacecraft the CoG must stay within d $\leqslant$ 30 mm from the launcher's longitudinal axis. For a three-axis stabilized spacecraft of 6900 kg this becomes 70 mm.
SR-001	Optical obstruction	Obstruction of the photon paths by the structure must be minimized to maximize scientific potential and collection of photons.
SR-002	Shock loads / Micrometeoroid impact	Micrometeoroid impact of 1/m^2/year with an force of 15708 N and impulse duration of 5 nanoseconds. Based on a micrometeoroid with a diameter of 0.01 cm, an assumed spherical shape, a density of 2500 kg/m^3, and a velocity of 20 km/s. The effects of such an impact on the tumbling and resonances are to be identified.

3
Literature Review

This chapter focuses on relevant aspects in past literature. This review looked into heritage missions and more specifically missions that require stringent stability requirements, highlighting the Laser Interferometer Space Antenna (LISA) and the Global Astrometric Interferometer for Astrophysics (Gaia). Common design drivers can be identified based on known literature, which combined with XRIstel specific requirements, leads to mission design drivers.

3.1. Heritage Missions

The development of ultra-stable spacecraft structures has been strongly influenced by past, current, and future missions that push the limits of optical and dimensional stability. No past mission combines all requirements and technologies that arise in the XRIstel mission, but several heritage missions demonstrate key technologies, structural concepts, and material applications that are directly applicable to the development of ultra-stable structures. The Astro2020 Decadal Survey identified structural and optical stability as one of the critical technologies for future large space observatories, highlighting mission concepts such as LUVOIR and the Habitable World Observatory (HWO) (Feinberg et al. [5]).

Ultra-stability requirements are not limited to large optical telescopes. Missions such as LISA and Gaia impose similarly stringent stability requirements, but for different scientific objectives. LISA requires extreme dimensional stability for interferometric distance measurements and Gaia relies on extreme thermo-mechanical stability to maintain relative alignment between its optical systems. Besides the differences, these missions demonstrate that the achievable scientific performance is (in)directly linked to, and thus often limited by, the stability of supporting structures.

The same principle applies to the XRIstel mission. Its interferometric architecture differs from the segmented optical systems such as HWO, Gaia, or the James Webb Space Telescope (JWST). Neither does it rely on formation-flying missions such as LISA, but XRIstel does similarly rely on maintaining relative position of multiple optical elements at the nanometer-level stability. Consequently, material selection, structural design strategies, and stability concepts of these heritage missions provide valuable insights into the design of an ultra-stable spacecraft structure for XRIstel. A summary of these heritage missions can be found in Table 3.1.

3.1.1. Laser Interferometer Space Antenna (LISA)

LISA is a space-based gravitational wave observatory that detects nanometer- and picometer-level variations in the distances between three spacecrafts, separated by 2.5 million kilometers in an Earth-trailing heliocentric orbit. The mission utilizes laser interferometry to measure gravitational wave strains originating from sources such as supermassive black holes and white dwarf binaries (Verlaan et al. [6], Lucarelli et al. [7], Danzmann et al. [8]). Although LISA differs from XRIstel in scientific aspect, as well as through its distributed spacecraft architecture, both missions rely on interferometric measurements, of which the performance is directly linked to the thermo-mechanical stability of supporting structures.

The required picometer-level precision imposed stringent requirements on mechanical and thermal stability. The mechanical distortions due to cool-down, outgassing, or change in gravitational environment must remain highly predictable, as structural instabilities directly influence the interferometer's sensitivity (Soldo [9]). The interferometer measurement noise of approximately 10 pm/$\sqrt{\text{Hz}}$ requires exceptional thermal stability within the observation bandwidth, while the optical benches and laser systems must remain within operating temperatures, ± 10 K of room temperature, to minimize static misalignment and maintain measurement stability.

To demonstrate that these requirements can be achieved, an ultra-stable telescope assembly (TA) breadboard was developed by Astrium GmbH and Xperion (Verlaan et al. [6], Lucarelli et al. [7]), as depicted in Figure 3.1. The main goal of the breadboard was to verify that a CFRP based structure and its mirror mounts could satisfy the required dimensional stability within a representative thermal environment, while simultaneously meeting stringent mass and stiffness constraints. The TA structure was designed to achieve a tunable coefficient of thermal expansion (CTE) in the order of 10^{-7} 1/K and to maintain highly predictable mechanical behaviour during cool-down to -90°C.

Table 3.1: Comparison of relevant heritage missions and their relevance to XRIstel.

Mission	Scientific Objective	Stability Driver	Primary Structural Material(s)	Relevance to XRIstel
LISA	Gravitational wave detection.	Picometer-level interferometric distance measurements.	CFRP, Invar, ZERODUR	Demonstrates ultra-stable optical assemblies, predictable thermo-mechanical behaviour, and near-zero CTE structures.
Gaia	Astrometric mapping of Milky Way.	µas pointing accuracy and basic angle stability.	SiC	Demonstrates athermal structural design, ultra-stable payload structures, integrated interferometric metrology, long-term dimensional stability.
JWST	IR observations of early universe, galaxy evolution, and exoplanets.	Wavefront stability and optical alignment of segmented mirror.	CFRP, Beryllium, Invar	Demonstrates large lightweight structures, cryogenic dimensional stability, and precision optical alignment.
HWO	High-contrast imaging and spectroscopy of exoplanets.	Optical wavefront and line-of-sight stability.	Under investigation	Current state-of-the-art development of ultra-stable space telescopes.
XRIstel	Direct imaging and spectro-astrometric observations of X-ray sources.	Nanometer-level optical path length stability and ultra-precise pointing.	Under investigation	–

The experimental process thus focussed on CTE measurements and thermal gradient characterization of the entire telescope assembly (Verlaan et al. [6]).

The TA combined CFRP structural components with ZERODUR mirrors and Invar interfaces to the optical bench. Extensive material characterization and finite element method (FEM) analyses supported the design choices, targeting a CTE below 10^{-7} 1/K across the operational temperature range of -45°to -90°C, while minimizing thermo-mechanical deformations. The numerical analyses demonstrated compliance with the mass, eigenfrequency, displacement, temperature gradient, and moisture desorption requirements. These results confirmed the feasibility of CFRP as a structural material for ultra-stable interferometric space missions (Verlaan et al. [6]).

The LISA telescope assembly demonstrates several design principles that are directly applicable to the XRIstel mission, specifically the potential of CFRP as ultra-low CTE material. Additionally, it demonstrated the importance of predictable thermo-mechanical behaviour and extensive combination of experimental validation and numerical analysis to provide valuable insights into the design of large ultra-stable structures for spacecraft.

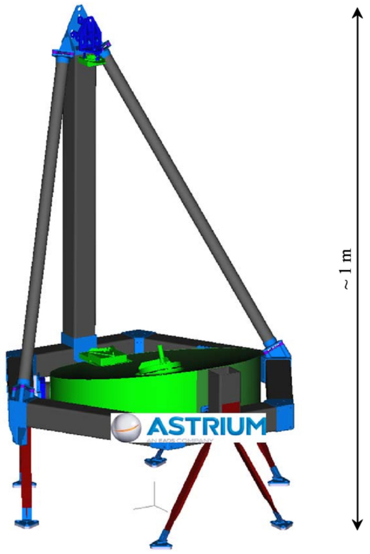

(a) One of the designs for stability experiments of the LISA TA.

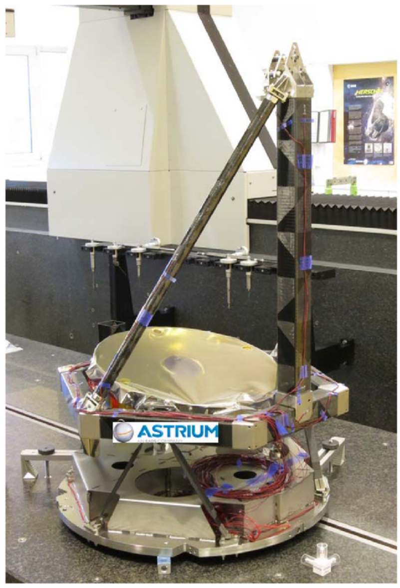

(b) The setup for the LISA TA for stability experiments.

Figure 3.1: The initial design model (left) and the actual experimental setup (right) as designed by Astrium GmbH and manufactured by Astrium GmbH and Xperion for the experiments on the stability of the LISA Telescope Assembly. (Verlaan et al. [6], Lucarelli et al. [7])

3.1.2. Global Astrometric Interferometer for Astrophysics (Gaia)

Gaia is one of ESA's astrometry missions and the successor of the Hipparcos mission, with the primary scientific objective of constructing a detailed 3D map of the Milky Way, by measuring stellar positions, distances, motion, and brightness variations. Gaia enabled detailed investigation of the galaxy's structure, formation, and evolution. The nominal operational lifetime of 5 years was extended to twelve years with final decommissioning on January 15, 2025. During its lifetime, Gaia observed more than 1.6 billion stars in the far-reaching regions of the Milky Way (Airbus Defence and Space [10], European Space Agency [11]).

The spacecraft was located in a Lissajous-type orbit around L2, similar to the intended XRIstel orbit, where both spacecraft rotate around their own axis. Gaia performed a slow rotation to enable repeated sky coverage and multiple observations of each target star, up to approximately 70 times during the mission (Meijer et al. [12]). To achieve its astrometric performance, Gaia required extreme attitude and pointing stability. This was realised through cold-gas micro-propulsion thrusters, allowing for the ultra-stable pointing and fine alignment (Airbus Defence and Space [10]). The resulting astrometric accuracy was within the range of 10 - 25 µas for primary measurements (Meijer et al. [12], Bougoin and Lavenac [13]).

These stability requirements directly drive the design of an ultra-stable payload structure. In particular, the stability of the basic angle between the two 1.5 m telescopes must be maintained within 7 µas over the duration of six hours (Bougoin and Lavenac [13]). Any thermo-mechanical deformations of the supporting structure directly influence the measurement errors and thus the scientific performance. This requires the payload to be designed as an athermal system in which only the line-of-sight fluctuations induced by thermal gradients are within tolerable limits (Meijer et al. [12]). To achieve this, silicon carbide (SiC) was used as the primary structural material throughout the payload structure and sub-structures.

The primary structural element is the ultra-stable torus platform, which supports the telescopes and the focal plane assembly. This quasi-octagonal hollow structure has a diameter of approximately 3 m and represent the largest ceramic-only instrument platform ever constructed (Airbus Defence and Space [10], ESA [14]). It was designed by Astrium GmbH and manufactured in collaboration with Boostec. The torus consists of seventeen brazed SiC segments, with a final structure mass below 200 kg while supporting approximately 420 kg of payload hardware (ESA [14]). The torus assembly is depicted in Figure 3.2b. All primary mirrors, structural benches, struts, focal plane supports, and components of the Basic Angle Monitoring (BAM) system are also made of SiC to ensure matching thermal behaviour and minimize thermally induced distortions (Bougoin and Lavenac [13]).

In addition to the structural design, the BAM system provides continuous interferometric measurement of variations in the basic angle between the two telescopes, enabling in-flight correction of residual structural drifts (Meijer et al. [12], Gielesen et al. [15]). The system achieved an accuracy better than 0.5 µas root mean square (RMS) at five-minute intervals, corresponding to an optical path difference stability of approximately 1.5 picometers RMS. This level of performance requires thus a metrology system and support structures to maintain a picometer- and picoradian-level stability (Meijer et al. [12]).

Gaia demonstrated that ultra-high stability in large optical payload structures can be achieved through a combination of material homogeneity, athermal structural design, and integrated metrology. Especially, the exclusive use of SiC throughout the payload ensures matching thermal behaviour across the system. The segmented and brazed torus construction illustrated how large mechanically stable ceramic structures can be manufactured while adhering to strict mass and stiffness constraints.

Gaia is in many ways different to the XRIstel mission regarding scientific objectives, optical architecture, and overall spacecraft design, but both systems are fundamentally driven by requirements of extreme dimensional stability of their optical assemblies. The Gaia design provides key insights into possible structural design strategies that are directly relevant to the XRIstel spacecraft structure.

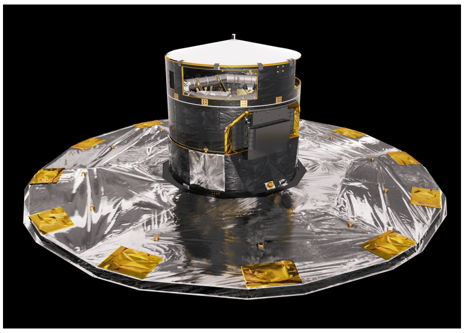

(a) Image of the Gaia spacecraft.

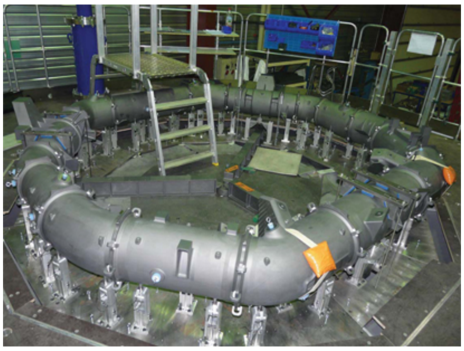

(b) Photo of the ultra-stable Torus structure.

Figure 3.2: a) Image of the Gaia spacecraft, image credit: ESA/ATG medialab. b) The ultra-stable Torus structure for Gaia, image credit: Boostec®.

3.1.3. James Webb Space Telescope (JWST)

The JWST is a large infrared space-based observatory designed to characterize exoplanet atmospheres and observe the earliest luminous objects in the universe. Its scientific performance relies on a 6.6 m segmented primary mirror operating at cryogenic temperatures of approximately 40 K (McElwain et al. [16], Gracey et al. [17]). These operating conditions impose stringent thermo-mechanical stability requirements, requiring the primary mirror backplane support structure (PMBSS) to remain stable within 32 nm while maintaining a line-of-sight (LOS) jitter below 7 mas RMS. Routine in-flight performance achieved approximately 1 mas RMS (McElwain et al. [16], McKeon [18], NASA Science [19]).

The PMBSS forms the primary structural element of the telescope and supports more than two tonnes of hardware, including the 18 mirror segments and the integrated science instrument module (ISIM). The ISIM metering structure accommodates four scientific instruments and a fine guidance sensor, while satisfying a structural mass allocation of approximately 300 kg and a minimum eigenfrequency requirement of 25 Hz. To achieve these requirements, the PMBSS and ISIM utilize a bonded composite frame (Gracey et al. [17], McKeon [18], NASA Science [19], Kunt et al. [20]).

The primary structural material consist of Toray M55J carbon fibres combined with a cyanate ester resin, selected for their high specific stiffness and low CTE. A custom tailored laminate of M55J/954-3 and T300/954-3 unidirectional tapes provides a near-zero CTE along the axis. Due to the extensive use of individual composite members, joints became a critical aspect of the design. Adhesive bonding was preferred over mechanically fastened composite joints, with Invar connective elements to match the CTE of the composite members and maintain structural integrity during cool-down to cryogenic temperatures. As structural adhesive, EA-9309 was selected due to its high elongation capability (McKeon [18], Kunt et al. [20]).

The size and operating temperature of JWST made full end-to-end ground verification very difficult, resulting in a verification-by-analysis approach centered on high-fidelity structural-thermal-optical performance (STOP) modelling (McElwain et al. [16], Gracey et al. [17]). Thermal analyses were done using Ansys Thermal Desktop, structural analyses using NASTRAN, and optical analyses using CodeV to predict thermal distortions, wavefront errors, bore-sight shifts, and pupil shear. Stochastic modelling accounted for material variability and geometric uncertainties. A 100-day cryogenic vacuum test at NASA's Johnson Space Center validated the thermal distortion predictions.

Although JWST differs from XRIstel through its cryogenic operating environment and segmented optical architecture, both missions require large lightweight structures that combine low mass with exceptional thermo-mechanical stability. Consequently, the composite structural design, tailored laminate development, and joint design philosophy provide valuable insights into applicable design strategies for the structural development and verification of the XRIstel spacecraft structure.

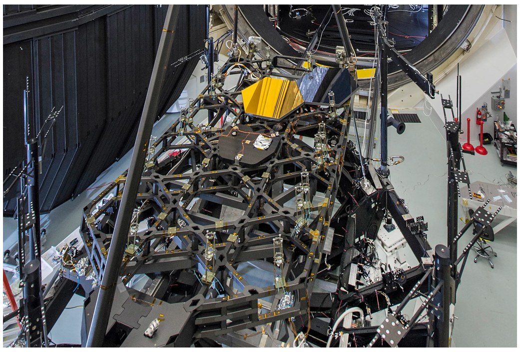

(a) JWST pathfinder before going into Chamber A.

(b) Structural wing sections of the mirror backplane.

Figure 3.3: a) JWST pathfinder clearly showing the large PMBSS before going into Chamber A for cryogenic testing, image credits: NASA/Chriss Gunn. b) Wing sections of the PMBSS during assembly, image credits: Northrop Grumman.

3.1.4. Habitable World Observatory (HWO)

The HWO is the future flagship mission recommended by the Astro2020 Decadal Survey and is designed to directly image and characterize potentially habitable exoplanets in its search for life (NASA Goddard Space Flight Center [21], Habitable Worlds Observatory [22]). To distinguish these faint planets from their much brighter host star, the coronagraph requires an optical contrast ratio of $\leqslant 1 \times 10^{-10}$, imposing picometer-level wavefront stability requirements that exceed those of previous space telescopes (Feinberg et al. [23]).

The current HWO concept is based on a 6 – 8 m off-axis segmented telescope operating near room temperature, making its thermal environment more comparable with XRIstel than cryogenic telescopes such as JWST (Habitable Worlds Observatory [22], Feinberg et al. [23]). Ultra-low expansion (ULE) glass is selected as the baseline mirror material, while ZERODUR remains a viable candidate due to its low CTE (Feinberg et al. [23]). To reduce sensitivity to residual vibrations, the observatory is designed for a fundamental natural frequency of > 10 Hz, while flat sunshields and a large micrometeoroid baffle provide both thermal and structural protection (Feinberg et al. [23]).

Verification of the observatory relies on an integrated modelling approach that combines STOP, jitter, and diffraction analyses to predict optical performance and contrast stability (Feinberg et al. [23]). Ground verification is supported by advanced optical metrology, including photonic integrated circuit heterodyne laser gauges and tracking frequency gauges, the latter demonstrating a measurements instability of < 3 pm over several hours (Carrier et al. [24]).

HWO differs from XRIstel in terms of its optical architecture and scientific objective, but both missions are fundamentally driven by the need to maintain extreme optical stability through an ultra-stable spacecraft structure. HWO demonstrates the importance of designing a stiff structural architecture that minimizes sensitivity to exported disturbances, while integrating structural, thermal, optical, and pointing analyses within a single verification framework. These design principles provide valuable insights into the structural developments and verification of XRIstel.

3.2. Design Drivers

This sections briefly discusses general design drivers that are inherent to almost any space mission, with a more detailed and specified summary of design drivers that are applicable to XRIstel. These are based on the problem definition and requirements as discussed in section 2.4 and the known design drivers from heritage missions as discussed in section 3.1.

3.2.1. General Design Drivers

Key design drivers in spacecraft structural design are mass minimization, high stiffness, high strength, and high reliability (Delft University of Technology [25], Zhu [26], Djojodihardjo [27], Annarella et al. [28]). Minimizing spacecraft mass is essential, as launch costs scale strongly with increasing mass, while structural mass directly reduces the available payload mass and thus the overall scientific return of the mission. At the same time, sufficient stiffness and strength are required to withstand launch loads and ensure structural integrity and operational capabilities in orbit.

The structural design process is inherently a trade-off between cost, performance, complexity, and feasibility. As noted by Djojodihardjo [27], reducing the number of parts can improve mass efficiency, reliability, and system-level performance. This design choice often leads to increased complexity due to functional integration of components. These trade-offs must be balanced to achieve an optimal design that ensures structural integration throughout its lifecycle.

A major part of the design space is defined by external constraints, of which the launch vehicle is one of the most dominant. It imposes strict limits on mass, volume, and interface geometry, while also defining the load environment during launch (Zhu [26], Annarella et al. [28]). These constraints propagate throughout the spacecraft architecture, influencing payload accommodation, subsystem layout, and overall structural configuration. The total mass is strictly limited, but early design phases allow some flexibility in mass distributions and subsystem allocations, requiring careful optimization to maximize the payload capability.

In addition, the launch and space environment introduce complex loading conditions, including static, dynamic, and shock loads, which differ fundamentally from terrestrial applications (Zhu [26], Djojodihardjo [27], Annarella et al. [28]). To mitigate risks, extensive thermo-mechanical analyses are typically performed during early design phases to predict structural behaviour and reduce uncertainties in later stages.

While often not the main design driver, the spacecraft structure also fulfils a purpose beyond its load bearing capacity. Serving as the mechanical backbone during integration and assembly, it provides the interfaces needed for subsystems and payloads, while also ensuring dimensional stability at all times (Annarella et al. [28]).

3.2.2. XRIstel-Specific Design Drivers

Beyond the general spacecraft constraints, the XRIstel mission introduces a set of highly stringent and coupled design drivers from its single-spacecraft XRI architecture. The first critical requirement that arises is the launch survivability, which is dictated predominantly by the Ariane 6 launch manual. It states several hard requirements that the spacecraft must fulfil specifically for the Ariane 64 long fairing configuration, including static, dynamic, and shock loads, as well as eigenfrequency requirements. These specific requirements are summarized in Table 2.2. Potentially the most critical requirement is the ultra-high thermo-mechanical stability, as nanometer and sub-nanometer scale optical path differences directly affect fringe visibility and thus the scientific performance of the telescope.

This latter requirement translates into extremely tight constraints on structural dimensional stability, as thermo-mechanical deformations, vibrations, and attitude variations introduce equivalent optical path errors. Consequently, structural stability, thermal stability, and pointing stability are inherently coupled, rather than independent design parameters.

In addition, the spacecraft must operate in a Lissajous-type orbit around L2 while undergoing controlled rolling motions. This imposes additional constraints on structural symmetry, mass distribution, and dynamic stability.

Minimized optical obstruction is directly connected to maximized effective area for the scientific instruments, thus constraining the allowable structural layouts and joint configurations further.

Finally, requirements derived from heritage missions such as LISA, Gaia, JWST, and HWO reinforce the need for ultra-stable structural concepts, minimal joint complexity, high material homogeneity, and integrated verification approaches, all of which strongly influence the structural design space.

3.3. Structural Architectures

Spacecraft structures are generally divided into primary and secondary structures. The primary structure forms the main load path between the launch vehicle and the spacecraft, while simultaneously providing interfaces for subsystems and payloads. Secondary structures support individual subsystems, instruments, solar arrays, and antennas. Failure of a primary structure typically results in mission loss while failure of a secondary structure not necessarily leads to mission loss, but can cause significantly degraded spacecraft performance (Djojodihardjo [27], Annarella et al. [28]).

Early spacecraft architectures were predominantly based on relatively simple truss-based primary structures combined with panel-based secondary structures (Rawal [29]). These configurations were primarily optimized to survive launch loads while providing sufficient stiffness and support for payload integration. However, increasing payload complexity and the demand for extreme stability have driven the development of more integrated and optimized structural concepts.

A relatively recent example of such developments is the approach presented by Choi and Ahn [30], where mesoscale CFRP lattice structures are developed with specific strengths comparable to conventional CFRP laminates and aluminium alloys, but with foam-like densities. The design methodology transforms a conventional structural layout into a lattice representation, which is further reduced to a nodal topology. This nodal representation enables the use of continuous fibre winding techniques, where fibres are deposited only along optimized load paths using 3D node winding. This approach eliminates non-load-bearing material and results in substantial mass reduction. Although demonstrated on small-scale drone structures and test specimens, scalability to large spacecraft structures remains a key challenge.

The spacecraft bus typically forms the structural core of the spacecraft, housing internal systems while providing protection against environmental effects such as radiation. Externally, it provides interfaces for appendages such as solar arrays, antennas, and radiators (Djojodihardjo [27]). While modular architectures enable rapid development and cost efficiency, they are often insufficient for missions with stringent mass and stability requirements. In such cases, non-modular, mission specific architectures are required despite increased development complexity and cost (Annarella et al. [28]).

Deployable structures are commonly used to reconcile mechanical requirements with strict launch volume constraints. While they enable compact stowage, they introduce additional system complexity and reliability risks. In parallel, multifunctional structural concepts have gained increased attention, where load-bearing elements are combined with additional functionalities such as thermal management, radiation shielding, or integration of electronics and sensors (Rawal [29]). For high-precision missions, this trend is complemented by the introduction of active structural elements, where sensors and actuators are embedded within structural components to enable feedback-based control of structural behaviour.

3.4. Materials for Space

This section discusses a brief introduction into common heritage space-grade materials and which properties are of importance to space certification. Additionally, the subsection on ultra-stable space materials discusses several materials that are considered candidates for ultra-stable applications due to specific material properties.

3.4.1. Common Materials

Material selection is a fundamental aspect of spacecraft structural design and is directly linked to mass constraints, load cases, and operational stability. In general, materials are selected based on their strength-to-density ratio and stiffness-to-density ratio. Additionally, properties such as thermal behaviour, manufacturability, and environmental resistance must also be considered (Zhu [26], Djojodihardjo [27], Annarella et al. [28]).

Historically, aluminium alloys, honeycomb sandwich panels, and fibre-reinforced composites have been widely used due to their favourable mechanical properties and established flight heritage. Early spacecrafts such as Sputnik and Explorer relied primarily on metallic structures, which were later supplemented and partially replaced by fibreglass composites. In more recent decades, these materials have further evolved towards boron-fibre composites and subsequently carbon-fibre reinforced polymers (CFRP) (Rawal [29]). While aluminium alloys and metallic structures remain widely used, the increasing demand for lightweight and dimensionally stable structures has led to a stronger reliance on composite materials for both primary and secondary structures.

Several material properties are critical for the spacecraft structural performance. Density directly influences launch cost and should therefore be minimized. Stiffness, defined by the Young's modulus, governs the structural response under load and plays a key role in vibrational behaviour and stability. While this is straightforward for isotropic materials, anisotropic composites require a more detailed characterization to accurately capture directional dependencies in structural performance. Material strength, including yield and ultimate strength, defines the limits of elastic behaviour and failure, with plastic deformation being particularly undesirable for high-precision structures (Zhu [26]).

Thermal properties are equally critical for spacecraft performance. The CTE determines dimensional changes under temperature variations, which can be significant between ground conditions and in-orbit operation. Thermal conductivity governs heat distribution within structural components and is therefore important for spacecraft thermal control. Additionally, low outgassing behaviour is required to prevent contamination in vacuum environments, which could otherwise lead to degradation of the optical and mechanical performance (Zhu [26], Djojodihardjo [27], Annarella et al. [28]).

3.4.2. Ultra-Stable Materials

The stringent thermo-mechanical stability requirements imposed by XRIstel's objectives significantly limit the range of suitable structural materials. Conventional spacecraft materials are primarily selected based on their specific strength and stiffness, ultra-stable structures additionally require exceptional dimensional stability through thermal behaviour. At the same time, outgassing should be low enough to satisfy stringent European Cooperation for Space Standardization (ECSS) outgassing requirements for materials near optical components. Several materials showing potential for precision space structures have been identified as material candidates for the XRIstel structure.

This section provides a preliminary overview of the most relevant material candidates, including their principal advantages, limitations, common applications, and potential relevance for the XRIstel mission. A qualitative comparison can be found in Table 3.2, followed by a summary of the most important material properties in Table 3.3. The individual materials are subsequently discussed in more detail with emphasis on characteristics relevant to XRIstel.

Table 3.2: Comparison of several ultra-stable material candidates considered for precision space structures.

Material	Advantages	Disadvantages	Common Applications	Relevance to XRIstel
ZERODUR	Near-zero CTE, high dimensional stability, available heritage	Brittle, relatively low specific stiffness	Precision mirrors, optical benches	Optical components requiring maximum dimensional stability
ALLVAR Alloy 30	Negative CTE	High density, limited structural purpose	Precision interfaces, CTE compensation	Connective joints to compensate thermo-mechanical deformations
SiC	High stiffness, low CTE, excellent thermal conductivity	Brittle, complex manufacturing	Optical benches, telescope structures	Ultra-stable optical support structures
C/SiC	Lightweight, high stiffness, low CTE	Complex manufacturing, limited heritage	Lightweight optical structures	Lightweight ultra-stable optical assemblies
CFRP	High specific stiffness, low density, tailored CTE	Anisotropic behaviour, manufacturing sensitivity	Primary and secondary spacecraft structures	Primary candidate for large ultra-stable structures
C/C-SiC	Low CTE, high stiffness, low density	Limited heritage, immature manufacturing process	Emerging ultra-stable precision structures	Novel candidate for large ultra-stable spacecraft structures
Invar 36	Low CTE, good mechanical characteristics	High density, difficult machinability	Smaller mounting components, structural joints	Connective joints to match CTE, smaller ultra-stable elements

ZERODUR
ZERODUR is a glass-ceramic material developed for applications requiring exceptional dimensional and thermal stability. Its near-zero coefficient of thermal expansion, high material homogeneity, and resistance to radiation-induced dimensional changes have resulted in extensive heritage in precision optical systems and ultra-stable mirrors such as for the LISA mission, as mentioned in subsection 3.1.1 (Hull et al. [31]). A summary of its material properties is provided in Table 3.3 (SCHOTT [32]).

Despite these advantages, ZERODUR has a relatively low specific stiffness and brittle failure behaviour, making it less suitable for large primary structures. Its application is therefore generally limited to precision optical components and optical benches that do not serve as primary load path, but still require dimensional stability.

Table 3.3: Summarized material properties of some ultra-stable material candidates considered for the XRIstel spacecraft structure as primary material or as secondary supporting material. Empty entries indicate that no representative value was available in consulted literature. Provided ranges provide an indication of value, but might be highly dependent on exact material specifications.

Material	ρ kg/m^3	E GPa	c_p J/(kg·K)	ν -	α 10^{-6}/K	λ W/(m·K)	σ_y MPa	σ_u MPa
ZERODUR	2530	90.3	800	0.24	0 ± 0.010	1.46	–	–
ALLVAR Alloy 30	5080	55	380	0.38	-30	8.88	295	650
SiC	3150	420	680	0.17	2.2	180	–	336
C/SiC	2700	270	700	–	2.0	125	–	–
CFRP *	1950	500 – 700	–	–	0.01 – 50	5 – 500	–	1000 – 3500
C/C-SiC	1900 – 2000	50 – 70	690 – 1550	–	-1.1 – 4.4 2.1 – 7.0 **	17 – 22.6 7.5 – 10.3 **	–	80 – 190
Invar 36	8100	141	515	0.29	1.6 – 6.0	10.15	276	448

* *Values are highly dependent on layup and composition, not one average can be easily determined.*
** *The first range is in-plane and the second range is out-of-plane.*

ALLVAR Alloy 30

ALLVAR Alloy 30 is a titanium-based alloy that exhibits a unique negative thermal expansion (NTE), meaning that it contracts when heated and expands when cooled. By combining NTE materials such as ALLVAR Alloy 30 with conventional positive-CTE materials, structures can theoretically achieve a net-zero effective CTE. This approach is particularly valuable when positive-CTE materials must be used or when large structures require thermal expansion compensation to achieve ultra-stability (Soldo [9], ALLVAR [33], NASA [34]). A summary of the material properties is provided in Table 3.3 (ALLVAR Alloys [35]).

The relatively high density limits the applicability of ALLVAR Alloy 30 as the primary material for a large spacecraft structure. However, it could be advantageous for smaller components or potentially joint structures. Utilizing it as connective elements can benefit the global thermal behaviour while simplifying assembly and integration.

Silicon Carbide (SiC)

Silicon Carbide (SiC) combines a high specific stiffness with a low CTE and high thermal conductivity, making it a suitable material for ultra-stable space structures. In addition to its favourable thermo-mechanical properties, SiC is characterized by an isotropic microstructure, radiation resistance, and the near absence of moisture absorption and outgassing, allowing for long-term dimensional stability (Bougoin and Lavenac [13], Robichaud et al. [36]). A summary of the material properties is provided in Table 3.3 (Bougoin and Lavenac [13], Harnisch et al. [37]).

Both reaction-bonded and sintered SiC have extensive flight heritage . Reaction-bonded SiC has demonstrated stable structural, thermal, and optical performance over a thermal range of +40 °C to -143 °C on the Long Range Reconnaissance Imager (LORRI) telescope aboard NASA's New Horizons mission (Robichaud et al. [36]). It managed to keep the thermal gradients at 1.0 °C laterally and 2.5 °C axially. FEM analyses and thermal vacuum testing validated SiC's structural, thermal, and optical performance, with no detected in-orbit degradation over multiple years (Robichaud et al. [36]).

Sintered SiC, such as Boostec® SiC, enables the manufacturing of large monolithic or brazed structures through green machining followed by sintering. As discussed in subsection 3.1.2, SiC formed the basis of Gaia's ultra-stable Torus structure. Additionally, SiC has also been applied in missions such as Herschel, Sentinel-2, and several JWST instruments (Bougoin and Lavenac [13]). Despite the advantages and the mature in-flight heritage, the brittle nature and relatively high density impose limitations on its structural usage.

Carbon/Silicon Carbide (C/SiC)

Carbon/Silicon Carbide (C/SiC) combines carbon fibres with a silicon carbide matrix, resulting in a lightweight material with high specific stiffness and advantageous thermo-mechanical stability. One of its principal advantages is the manufacturing process, in which complex geometries are machined in carbon green bodies before undergoing silicon infiltration. This minimizes shrinkage during processing and enables the production of lightweight complex monolithic structures (Harnisch et al. [37]). A summary of the material properties is provided in Table 3.3.

One of the limitations of C/SiC is its surface micro-roughness caused by the embedded carbon fibres, making the material unsuitable for precision optical surfaces without a polishable coating. Nevertheless, the combination of low mass, high stiffness, and thermal stability has resulted in utilization in several ESA missions, including the SEVIRI instrument on Meteosat and the mirrors for the ATLID lidar. It demonstrated great mechanical, thermal, and optical stability (Harnisch et al. [37]).

Carbon/Carbon Silicon Carbide (C/C-SiC)

Carbon/Carbon Silicon Carbide (C/C-SiC) is a ceramic matrix composite in which carbon fibre reinforcement is combined with a carbon and silicon carbide matrix. The material aims to combine the high specific strength of carbon-fibre composites with the dimensional and thermal stability of ceramics (Koutsounanos [38]). Carbeon-HPS, developed by Arceon, is a C/C-SiC variant specifically intended for high-precision structural applications that require dimensional stability under varying thermal environments (Arceon B.V. [39]). A summary of the material properties is provided in Table 3.3 (Koutsounanos [38]).

The material is manufactured by producing a near-net-shape CFRP component, which is converted into a porous carbon-carbon preform through pyrolysis. During the final liquid silicon infiltration process, molten silicon reacts locally with the carbon to form silicon carbide. This results in a heterogeneous microstructure consisting of carbon fibre bundles, carbon-rich regions, and SiC-rich regions (Koutsounanos [38]). This manufacturing technique allows individual carbon-carbon components to be assembled before infiltration and thus enables complex components whose material properties can be tailored.

Besides its favourable thermo-mechanical characteristics, C/C-SiC exhibits low open porosity and very low outgassing, both of which are important for space applications (Koutsounanos [38]). The close relationship between manufacturing, microstructure, and final material properties provide some flexibility in tailoring the material for specific needs, making it a candidate for ultra-stable spacecraft structures.

Carbon-fibre reinforced polymer (CFRP)

Carbon-fibre reinforced polymer (CFRP) composites are widely used in spacecraft structures due to their high specific strength and stiffness and their favourable thermal stability. These properties make CFRP particularly suitable for ultra-stable space structures where mass minimization and launch survivability are key constraints. The low density directly contributes to reduced launch costs and increased payload allocation. Mechanical performance ensures sufficient stiffness and strength to withstand launch loads (Sarkar [40]).

A key advantages of CFRP is its low CTE, enabling dimensional stability throughout thermal cycles in space environments. Additionally, carbon fibre materials can provide good thermal conductivity and low fatigue degradation, allowing for long-term structural integrity. CFRP is widely applied in primary and secondary spacecraft structures, satellite bus components, solar arrays, antennas, and deployable systems. As discussed in subsection 3.1.3, CFRP was used as the primary material for the PMBSS in JWST. However, one of the main limitations is its anisotropic behaviour, which requires careful considerations of fibre orientation, laminate lay-up, and load path alignment to ensure predictable structural performance (Sarkar [40]).

Within space applications, CFRP has become increasingly dominant due to its favourable material properties. Pitch-based carbon-fibres are particularly relevant for precision structures such as telescope support systems and optical benches due to their higher modulus and improved thermal stability, coming at a cost of reduced tensile strength compared to PAN-based fibres. PAN-based and epoxy based CFRP systems are more commonly used in aviation applications due to their fatigue resistance and fire resistance. In contrast, pitch-based CFRP systems are more common in space applications, where radiation resistance and dimensional stability are critical design drivers (Mamat et al. [41]). The material properties of CFRP are summarized in Table 3.3, and are strongly dependent on fibre-resin ratio, fibre orientation, and laminate stacking sequence. As a result, CFRP laminates can be tailored to achieve mission-specific mechanical and thermal performance requirements (Mamat et al. [41], Noh, Nam, and Kwak [42]).

Invar 36

Invar 36 is a nickel-iron alloy containing approximately 36% nickel, known for its exceptionally low CTE. This dimensional stability throughout temperature variations is linked to its ferromagnetic behaviour; below its Curie temperature, spontaneous volume magnetostriction counteracts normal lattice expansion (Harner [43], High Temp Metals [44], Meltio [45]). As a result, Invar 36 exhibits a CTE that is approximately one order of magnitude lower than that of carbon steel at temperatures up to 204°C, making it widely applicable in high-precision systems such as optical assemblies, laser systems, and spacecraft telescope structures.

For space applications, the main advantage of Invar 36 lies in its ability to maintain dimensional stability near ambient operating temperatures, which is critical for precision structural interfaces and alignment sensitive components. In addition, its relatively high ductility enables its use in glass-to-metal and ceramic-to-metal interfaces, where thermal expansion matching is required. However, the material is limited by its high density and the difficult machinability. It is a soft material which is prone to ”gummy” chips during machining and typically requires a multi-step heat treatment to relieve fabrication-induced stresses. Furthermore, oxidation at elevated temperatures requires controlled atmospheres during processing (Harner [43], High Temp Metals [44], Meltio [45]).

Provided these characteristics, Invar 36 is not considered a candidate as primary material for large structural architectures, but rather a suitable material for localized high-precision elements. Typical applications include structural joints, optical bench elements, and ultra-stable mounting interfaces. A summary of the material properties is provided in Table 3.3 (High Temp Metals [44]).

Additional Material Considerations

Beyond primary material parameters such as the coefficient of thermal expansion, density, and thermal conductivity, ultra-stable spacecraft structures are also influenced by higher-order material characteristics. In particular, anisotropy, inhomogeneity, material discontinuities, radiation-induced compaction, creep behaviour, and long-term dimensional drift can lead to the accumulation of small thermo-mechanical instabilities over time. As a results, material selection for ultra-stable structures must extend beyond conventional static mechanical properties and include detailed thermo-mechanical and temporal stability characterization (Hull et al. [31]).

A relevant example of material selection trade-offs is provided by the LISA telescope assembly breadboard study, as discussed in more detail in subsection 3.1.1. During this study, SiC 100, CSiC/CeSiC, ZERODUR, and CFRP were evaluated for ultra-stable structural applications. Although SiC 100 offers high stiffness, good thermal conductivity, and strong heritage, its non-negligible CTE was considered to be a limitation under representative thermal gradients, making it less suitable for the demonstrator. CSiC/CeSiC, while structurally similar to SiC, was also assessed as inferior in overall performance (Lucarelli et al. [7]).

ZERODUR demonstrated excellent thermal stability with near-zero CTE behaviour, but its relatively low stiffness and higher density resulted in less favourable performance in terms of mass, eigenfrequencies, and stress distribution compared to CFRP. CFRP offers high specific stiffness, low density, and tailorable thermo-mechanical behaviour through fibre orientation and laminate design, enabling near-zero CTE configurations in specific orientations. Based on the trade-off, CFRP was selected as the primary material for the LISA TA breadboard due to its superior overall structural performance (Lucarelli et al. [7]).

3.5. Structural Design Strategies

The design of ultra-stable spacecraft structures differs fundamentally from conventional spacecraft structural design due to the partial shift in design drivers. Traditional structures are primarily optimized for general design drivers, as discussed in subsection 3.2.1, whereas ultra-stable structures are optimized according to slightly different design drivers, as indicated in subsection 3.2.2.

Passive stability strategies form the primary design approach. These strategies focus on reducing instability at its source through the selection of materials with inherently low and predictable thermal expansion, the use of anisotropic material behaviour, and the minimization of material inhomogeneity. In addition, structural geometry plays a key role by reducing thermal gradients and limiting stress concentrations (Hull et al. [31]).

Once passive stability is maximized, active control strategies are introduced to mitigate residual instabilities. These include active thermal control through heating and/or cooling, wavefront sensing and correction for optical stability, and feedback-based structural actuation. As highlighted by Feinberg et al. [5], achieving stability in the order of 10 picometers over 10 minutes requires a combined approach of passive and active control strategies.

At this performance level, structural, thermal, and optical subsystems should no longer be designed independently. Ultra-stable spacecraft therefore require an integrated design philosophy in which materials, structural architecture, thermal control, and metrology are considered simultaneously throughout the design process. This represents a shift from traditional spacecraft development, where subsystems are typically designed separately and integrated at later stages.

The Finite Element Method (FEM) is key tool in the analysis and design of ultra-stable structures. FEM enables predictions of thermo-mechanical deformations that directly affect dimensional stability and optical path length (Liu et al. [46], Argence et al. [47], Banerjee et al. [48]). Unlike analytical approaches, FEM can handle complex geometries and material systems and is therefore essential for picometer-level stability analysis. It is widely used to evaluate thermal behaviour, vibrations, and geometry/material trade-offs without extensive physical experimental work. Symmetric structures generally reduce deformation sensitivity and simplify modelling complexity (Argence et al. [47], Banerjee et al. [48]).

FEM is also essential for optimizing support strategies and structural interfaces and is further used to reduce self-weight deformation through geometric optimization, such as offsetting component centres relative to structural axes.

For ultra-stable systems, FEM is also used for system level trade-offs involving interfaces, spacer geometries, and structural connections. As shown by (Argence et al. [47]), even small misalignments or angular offsets can significantly increase vibration sensitivity. Therefore, stress, deformation, and resonance behaviour of interfaces are evaluated under combined thermal and mechanical loads to ensure compliance with material and frequency requirements.

Thermal FEM is used to analyse temperature-induced instabilities and determine effective thermal expansion behaviour of integrated global structures. These simulations help identify temperature hotspots and zero-crossing temperatures where dimensional stability is maximized (Liu et al. [46], Banerjee et al. [48]). Even milikelvin deviations from these points can lead to large increases in instability. Thermal FEM is also used for composite structures and thermal shielding design, enabling predictions of long-term environmental effects (Liu et al. [46], Argence et al. [47]).

Dynamic FEM is used to assess vibration sensitivity and structural dynamic performance. Modal analysis determines fundamental frequencies and the influence of mounting structures on overall stability (Liu et al. [46], Argence et al. [47], Banerjee et al. [48]). Forced vibration analyses provide additional insights into in-phase and out-of-phase motion. FEM results are often integrated into parametric and multi-objective optimization approaches, linking geometry and material properties to general behaviour. In final design stages, models may be refined and experimentally validated where necessary (Liu et al. [46], Argence et al. [47]).

3.6. Conclusions

Based on the literature review, it can be concluded that XRIstel is not the first space mission that requires ultra-stability, with heritage missions such as LISA, Gaia, and JWST also aiming for ultra-stable structures, or ultra-stable optical performance. No single mission combines the exact requirements that XRIstel has to satisfy, but heritage missions provide valuable insights, useful for XRIstel. LISA demonstrates the applicability of CFRP as primary material for picometer dimensionally stable structures, while Gaia demonstrates that material homogeneity can play a big role for an athermal design. JWST also demonstrated that CFRP can be utilized for lightweight ultra-stable structures with a near-zero CTE and adhesive-based joints. Combined with the general and XRIstel-specific design drivers, these heritage missions show that XRIstel's stability and launch survivability are even more stringent. Regarding the evaluated materials, CFRP is identified as the primary structural material with the most potential, provided its high specific stiffness/strength, low density, tailorable CTE, and its extensive heritage in past missions, such as LISA and JWST. Other ultra-stable materials such as ZERODUR, ALLVAR Alloy 30, SiC, C/SiC, and Invar offer low or even negative CTEs, but are more limiting regarding higher densities or brittle behaviour.

4 Conceptual Design

This chapter presents the conceptual phase of the spacecraft structure design process. First, the relevant load cases, environmental conditions, and requirements are identified and explained. Subsequently, a systematic concept generation process is performed using the design option tree and a `Python script`, after which candidate materials, geometries, and different configurations are evaluated through a series of trade-offs. The most promising concept is identified and forms the baseline for future detailed design.

4.1. Load Cases & Requirements

This section defines the load cases and requirements considered during the conceptual design phase. They represent the primary criteria used to compare concepts and design choices during the early trade-offs, while the complete set of requirements extends beyond the scope of this phase. Launch survivability is the dominant design driver at this stage, making the launch load case (HR-001) the primary structural criterion. Dimensional stability remains a critical mission requirement, but it is considered secondary during the initial concept generation. In addition to withstanding the launch loads, the spacecraft must satisfy performance requirements related to the fundamental lateral and longitudinal eigenfrequencies (HR-002 & HR-003). Additionally, the material outgassing constraints (HR-014 & HR-015) are of importance during material selection. The launch load cases are summarized in Table 4.1.

Safety Margins
The launch loads, as specified in the Ariane 6 launch manual, are not directly implemented as design loads, because appropriate safety factors must be included. The loads used in analytical approximations and finite element analysis (FEA) therefore exceed the nominal flight load limits. ESA follows the ECSS standards for structural safety factors, which are mostly consistent with the Ariane 6 launch manual, except that they specify more detailed safety factors. For structural components made of fibre-reinforced polymers and sandwich materials, a factor of safety (FOS) of 1.25 is applied when the component is verified experimentally. When components are verified by analysis only, a safety factor of 2.0 must be applied (ArianeSpace [3], ECSS [49]). For ceramic materials such as SiC, the corresponding factors increase to 2.5 and 5.0 respectively (ECSS [49]).

Launch Acceleration
During launch, the spacecraft experiences the most severe mechanical environment of its lifetime. Two phases are considered critical.

During the *Aerodynamic Phase*, the maximum lateral acceleration is 1.8 g. The longitudinal acceleration consists of a static component between 1.3 and 2.8 g and a dynamic component of $\pm$ 0.8 g. This results in a maximum longitudinal acceleration of 3.6 g.

During the *End-of-Flight Phase*, the maximum longitudinal acceleration occurs. The static longitudinal acceleration ranges from 2.2 to 4.6 g with a dynamic component of $\pm$ 1.4 g. This results in a maximum longitudinal acceleration of 6.0 g. The corresponding lateral acceleration is 1.0 g.

Eigenfrequencies
To satisfy launch survivability requirements, the spacecraft must satisfy the minimum eigenfrequency constraints defined in HR-002 & HR-003, as imposed by ArianeSpace. The fundamental lateral frequency must be at least 6 Hz, while the fundamental longitudinal frequency must be at least 20 Hz.

Material Outgassing
Requirements HR-014 & HR-015, based on the Ariane 6 launch manual and ECSS standards, impose limits on material outgassing for spacecraft components. The general spacecraft limits are RML $\leqslant 1\%$ and CVCM $\leqslant 0.1\%$. For components near optical elements the material must satisfy stricter limits: RML $\leqslant 0.1\%$ and CVCM $\leqslant 0.01\%$.

Table 4.1: Load cases that are evaluated for each of the concepts during the early conceptual design phase. The mechanical loads already include a safety factor of 2.0 according to ECSS standards for composite and sandwich materials that will only be verified analytically.

Load Case	**Load**	**Location / Direction**	**Analysis**
Aerodynamic Phase	7.2 g & 3.6 g	Longitudinal & Lateral	COMSOL (FEM)
End-of-Flight Phase	12.0 g & 2.0 g	Longitudinal & Lateral	COMSOL (FEM)

4.2. Design Option Tree

The conceptual design process begins with the identification of possible structural solutions and design choices. The design option tree, shown in Figure 4.1, provides a structured overview of the candidate options considered throughout the conceptual design phase. It shows both the complete design space considered at this stage, as well as the successive elimination of options based on literature findings, engineering assessment, and trade-offs discussed at later stages in this chapter.

The primary objective of the structural concept in this phase is to satisfy the launch survivability requirements while maintaining a feasible path towards dimensional stability. Consequently, the design option tree focuses on the principal design choices related to the primary structure, including beam geometry, material selection, structural reinforcement, and modelling strategy.

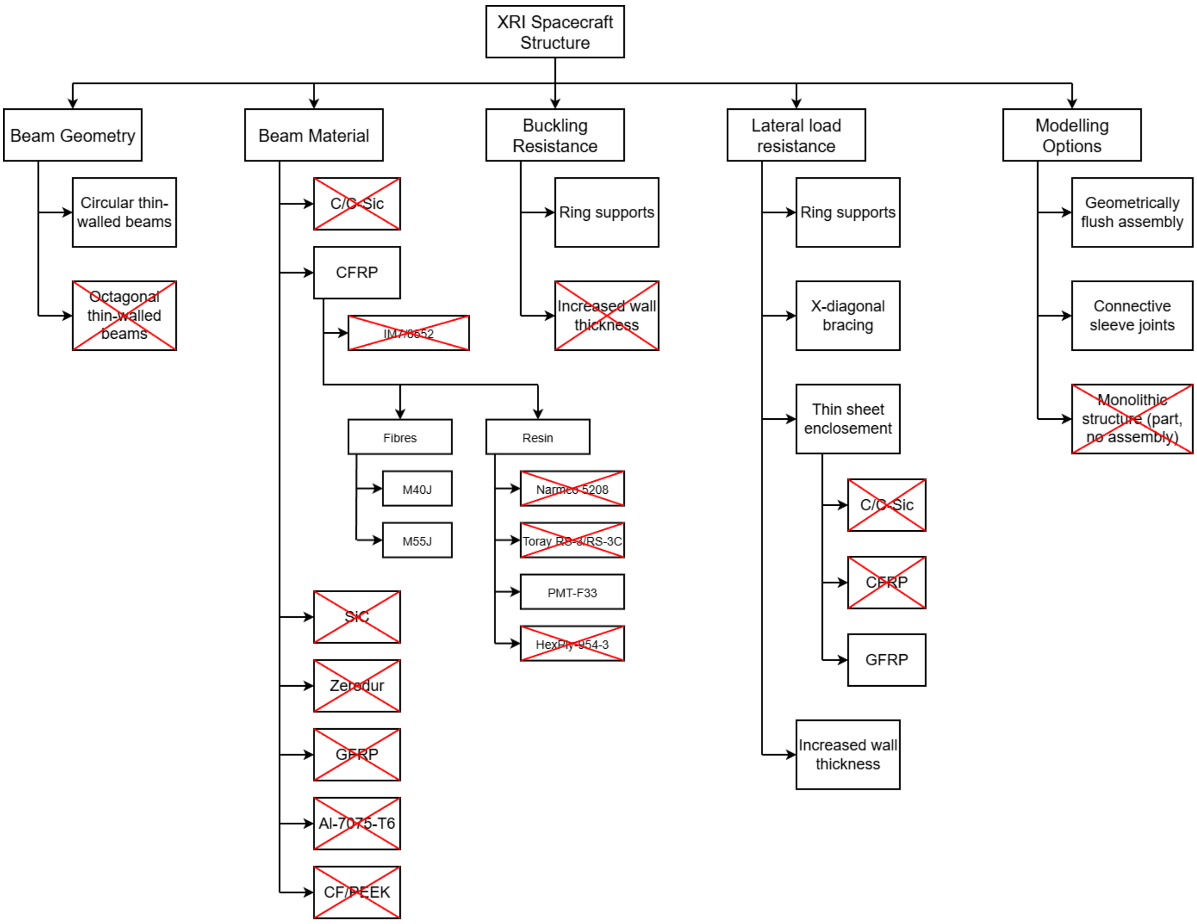

Figure 4.1: Design option tree depicting the originally considered design space and the eliminated options.

Beam Geometry

Two beam cross-sections are considered for the primary structure: thin-walled circular beams and thin-walled octagonal beams. Both candidate beam cross-sections can be seen in Figure 4.4.

Circular beams provide favourable structural behaviour due to their axisymmetric geometry, resulting in efficient load transfer, high buckling resistance, and limited stress concentrations. The smooth geometry also avoids sharp edges and corners that may locally increase mechanical or thermal stresses. A potential disadvantage is the integration of secondary components, such as the connection to the optical benches, which may require additional connective hardware.

Octagonal beams are primarily considered because of their flat surfaces which simplify assembly and integration of secondary components. Additionally, the octagonal geometry is consistent with the overall spacecraft layout, providing a geometrically consistent structural configuration. The mechanical disadvantage of octagonal cross-sections is discussed in subsection 4.5.3.

Beam Material

The candidate materials shown in Figure 4.1 are considered for the primary spacecraft structure, of which some were eliminated early on. The material selection is discussed in more detail in subsection 4.4.5.

C/C-SiC is included in the consideration because of its excellent dimensional stability, near-zero CTE, and very low outgassing. Potential limitations include its relatively moderate mechanical properties, higher expected manufacturing costs, and possible limitations to the manufacturable dimensions.

CFRP is considered because of its high stiffness and low density, with the possibility to tailor the material to achieve mission-specific mechanical and thermal properties. Several quasi-isotropic laminate combinations are considered using fibre-resin combinations with some flight heritage. This includes the Toray M55J fibres and the Hexply 954-3 cyanate ester resin as present in the JWST backplane (McKeon [18]), as well as the heritage on the XMM-Newton (European Space Agency (ESA) [50]).

SiC & C/SiC was initially considered because of its excellent thermal stability and successful application in the Gaia payload structure. Due to the high density and the significantly higher ECSS safety factors required for ceramic materials, it was considered not feasible at this stage, and was thus eliminated.

Similarly, ZERODUR was considered because of its exceptional dimensional stability, but due to its high density, brittle nature, and the same ceramic safety factors, it was eliminated early on.

GFRP was briefly considered because of its similarity to CFRP. However, its structural and thermal properties are in general inferior to CFRP, offering little to none advantage over CFRP besides lower cost. As cost is not a primary design driver at this stage, GFRP was not investigated further.

Aluminium 7075-T6 is a candidate due to its favourable mechanical properties, extensive flight heritage, and mature manufacturing techniques. Its CTE and density are significantly less favourable than those of CFRP and C/C-SiC.

CF/PEEK is considered because it combines carbon-fibre reinforcement with a thermoplastic matrix, providing great thermal behaviour together with low outgassing properties. Depending on the manufacturing process, both quasi-isotropic and highly anisotropic components are possible, allowing for tailored material properties.

Buckling Resistance

Two approaches are considered to improve the buckling resistance of the primary structure. The first option introduces intermediate ring structures connecting the eight primary beams. Besides reducing the effective buckling length of the beams, these rings contribute to the global stiffness of the spacecraft while providing convenient interfaces for subsystems. A visualization of this option can be seen in Figure 4.2a.

The second approach uses increased wall thicknesses of the primary beams. This method increases buckling resistance, but at the cost of a heavy mass penalty. Because intermediate ring structures are expected to fulfil multiple functions, increasing the wall thickness was not investigated any further as solution for buckling resistance specifically.

Lateral Load Resistance

Four options were considered to improve resistance against lateral launch loads and to increase the lateral eigenfrequency. The first approach uses the same ring structures as discussed for the buckling resistance. It allows the individual beams to act as a global frame while restricting lateral deformation.

The second option encloses the primary beam structure with a thin-wall outer shell, increasing the global bending stiffness through closed-section behaviour. Due to the need for external solar panels, the supporting substrate of these panels might in fact act as this thin-wall enclosement, depending on their integration onto the structure. A visualization of this option can be seen in Figure 4.2b.

The third consideration is the introduction of diagonal bracing between the primary beams. Several layouts are herein possible, but the feasibility depends on the available space and the joint connections. A visualization of this option can be seen in Figure 4.2c.

The final consideration is the increase of the wall thickness, which is introduced in the detailed design phase, and thus not considered during the conceptual design phase. This is deliberately done, as the goal is still to minimize the mass, while satisfying requirements with the minimal wall thickness as defined by the `Python script` discussed in section 4.3 and Appendix G.

Modelling Connections
Several modelling approaches are considered at this stage, mainly regarding the implementation of the model into FEM. The first option models the structure as a geometrically flush assembly of individual beams. This option is applied in the COMSOL models as the models are created with surface elements, meaning that they do not carry any geometrical thickness. Although this is not the most realistic way for the actual physical structure, it is applied due to its modelling ease.

The second approach represents an assembly of individual beam components that can be modelled with connective sleeves that can be joint together. This method has also been applied in the COMSOL models but with disregard of the thickness of beams. This results in a modular modelling approach where sleeves are included and allows beams to be connected, but with an overlap in surfaces, without physically including the thickness.

The third modelling option is to model the entire structure as a monolithic part without any individual components. This option was eliminated early on to allow for modular modelling and a faster iterative approach.

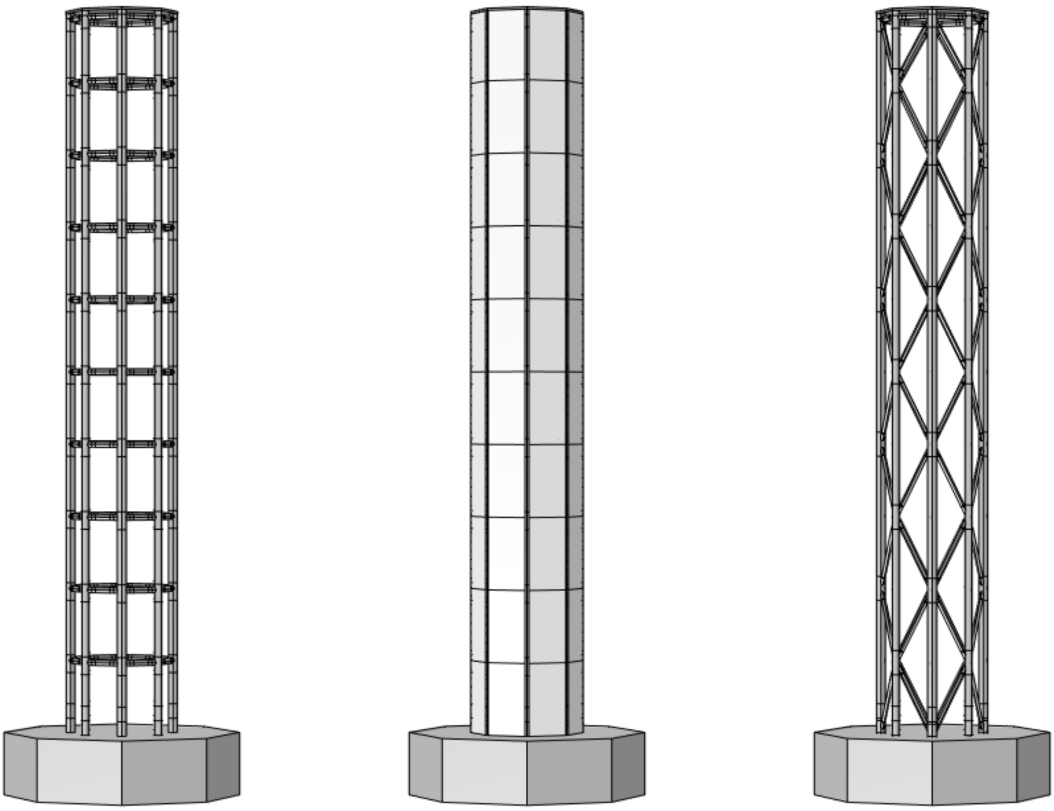

(a) Ring support structure. **(b)** Thin-sheet enclosure. **(c)** Diagonal support structure.

Figure 4.2: Three support structure candidates for the resistance against buckling and lateral loads.

4.3. Concept Generation

This section describes the generation and preliminary evaluation of structural concepts based on different materials, geometries, and support structure combinations. The concepts are assessed against the load cases and requirements as defined in section 4.1 and are then compared in the concept trade-off discussed in subsection 4.6.2. The objective is to identify a configuration that can serve as a starting point for further detailed design, selecting an initial wall thickness, outer diameter, support structures, and material candidate.

For each candidate material and beam geometry, an automated design exploration `Python script` is used to gain insights into potential combinations. The automated `Python script` is a rough approximation of the survivability of the launch loads to obtain an outer diameter of the beams and the wall thickness. The script evaluates sweeps across a range of beam diameters, wall thicknesses, and support structures to determine the lightest configuration that is able to survive launch. The analytical formulations applied in the `Python script` are presented in Appendix G. The `Python` files can be found on GitHub.

Based on the geometry trade-off as shown in subsection 4.5.3, only the circular beam cross-section was applied in the generation of concepts, as it outperformed the octagonal cross-section. Implementation of the octagonal cross-section into the `Python script` also confirmed its inferior characteristics by providing consistently higher wall thicknesses and outer beam diameters to survive the launch environment.

The conceptual spacecraft structure consists of eight primary beams supporting a total payload mass of 4500 kg. An equal load distribution over the beams is assumed during this phase, which is not physically accurate, but provides a first-order approximation. Individual beam dimensions are first evaluated for the longitudinal and lateral launch loads, after which the complete structural configuration is assessed under combined loading. When required, support rings and additional support structures are introduced to increase stiffness and improve buckling resistance while minimizing structural mass.

The `Python script` follows the general design approach as shown in Figure 4.3.

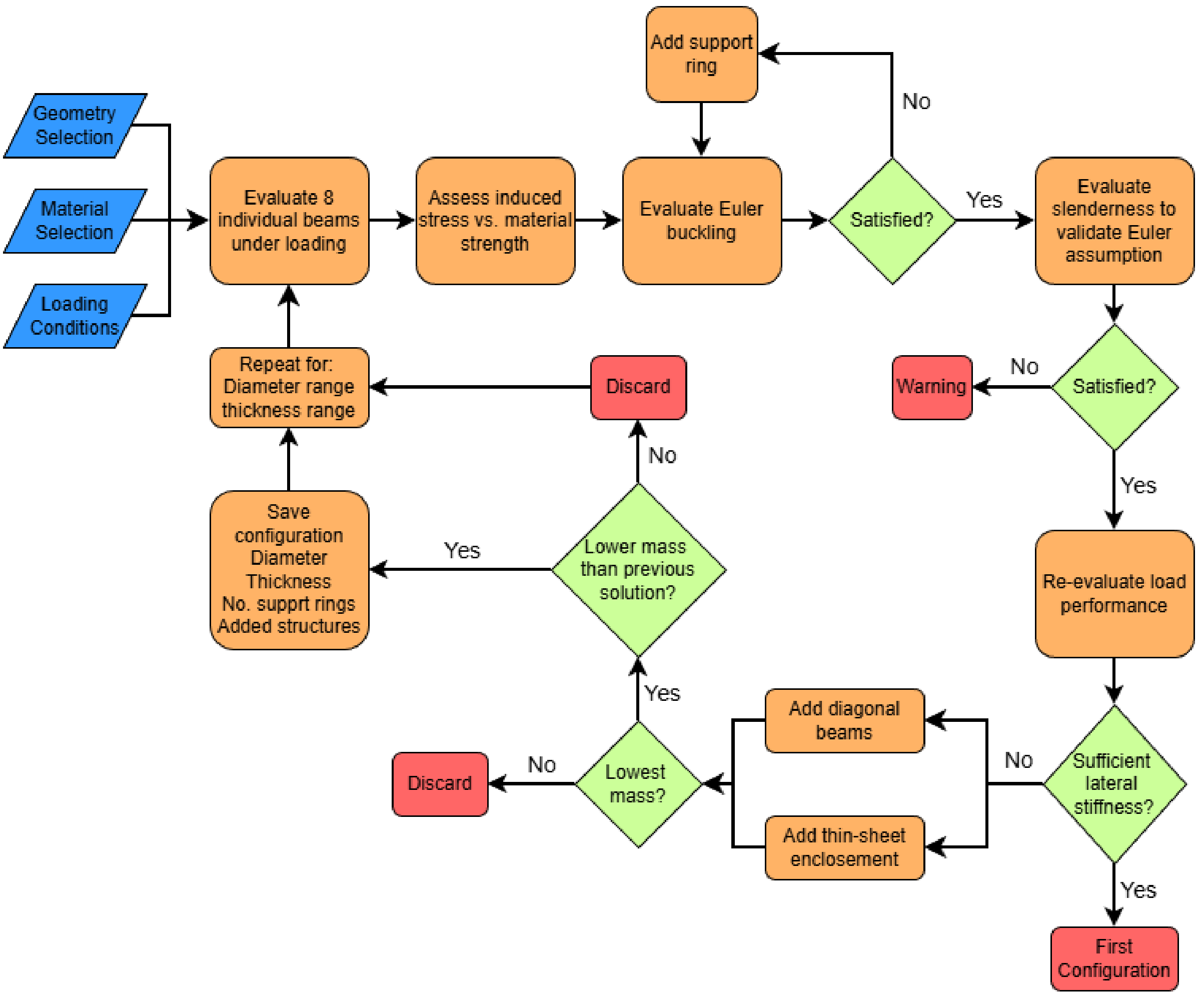

Figure 4.3: Conceptual design approach as implemented in Python, used to obtain first-order approximations of combined diameter/thickness/material/support structures that could satisfy the launch environment.

To include the material candidates into the concept generation, the material candidates have to be defined in more detail than provided in subsection 3.4.2. section 4.4 provides a detailed overview of the material definitions, while section 4.5 discusses the two geometries, resulting in the early elimination of the octagonal cross-section.

4.4. Candidate Materials

Some of the material options as mentioned in chapter 3 and depicted in Figure 4.1 are discussed in more detail in this section to provide workable material properties for FEM packages. Materials discussed include C/C-SiC, CFRP, Aluminium-7075-T6, and Carbon-Fibre reinforced Polyetheretherketon (CF/PEEK).

4.4.1. Carbon/Carbon-Silicon Carbide (C/C-SiC)

As discussed in subsection 3.4.2, C/C-SiC is one of the primary material candidates for the XRIstel spacecraft structure due to its relatively low density, near-zero CTE, and great outgassing properties. The available material properties are summarized in Appendix H and are based on laminates consisting of stacked (0°/ 90°) 2/2 twill weave fabric plies.

For the structural analyses in this chapter, a complete orthotropic material definition is needed for proper implementation in COMSOL. The available literature does not provide all the material characteristics, requiring the approximation of several directional properties. The provided material properties, as provided by Koutsounanos [38], were complemented with approximated properties based on the multi-scale modelling study by Ullah et al. [51]. The multi-scale modelling study investigated a similar 2/2 twill woven C/C-SiC composite material. Because both studies consider similar laminate architectures, the in-plane material properties are assumed to be nearly identical, resulting in E1 $\approx$ E2 = 70 GPa and ν12 $\approx$ ν21. The remaining elastic constants are approximated by preserving ratios reported by Ullah et al. [51] and scaling them to the measured material properties of Koutsounanos [38]. The full derivation of these properties is provided in Appendix H. The resulting orthotropic material properties adopted for the FEM analyses are summarized in Table 4.2.

Table 4.2: Material properties of C/C-SiC to be utilized for FEM analysis. Directions 1 & 2 are considered to be in-plane, while direction 3 is normal to both in-plane directions and thus out-of-plane.

Young's Modulus [MPa]		**Shear Modulus [MPa]**		**Poisson's Ratio [–]**		**Coefficient of Thermal Expansion [1/K]**		**Thermal Conductivity [W/mK]**	
Direction	Value	Direction	Value	Direction	Value	Direction	Value	Direction	Value
E1	70000	G12	26198	ν21	0.336	α1	$1e^{-7}$	λ1	19.0
E2	70000	G13	12051	ν31	0.133	α2	$1e^{-7}$	λ2	19.0
E3	44240	G23	12051	ν32	0.133	α3	$2e^{-6}$	λ3	9.0

4.4.2. Carbon-Fibre Reinforced Polymer (CFRP)

Carbon-fibre reinforced polymer (CFRP) is one of the primary material candidates for the spacecraft structure due to its high specific stiffness, low density, space heritage, and tunable CTE properties, as discussed in subsection 3.4.2. Unlike isotropic materials, CFRP requires a complete orthotropic material definition for FEA. Laminate properties are highly dependent on selected fibres, resin matrix, fibre volume fraction, and laminate layup.

For this conceptual design, the material properties are based on symmetrical quasi-isotropic laminates consisting of a 0° / $\pm$45° / 90° stacking sequence. This lay-up provides nearly identical in-plane properties with an anisotropic through-thickness characteristic. Some material properties have been taken from sources instead of approximations, such as the specific heat capacity (C_p), which can be assumed to be around 1000 J/(kg·K), based on a combination of fibres and cyanate ester (Calard et al. [52]).

The modelling approach follows a two-step homogenization process. Firstly, the unidirectional (UD) ply properties are estimated using a micromechanics approach, including the rule of mixtures (ROM) and Halpin-Tsai relations based on fibre and matrix properties. The raw fibre properties, resin properties, and UD ply properties can be found in Appendix C, with the micromechanics approach described in Appendix D.

The second step includes the approximation of quasi-isotropic laminate properties through classical laminate theory (CLT), assuming the symmetric 0° / $\pm$45° / 90° stacking. The final laminate properties are summarized in Table 4.3 and are the result of the methodology depicted in Appendix E.

Additionally, Appendix E also discusses the analytical approximation of the tensile strength, compressive strength, density, and effective Young's modulus of a CFRP laminate that can be used in first-order design approximations, as further discussed in section 4.3. These values have been summarized in Table 4.6.

Table 4.3: Comparison of different fibre/resin combinations after the quasi-isotropic laminate approximation. All quasi-isotropic laminates are based on a fibre volume fraction of ($V_f = 0.60$) and a ply stacking of symmetrical 0° / ±45° / 90° plies.

Property	Unit	M40J 5208	M40J RS3	M40J PMT-F33	M40J 954-3	M55J 5208	M55J RS3	M55J PMT-F33	M55J 954-3
E_1	GPa	82.3	81.2	81.2	80.9	114.9	113.8	113.8	113.5
E_2	GPa	82.3	81.2	81.2	80.9	114.9	113.8	113.8	113.5
E_3	GPa	8.8	7.7	7.7	7.4	8.8	7.7	7.7	7.4
G_{12}	GPa	31.2	30.7	30.7	30.6	43.4	42.9	42.9	42.8
G_{13}	GPa	4.3	3.5	3.5	3.3	4.3	3.5	3.5	3.3
G_{23}	GPa	4.3	3.5	3.5	3.3	4.3	3.5	3.5	3.3
ν_{21}*	–	0.319	0.322	0.322	0.323	0.323	0.326	0.325	0.326
ν_{31}*	–	0.037	0.033	0.033	0.032	0.027	0.024	0.024	0.023
ν_{32}*	–	0.037	0.033	0.033	0.032	0.027	0.024	0.024	0.023
α_1	$\times 10^{-6}$ 1/K	0.287	0.180	0.187	0.351	-0.302	-0.379	-0.374	-0.260
α_2	$\times 10^{-6}$ 1/K	0.287	0.180	0.187	0.351	-0.302	-0.379	-0.374	-0.260
α_3	$\times 10^{-6}$ 1/K	22.00	23.20	23.20	28.04	22.00	23.20	23.20	28.04
λ_1**	W/(m·K)	10.34	10.34	10.34	10.34	23.41	23.41	23.41	23.41
λ_2**	W/(m·K)	10.34	10.34	10.34	10.34	23.41	23.41	23.41	23.41
λ_3**	W/(m·K)	0.50	0.50	0.50	0.50	0.50	0.50	0.50	0.50

** Poisson's ratio for RS3, PMT-F33, HexPly 954-3 all assumed 0.35, same as Narmco 5208, as common values are 0.3 - 0.4.*
*** Resin thermal conductivity assumed the same 0.5 for each resin, as based on the Narmco 5208 value.*

4.4.3. Aluminium 7075-T6

Aluminium 7075-T6 is included as a reference material due to its extensive heritage in spacecraft structures. The alloy offers a high specific strength, mature manufacturing methods, and well-known mechanical behaviour. Unlike composite materials, Al-7075-T6 is isotropic, requiring only a single set of material properties for FEM implementation, which simplifies the structural analyses (Conniff and Tewolde [53]).

Although the alloy provides an attractive combination of properties, its relatively high coefficient of thermal expansion makes it less suitable for ultra-stable structures where dimensional stability is an important design driver. The limited weldability generally requires mechanical fastening methods, which potentially increase structural mass across large global structures. The material properties used during the conceptual design are summarized in Table 4.4.

Table 4.4: Material properties of Aluminium 7075-T6 used for the conceptual design and subsequent concept assessment, based on data provided by (Conniff and Tewolde [53]).

Material	Density [kg/m^3]	Young's Modulus [GPa]	Yield Strength [MPa]	Tensile Strength [MPa]	Comp. Strength [MPa]	CTE [1/K]	TC [W/(m·K)]
7075-T6	2810	71.7	505	570	505	$23.6e{-}6$	130

4.4.4. CF/PEEK

Carbon-fibre reinforced polyetheretherketon (CF/PEEK) is a material candidate because it combines the advantages of continuous fibre reinforcement with a high-performance thermoplastic matrix. Compared to conventional CFRP, CF/PEEK offers excellent damage tolerance, chemical resistance, and very low outgassing. This makes it especially interesting for spacecraft structures in the vicinity of optical elements.

The material properties used for the conceptual comparison are based on quasi-isotropic continuous-fibre CF/PEEK laminates experimentally characterized by Ju et al. [54]. The laminates consist of continuous-fibre UD prepregs consolidated by hot pressing them into a symmetric 0° / $\pm$45° / 90° stacking sequence. The fibre volume fraction is kept the same during approximations as for conventional CFRP, 60%. The UD ply properties for CF/PEEK are summarized in Table C.4.

The study by Ju et al. [54] does not provide a complete set of thermal material properties. Hence, the CTE and thermal conductivity are supplemented with data from the VICTREX 90HMF40 CF/PEEK material data sheet, assuming these values are representative for the laminate (VICTREX [55]).

The quasi-isotropic laminate properties used throughout the conceptual design phase are obtained using the CLT methodology described in Appendix E. The resulting orthotropic material properties are summarized in Table 4.5, with additional properties such as density and strength values summarized in Table 4.6.

Table 4.5: Orthotropic material properties of a quasi-isotropic CF/PEEK laminate as approximated using classical laminate theory. The UD material properties are provided in Table C.4.

Young's Modulus [MPa]		Shear Modulus [MPa]		Poisson's Ratio [–]		Coefficient of Thermal Expansion [1/K]		Thermal Conductivity [W/mK]	
Direction	Value	Direction	Value	Direction	Value	Direction	Value	Direction	Value
E1	54063	G12	21300	ν21	0.269	α1	$5.401e^{-6}$	λ1	1.375
E2	54063	G13	5700	ν31	0.067	α2	$5.401e^{-6}$	λ2	1.375
E3	10300	G23	3200	ν32	0.067	α3	$3.5e^{-5}$	λ3	0.750

4.4.5. Material Summary and Comparison

The material selection for large spacecraft structures is not a straightforward decision and depends on more than a single property. From the combinations considered in subsection 4.4.2, two options remain viable and are still considered, M40J/PMT-F33 and M55J/PMT-F33. The Narmco 5208 has been deemed unsuitable due to it being an epoxy resin, which has significantly inferior outgassing and moisture absorption properties compared to cyanate ester resins. The remaining three resins are fairly similar, but due to slightly superior mechanical properties of PMT-F33, this one has been chosen at this stage.

The CFRP fibres considered are M40J and M55J, with the IM7/8552 deemed unsuitable due to its inferior properties and higher mass for UD plies compared to M40J/M55J in combination with cyanate ester resins. The Toray M55J also shows heritage onboard the JWST in the backplane as mentioned by McKeon [18].

The outgassing properties have been at the center of some choices, as outgassing is a major risk for components near optical elements. The TML of C/C-SiC is publicly available on the website of Arceon B.V., with the RML and CVCM to be estimated equal or lower than the TML value, as this is generally the case. No exact values could be provided. The PMT-F33 cyanate ester resin has outgassing properties as defined in Table C.2, with a TML of 0.21% and a CVCM of 0.01%. Additionally, (NASA [56]) mentions, based on the 2006 reference GSC29923, that for a carbon fibre composite with M55J fibres and an unknown resin, the TML = 0.11%, RML = 0.07%, and the CVCM = 0.00%, boosting the confidence in low outgassing composite materials.

Table 4.6 depicts some of the critical material properties for the final materials that are considered. It is important to mention that the upper limit for the outgassing properties of CFRP materials is based on 100% resin mass fraction, and the lower limit is based on the mass fraction of resin with a 60% volume fibre fraction. In reality, the outgassing will never reach the upper limits, but will most likely be slightly higher than the lower limit. Lastly, it is worth mentioning that a too high RML, in comparison against the ECSS requirements, is often accepted when the CVCM is low enough.

Table 4.6: Comparison between material properties, where outgassing is compared against the ECSS requirements as dictated in ECSS-E-HB-32-20-1A and by Ariane (ArianeSpace [3]).

Property	Unit	ECSS	C/C-SiC	M40J / PMT-F33	M55J / PMT-F33	Al-7075-T6	CF/PEEK
Density	g/cm^3	-	1.95	1.526	1.622	2.81	1.58
Tensile strength	MPa	-	135.0	667.2	610.2	505.0	330.0
Compressive strength	MPa	-	265.0	317.5	220.0	505.0	310.0
Young's modulus	GPa	-	70.0	81.2	113.8	71.7	50.4
Outgassing (TML)	%	< 1.0	0.01	0.066 - 0.21	0.062 - 0.21	- *	0.33
Outgassing (RML)	%	< 0.1	$\leqslant 0.01$	$\leqslant 0.21$	$\leqslant 0.21$	- *	0.21
Outgassing (CVCM)	%	< 0.01	$\leqslant 0.01$	0.003 - 0.01	0.003 - 0.01	- *	0.00
CTE (in-plane)	$\times 10^{-6}$ 1/K	-	0.1	0.187	-0.374	23.6	5.401
CTE (out-of-plane)	$\times 10^{-6}$ 1/K	-	2.0	23.2	23.2	23.6	35.0
TC (in-plane)	W/(m·K)	-	19.0	10.34	23.41	130	1.375
TC (out-of-plane)	W/(m·K)	-	9.0	0.50	0.50	130	0.75

** Aluminium generally doesn't outgas, 7000-series has minimal outgassing due to high zinc-content. Quantity unknown.*

4.5. Candidate Geometries

This section discusses the primary beam geometry candidates and a trade-off between them. The comparison between the two cross-sections forms the basis for selecting the final cross-section of the main load carrying beams. Two configurations are evaluated: a thin-walled circular beam and a thin-walled octagonal beam.

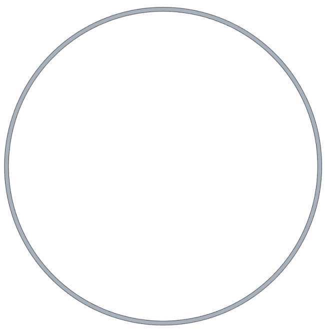

(a) Circular cross-section

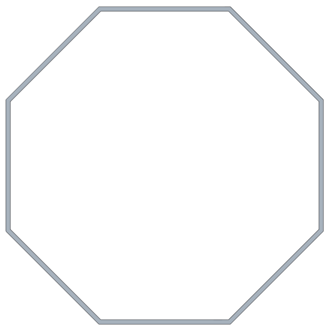

(b) Octagonal cross-section

Figure 4.4: Visualizations of the considered thin-walled circular cross-section and the thin-walled octagonal cross-section.

4.5.1. Thin-Walled Circular Beams

The thin-walled circular cross-section is selected as a primary candidate due to its favourable structural efficiency and geometric symmetry. Unlike polygonal geometries, the circular cross-section has perfect symmetry regardless of load direction. This allows it to be insensitive to load orientation in unpredictable environments such as launch environments.

Under bending or torsional loads, the circular geometry ensures a uniform stress distribution, since the distance from the neutral axis to the outer fibre is constant along the circumference. The result is a constant second moment of inertia in all directions, which is advantageous for multi-directional loading environments.

Lastly, the absence of corners and sharp edges eliminate geometric stress concentrations, thus reducing the likelihood of local failure. Simultaneously, it improves the predictability of global failure modes such as buckling. These characteristics make the circular cross-section especially robust for primary structural applications. A visualization of the thin-walled circular cross-section can be seen in Figure 4.4a.

4.5.2. Thin-Walled Octagonal Beams

The thin-walled octagonal cross-section is considered as a compromise between structural efficiency and practical integration considerations. An octagonal approximates the behaviour of a circular cross-section to a certain extent, while introducing flat surfaces that simplify assembly, integration, and mounting of secondary systems. It can be especially relevant for the XRIstel structure, which requires the integration of many components such as the solar arrays, mirror assemblies, and shielding.

The octagonal geometry introduces corners and sharp edges, which may lead to local stress concentrations and increased risks of local failures. Additionally, its stiffness is not fully symmetrical, as the structural response depends on whether the loading is applied to an edge or a flat surface.

Compared to a circular cross-section, the octagonal geometry is more sensitive to local skin buckling in the flat faces due to reduced curvature stiffness. Nonetheless, it still acts as a reasonable approximation of circular structural behaviour under a global symmetric loading and it remains an interesting option from an assembly and integration perspective. A visualization of the octagonal geometry can be seen in Figure 4.4b.

4.5.3. Geometry Trade-Off

The comparison between the two geometries is performed through analytical approximations and a supporting FEM analysis. To ensure a fair comparison, both geometries are evaluated using the same C/C-SiC material discussed in subsection 4.4.5. The available structural envelope is kept identical by dictating an outer diameter of 200 mm and a wall thickness of 2.5 mm, remaining within realistic design values.

For the circular cross-section, the full 200 mm diameter contributes to the second moment of area, while the octagonal cross-section has a corner-to-corner distance of 200 mm, resulting in a lower flat-to-flat distance. The result is a lower second moment of area for the octagonal cross-section.

The analytical comparison is performed according to the procedure described in Appendix F. The resulting performance metrics are summarized in Table 4.7 with the relative difference between circular and octagonal geometries depicted in Figure 4.5.

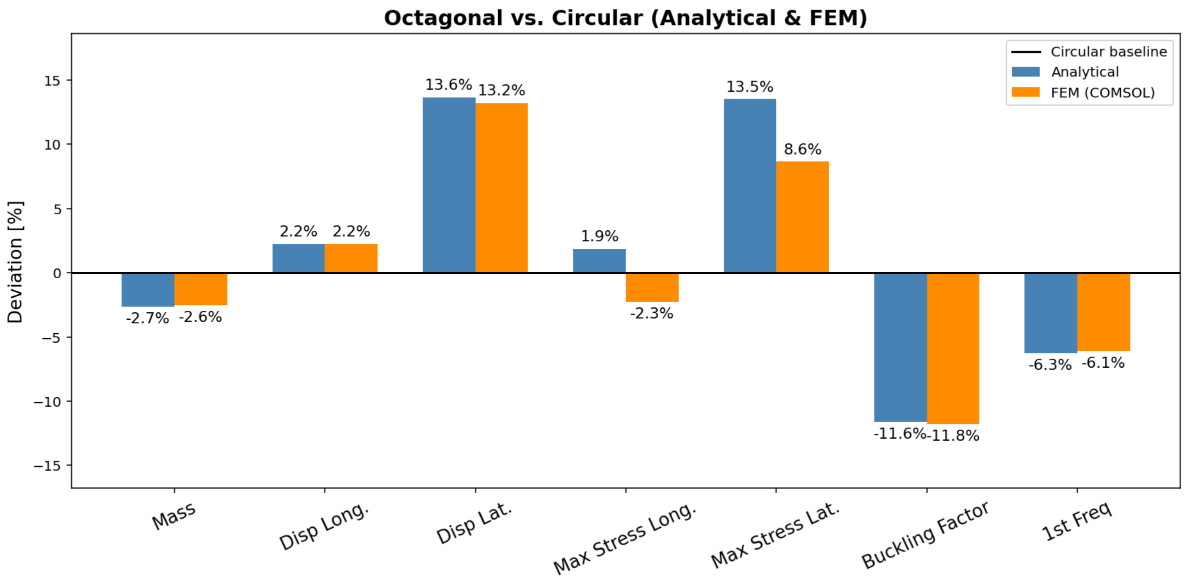

Figure 4.5: Performance comparison between the circular cross-section with $D_{out} = 200$ mm and $t_{wall} = 2.5$ mm as a baseline. The beam has a tip mass of 100 kg. The octagonal cross-section is compared to the circular baseline for both the analytical and FEM comparisons.

Table 4.7: Metrics extracted from COMSOL Multiphysics in support of the geometry trade-off. Geometries compared with $D_{out} = 200$ mm, $t_{wall} = 2.5$ mm, added top mass of 100 kg, launch loads as specified in section 4.1, and C/C-SiC material properties.

Property	Unit	Circular		Octagonal	
		FEM	Analytical	FEM	Analytical
Cross-sectional area	mm^2	1551.2	1551.2	1511.6	1510.0
Beam Mass	kg	45.371	45.3715	44.214	44.1682
Avg. surface stress (longitudinal load)	MPa	4.6571	4.6554	4.7525	4.7588
Max. displacement (longitudinal load)	mm	0.997	0.9976	1.02	1.01974
Max. displacement (lateral load)	mm	4390	4390	4970	4988
Max. surface stress (longitudinal load)	MPa	7.48	5.5162	7.31	5.6196
Max. surface stress (lateral load)	MPa	567	429.59	616	487.6459
Critical Buckling Factor	-	0.86861	0.67862	0.76619	0.59986
1^{st} eigenfrequency	Hz	0.32809	0.32818	0.30806	0.30767
2^{nd} eigenfrequency	Hz	0.32809	-	0.30806	-
3^{rd} eigenfrequency	Hz	4.6715	-	4.4355	-

To verify the analytical comparison, the same cases have been modelled and evaluated using FEM in COMSOL Multiphysics. As shown in Table 4.7, most analytical and FEM results differ by less than 1%, boosting confidence in the analytical approach and supporting the selection of the circular cross-section. Additionally, Figure 4.5 demonstrates that both the analytical and FEM analyses predict the same relative performance trends between the two cross-sections.

Three performance metrics show noticeable discrepancies between the analytical and FEM results. The first being the maximum longitudinal stress obtained through the FEM analysis is slightly lower for the octagonal cross-section than for the circular cross-section. This behaviour is not expected, but is likely caused by the shell approximation, discrete mesh, and local stress recovery in single nodes in the FEM model. This is supported by the sensitivity of this metric to mesh refinement.

The second discrepancy is that the maximum stresses obtained from FEM are higher than those predicted analytically for both load cases. Under longitudinal loading, the analytical approach assumes a purely axial stress state with a uniform stress distribution, neglecting local effects. The FEM model includes local deformation, distributed body loads, applied tip mass, and stress concentrations near the constrained root. Under lateral loading, the analytical solution assumes pure bending, a rigid cross-section, and a linear stress distribution. In contrast, FEM captures cross-sectional deformation, local stress concentrations, and the geometric influence of the octagonal corners. Additionally, the analytical model only accounts for the primary geometrical properties such as the cross-sectional area (A) and the second moment of area (I). The FEM model represents complete beam geometry and its load orientation.

Lastly, the critical buckling factors predicted by FEM are consistently higher than those obtained from the analytical Euler approximation. This is unexpected, as Euler assumes ideal geometry and boundary conditions. The discrepancy can be explained by the different modelling approaches. The analytical solution is based on classical Euler buckling, assuming pure axial compression, constant bending stiffness (E), a single global buckling mode, and neglecting shell behaviour. The FEM analysis determines the critical buckling factor through an eigenvalue analysis, accounting for shell stiffness, coupled membrane and bending behaviour, realistic load distribution, and the true buckling mode shapes. Despite the difference between both methods, the results indicate a consistent pattern, showcasing the superior behaviour of a circular cross-section. Hence the remaining of this study is done using thin-walled circular beams.

4.6. Structural Configuration Concepts

The analytical beam sizing method described in the previous sections results in a list of candidate structural configurations for each material, with their respective parameters and mass approximations. These configurations combine one of the selected materials, with a circular cross-section, an outer beam diameter, wall thickness, number of support rings, and additional support structures.

The resulting configurations are summarized in Table 4.8. These designs serve as the starting point of the conceptual design trade-off, where each of these parameter sets is modelled and subsequently analysed in COMSOL. At this stage of the study, the obtained parameters are merely a first-order design approximation, with the knowledge that a detailed design will significantly influence the parameter space. In addition to these obtained parameters, the respective FEM-appropriate material properties have been taken from subsection 4.4.5.

Table 4.8: Comparison between optimal designs for different materials with a circular cross-section of individual beams. The optimal designs are determined to satisfy the launch loads while minimizing mass.

Property	Unit	C/C-SiC	M40J / PMT-F33	M55J / PMT-F33	Al-7075-T6	CF/PEEK
Outer diameter	mm	297.91	187.20	236.61	240.58	207.84
Wall thickness	mm	1.32	1.00	1.03	0.50	1.00
Number of support rings	–	2	3	2	3	3
Additional support structure	–	none	none	none	none	none
Mass per beam	kg	36.10	13.39	18.55	15.90	15.40
Mass per ring	kg	17.17	6.37	8.82	7.56	7.32
Total estimated mass	kg	323.17	126.22	166.02	149.84	145.17

A first glance at the parameters in Table 4.8 demonstrates several noticeable differences. The high specific stiffness of the CFRP laminates allow for substantially lower structural masses than the C/C-SiC configuration, while maintaining structural performance. Between the two CFRP options, the higher modulus M55J/PMT-F33 configuration results in a larger beam diameter and thus a larger structural mass for nearly the same wall thickness. This is due to M55J being a higher-modulus fibre than M40J, but also less strong. The CF/PEEK concept achieves nearly the same structural mass as the Al-7075-T6 concept with a different thickness/diameter combination.

It should be noted that none of the analytical optimum configurations require additional support structures, which can be explained by the assumptions in the analytical model. With only the load cases as main design driver, the obtained concepts are able to withstand the launch environment, but do not necessarily satisfy eigenfrequency requirements. It is highly likely that the refined design will require additional structures to satisfy all requirements, as further discussed in chapter 5.

4.6.1. Concept COMSOL Models

The material properties discussed in section 4.4, combined with the geometrical parameters obtained from Table 4.8, are used as input for the COMSOL models. The models have been developed using a parametric approach, allowing for quick implementation of design changes, many iterations, and potentially future optimization studies.

Spacecraft Bus

The spacecraft bus, shown in Figure 4.6c, is outside the scope of this study and is therefore modelled as a rigid domain with artificially increased mechanical properties. Its dimensions are based on the Ariane 64 Long Fairing volume envelope, resulting in a corner-to-corner distance of 4.9 m and a height of 1.3 m (ArianeSpace [3]). Within the structural model, the spacecraft bus primarily provides the interfaces with the fixed constraint representing the launch vehicle while also serving as potential heat sink for the thermal analyses in later stages. At this stage, only the geometry and mass are considered relevant.

To obtain a realistic estimate of the spacecraft bus mass, several reference missions have been considered. These include **Spektr-RG** (eoPortal [57]), **Gaia** (ESA [58]), **XMM-Newton** (eoPortal [59]), **JWST** (Menzel et al. [60]), and **NewAthena**. Based on these reference missions and internal discussions within the XRIstel team, the spacecraft bus mass for XRIstel is estimated to be 1500 kg. This value is comparable to JWST, which represents a similar mission regarding the overall mass and destination orbit. Assuming a fuel allocation of roughly 300 kg, the corresponding dry mass is 1200 kg.

Because the spacecraft bus is modelled as a solid domain, the Solid Mechanics interface is applied in COMSOL, defining the corresponding element formulation and degrees of freedom.

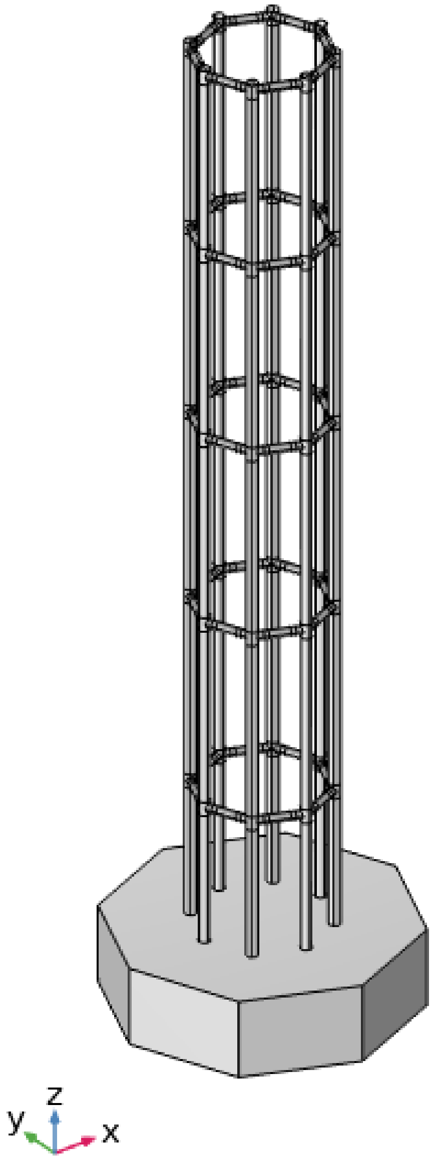

(a) COMSOL assembly of the M40J/PMT-F33 design with 5 support rings, of which the longitudinal beams are modelled as surfaces with shell physics.

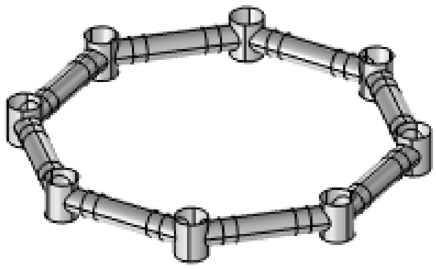

(b) COMSOL model of an individual support ring, modelled as surfaces with shell physics.

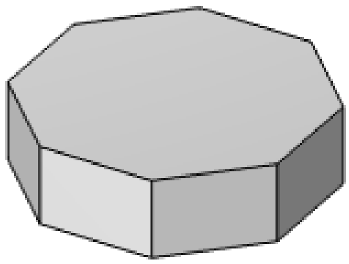

(c) COMSOL model of the solid spacecraft bus, modelled as domain with solid mechanics physics.

Figure 4.6: Several images of the COMSOL model for the M40J/PMT-F33 design. The model contains five support rings, where all beams are modelled as surfaces and have been assigned shell physics, while the spacecraft bus is considered rigid with solid mechanics physics.

Thin-Walled Beams
The thin-walled beams form the primary load-bearing structure and consist of the longitudinal beams and support rings. Both utilize the circular cross-section as selected in subsection 4.5.3, with the outer diameter and wall thicknesses defined in Table 4.8. Due to the their slender geometry, the beams are modelled as 2D shell surfaces, neglecting their through-thickness nodes. This shell formulation represents the structural behaviour through the beam mid-surface, significantly reducing the computational cost.

Because most candidate materials are orthotropic, the material orientation is carefully defined using local boundary coordinate systems. This ensures that the radial direction corresponds to the out-of-plane material direction, while the longitudinal and circumferential directions define the in-plane material axes.

The support rings are modelled using the same shell approximation as the longitudinal beams, differing only in the geometry. The vertical and horizontal sleeves are assigned an arbitrary wall thickness of 1.0 mm, with the outer diameter of the vertical sleeves matching that of the longitudinal beams. The horizontal sleeves are assigned an outer diameter equal to that of the longitudinal beams, minus 40 mm. The horizontal beam thickness remains equal to the longitudinal beam thickness. This reduction in diameter reflects the lower structural demands for these support rings. A visualization of the support ring is shown in Figure 4.6b.

Global Meshing
To generate a continuous finite element mesh, all components are unionized, defining a continuous connection between parts. Where shell surfaces overlap, the effective shell thickness is defined by the sum of the intersecting thicknesses, while the coupling between shell and solid boundaries is handled through COMSOL's multiphysics nodes.

Individual mesh settings are applied to the spacecraft bus and the shell structures. An extra coarse mesh is applied to the bus, whereas the shell elements are assigned the finest predefined mesh available within COMSOL. This predefined mesh dictates a minimum element size of 3.26 mm, a maximum element size of 326 mm, and an element growth rate of 1.3. Depending on the structural configuration, this results in approximately 200k – 700k boundary elements, placing significant demands on computational resources. As the mesh directly influences computational cost and solution accuracy, a mesh convergence study is done in Appendix K. An example of the applied mesh is shown in Figure 4.7.

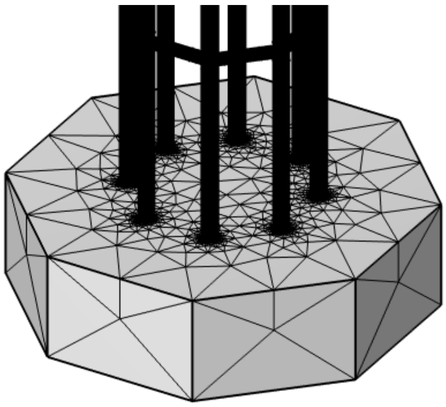

Figure 4.7: Extra coarse mesh for the spacecraft bus and extremely fine mesh for the shell elements. Total results in 11046 domain elements, 637110 boundary elements, and 44656 edge elements. This example is the M40J/PMT-F33 model with 5 support rings.

Analysis Steps
The analyses assessed at this stage primarily consider the launch load cases as discussed in section 4.1. For both the aerodynamic phase and the end-of-flight phase, the static loads and the response are assessed, as well as a linear buckling analysis during each launch phase. Additionally, the eigenfrequency analyses are done to gain insights into the fundamental longitudinal and lateral eigenfrequencies.

4.6.2. Concept / Material Trade-Off

To assess the five structural concepts, several evaluation metrics have been identified for the conceptual trade-off. These metrics are discussed in detail in Appendix I. Additional information on metric definitions and scoring methodology is provided in Table I.1 to Table I.3.

A trade-off sensitivity analysis has been performed to gain insights into the robustness of the methodology. This sensitivity analysis has been done by varying the weighting of the different criteria to asses the sensitivity of the final ranking to (subtle) changes in weight assignments. As shown in the additional trade-off tables in Appendix I, Table I.4 to Table I.7, the highest ranking concept remains unchanged regardless of the weights assigned.

Based on the final trade-off results, which are summarized in Table 4.9, the concept including the M40J/PMT-F33 material achieves the highest overall score. This concept, consisting of the above-mentioned material and five support rings, is therefore selected as the baseline configuration for the detailed design phase, discussed in chapter 5.

Table 4.9: Final trade-off table based on metrics defined and discussed in Appendix I and obtained from COMSOL simulations.

Final Conceptual Trade-Off												
			Concept 1		Concept 2		Concept 3		Concept 4		Concept 5	
		Material:	C/C-SiC		M40J/PMT-F33		M55J/PMT-F33		Al-7075-T6		CF/PEEK	
		Support rings:	2	5	3	5	2	5	3	5	3	5
Criterion		Weight	Score		Score		Score		Score		Score	
Total Structural Mass		0.125	1	1	4	4	1	1	1	1	3	3
Eight-Beam Volume		0.125	1		4		1		1		2	
Aerodynamic Phase	MoS	0.12	1	1	1	2	1	2	2	3	2	2
	Max Disp.	0.11	1	4	1	3	1	4	1	1	1	2
	CBF	0.07	3	3	3	3	3	4	1	1	2	3
End-of-Flight Phase	MoS	0.12	1	2	3	4	2	4	4	4	4	4
	Max Disp.	0.11	3	4	3	4	3	4	1	4	2	4
	CBF	0.05	3	4	4	4	4	4	1	1	3	3
Longitudinal Eigenfrequency		0.05	4	4	4	4	4	4	4	4	4	4
Lateral Eigenfrequency		0.12	1	2	1	1	1	2	1	1	1	1
		Total Score:	1.610	2.340	2.650	3.220	1.780	2.770	1.630	2.080	2.285	2.685
			1.975		2.935		2.275		1.855		2.485	

Based on the trade-off procedure and the final trade-off table, Table 4.9, the concept with the highest overall performance is the one including the M40J/PMT-F33 material. The concept with this material, and the 5 support rings will form the baseline for the next detailed design phase, which is discussed in chapter 5, detailing the design further to satisfy additional requirements and load cases.

4.7. Conclusion

The conceptual design phase is based on a structured and systematic design process, starting with a design option tree and a `Python tool` to allow initial rough sizing of the spacecraft structure. Several candidate structural concepts are evaluated against simplified launch load cases and requirements. Based on the geometry trade-off, the circular cross-section outperforms the octagonal cross-section for the thin-walled structural beams, as evaluated both analytically and through FEA. As a result, the octagonal cross-section is eliminated and not further investigated in this study. Additionally, the conceptual design phase favours composite materials over metallic and ceramic ones, with ceramic materials requiring a more than twice as large safety factor according to ECSS standards. Metallic materials can offer similar performance as the composite materials, but generally come at higher densities. As a result, the final conceptual trade-off confirmed these preliminary observations, identifying the concept based on the M40J/PMT-F33 material with five support rings as the best performing concept, regardless of trade-off weight distributions. This concept is taken as the baseline for further design iterations in the detailed design phase.

5
Detailed Design

This chapter discusses the detailed design phase, where the concept resulting from subsection 4.6.2 is further developed. Additional load cases and requirements have been identified, implemented, and discussed in chapter 6. The main design driver during the detailed design is the lateral eigenfrequency, which, based on preliminary conclusions of the conceptual design phase, seems to be the most difficult mechanical requirement to satisfy. The final configurations that have been modelled and assessed include Figure 5.1a, referred to as SO-BR (Single-Octagon-Bare), and Figure 5.1b, referred to as MO-BR (Multi-Octagon-Bare). Additional models are shown in Appendix J and include Figure J.1a, referred to as SO-HP (Single-Octagon-Half Panels), and Figure J.1b, referred to as SO-FP (Single-Octagon-Full Panels).

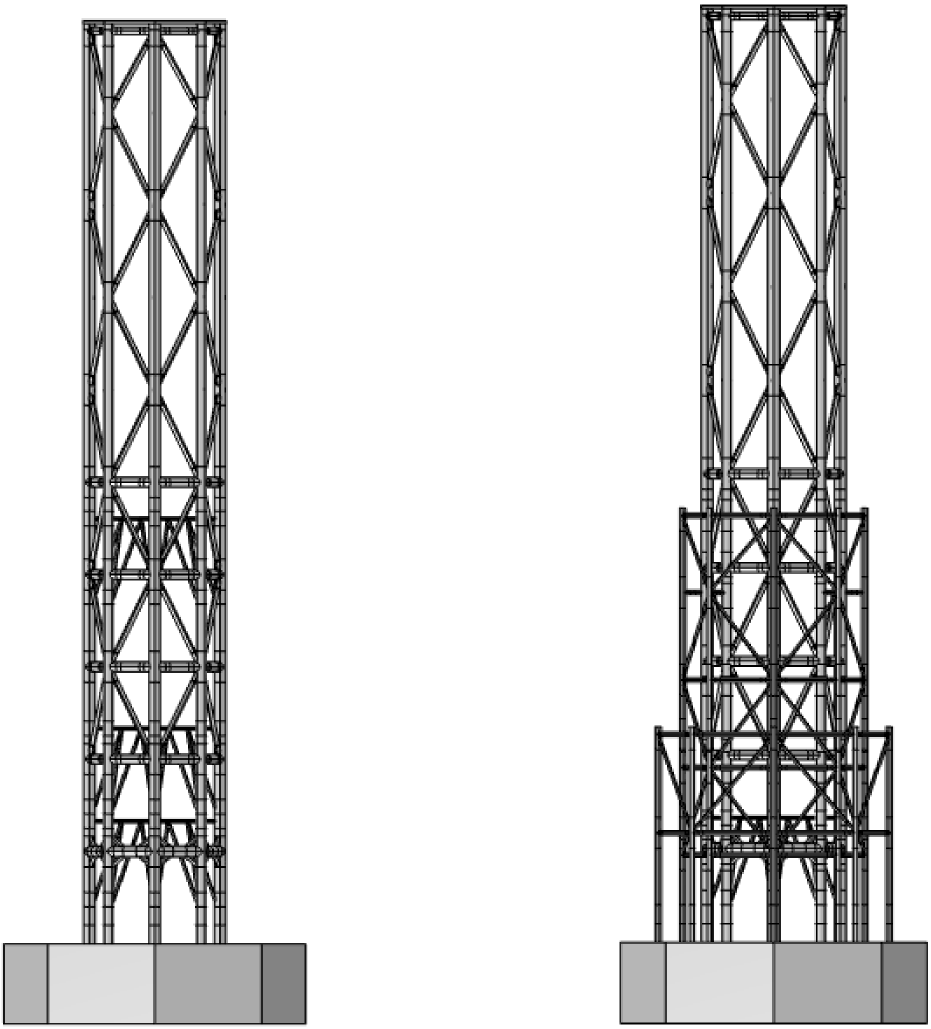

(a) The final structural configuration of the single-octagon structural design, excluding the mylar and solar panels.

(b) The final structural configuration of the multi-octagon structural design, excluding the mylar and solar panels.

Figure 5.1: The two final and bare configurations as designed in this chapter and analysed in chapter 6.

5.1. Thermal & L2 Environment

During launch and ascent, the spacecraft is exposed to varying thermal loads. Before fairing jettison, radiative heating from the fairing can reach approximately 1000 W/m^2 radiated from the fairing onto the spacecraft. After fairing separation, the aerothermal flux may reach up to 1135 W/m^2. In this phase, the dominant contribution is from direct solar radiation, with a nominal solar constant of 1361 W/m^2. The albedo and terrestrial infrared radiation are considered secondary for the launch conditions, assuming that the structure is partially shielded by the launch vehicle and assuming a simplified worst-case scenario. The resulting maximum thermal exposure is therefore given by the combination of aerothermal heating and perpendicular direct solar radiation (ArianeSpace [3]).

The Sun-Earth L2 point, located approximately 1.5 million kilometers from Earth, is the target operational environment for XRIstel. The spacecraft is assumed to operate in a Lissajous-type orbit, similar to previous missions such as Gaia. At L2, the dominant thermal effect is the direct solar radiation, with negligible contributions of Earth's albedo and terrestrial infrared radiation (Lockheed Martin Technical Operations [61]). The effective solar radiation at L2 remains similar to 1 AU conditions, typically within 1291 – 1421 W/m^2. The nominal design value is 1361 W/m^2. Particle radiation such as galactic cosmic rays, solar energetic particles, and trapped radiation belt particles are relevant for degradation and shielding effects, but are not considered during structural and thermal analyses (Lockheed Martin Technical Operations [61], Kohley et al. [62]).

Micrometeoroid impacts are included in the assessment of the detailed design, but are not a primary design driver during the design process. The focus of the impact study is to gain insights into the response behaviour of the structure, without leading to current design iterations. Space debris at L2 is considered negligible according to ORDEM-based predictions. Meteoroid flux is evaluated using the NASA Technical Memorandum 4527, predicting approximately 1075.09 impacts/m^2/year for particles of 1×10^{-4} cm. Similarly, for particles with a diameter of 700 cm the predictions decrease to 1.59169×10^{-18} meteoroid impacts/m^2/year (Lockheed Martin Technical Operations [61]). The distribution of meteoroid impacts can be seen in Figure 5.2.

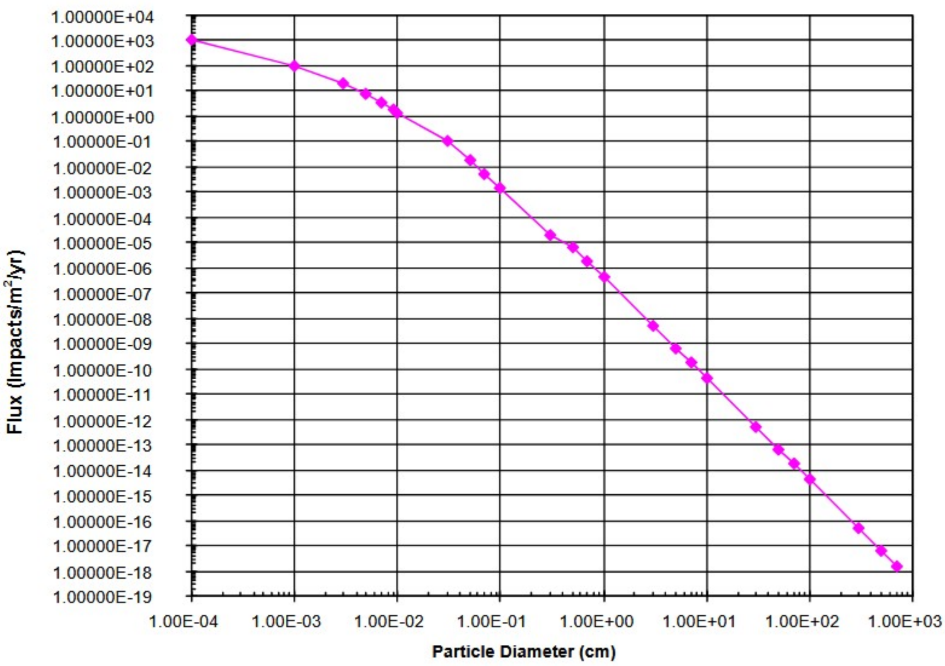

Figure 5.2: Graph depicting the meteoroid predictions based on the NASA Technical Memorandum-4527 model (Lockheed Martin Technical Operations [61]).

5.2. Load Cases & Requirements

The detailed design is eventually evaluated against a set of load cases and requirements, summarized in Table 5.1. These include mechanical, thermal, vibrational, and impact load environments to assess a broad range of behavioural characteristics.

The launch accelerations are identical to those defined in the conceptual design phase and are therefore not redefined here. They can be found in more detail in section 4.1.

During the detailed design phase, the lateral eigenfrequency is considered the primary design driver, as this requirement is the most difficult to meet. The other load cases and requirements were not part of the iterative design process, but rather provide valuable first-order insights into the expected behaviour of a large CFRP spacecraft structure.

The results of the mechanical analyses can be found in section 6.1, with eigenfrequency analysis results discussed in section 6.2.

Table 5.1: Summary of load cases and requirements investigated for the detailed design for later verification and performance assessment.

Load Case	Load	Location / Direction	Analysis
Aerodynamic phase	7.2 g & 3.6 g	Respectively in longitudinal and lateral direction.	Stationary Mechanical (FEM)
End-of-Flight phase	12.0 g & 2.0 g	Respectively in longitudinal and lateral direction.	Stationary Mechanical (FEM)
Thermal load (Launch)	1361 W/m^2 on sunlit side. Max 1135 W/m^2 on top of spacecraft.	Sunlit side and top of spacecraft.	Time Dependent Thermal Analysis (FEM)
Lateral sinusoidal excitation	0.6 – 0.8 g amplitude across 2 – 100 Hz in lateral direction.	At the base where the bus is connected to launch adapter.	Modal Response Analysis (Frequency Domain)
Longitudinal sinusoidal excitation	0.8 – 1.0 g amplitude across 2 – 100 Hz in longitudinal direction.	At the base where the bus is connected to launch adapter.	Modal Response Analysis (Frequency Domain)
Meteoroid impact	15708 N impulse force during 5 nanoseconds.	In the upper region of the CFRP structure, located between solar panels on the longitudinal beam.	Time Dependent Modal Response Analysis (FEM)
Requirement	**ID**	**Description**	**Analysis**
Longitudinal eigenfrequency	HR-003	The fundamental frequency along the longitudinal axis of the spacecraft must be $\geqslant$ 20 Hz.	Eigenfrequency Analysis (FEM)
Lateral eigenfrequency	HR-002	The fundamental frequency along the lateral axes of the spacecraft must be $\geqslant$ 6 Hz.	Eigenfrequency Analysis (FEM)
Spacecraft CoG	HR-007	The CoG of the spacecraft must satisfy $0.2 + 0.14 \times M < H_{CoG}(m) < 2.85 + 0.2 \times M$, where M is the mass of the spacecraft in tonnes.	COMSOL Model

5.2.1. Thermal Load (Launch)

During launch, the spacecraft is exposed to two dominant external thermal loads, as defined in section 5.1. The first is the aerothermal flux after fairing jettisoning, reaching up to 1135 W/m^2, mainly affecting surfaces normal to the flight direction. The aerothermal flux originates from thermal drag after fairing separation, which is roughly at 100 - 120 km altitude, where there are minimal particles in the environment, but the particles present reach temperatures of 300+ °C, causing a significant thermal drag. The aerothermal flux is provided by ArianeSpace [3] and is depicted as interpolated function in Figure 5.3.

The second external influence is the direct solar radiation with a nominal design value of 1361 W/m^2, which acts on the sunlit spacecraft side and is assumed to arrive at a normal incidence angle. The results of the thermal analysis after fairing separation can be found in section 6.5.

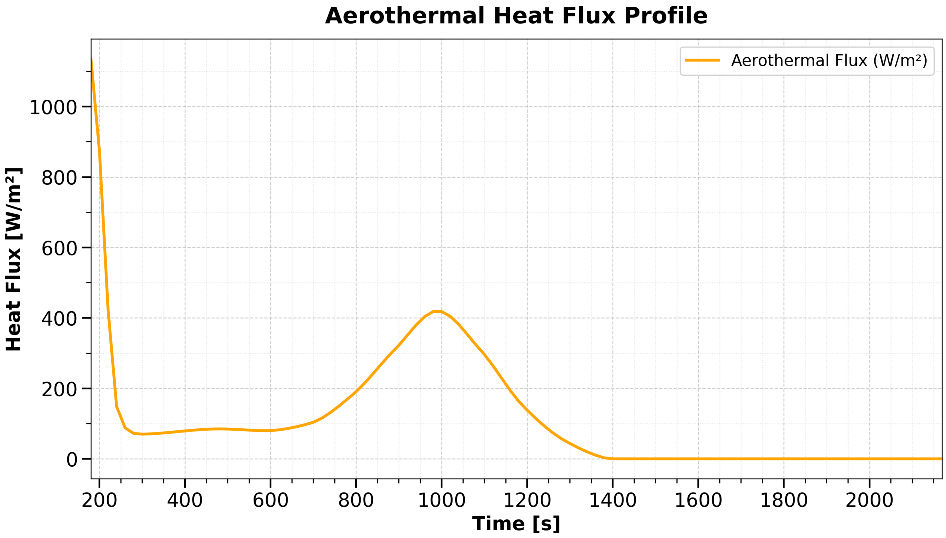

Figure 5.3: Aerothermal flux function as provided by the Ariane 6 launch manual.

5.2.2. Sinusoidal Excitation

The sine-equivalent dynamics in the 2 – 100 Hz frequency band are defined in the Ariane 6 launch manual and can be seen in Figure 5.4. The excitation is decomposed into longitudinal and lateral components, which are evaluated separately. These sinusoidal loads act at the spacecraft base and are combined with the static launch accelerations, with the aerodynamic phase considered as the most critical phase. It is important to note that the SC bus has not been designed in detail, and thus the transfer of the sinusoidal excitation through the SC bus to the base of the CFRP structure will be altered once the SC bus will be designed more thoroughly.

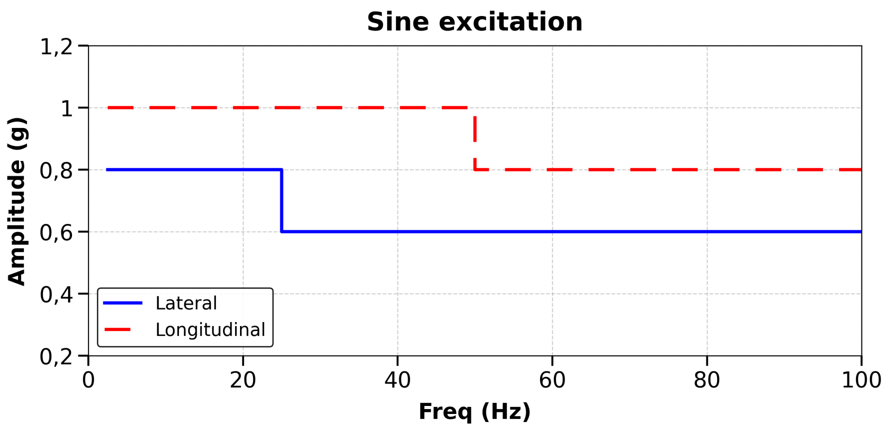

Figure 5.4: Sinusoidal excitation in both longitudinal and lateral direction as defined and provided by ArianeSpace (ArianeSpace [3]). The excitation is in addition to the already existing load cases and is present at the spacecraft base.

The numerical procedure follows a three-step process. Firstly, the static accelerations are applied in a stationary study step. The resulting final state of the stationary study serves as the input for the pre-stress eigenfrequency analysis. During the eigenfrequency analysis, the eigenfrequencies of the structure are determined while in the prestressed situation. The final study step includes the sinusoidal base excitation, which is applied to the bottom SC bus surface and covers the 0 – 100 Hz band. In this prestressed modal analysis, the response of the structure to this sinusoidal excitation input is determined. The results of the sinusoidal excitation analyses can be found in section 6.3.

5.2.3. Meteoroid Impact

The meteoroid impact analysis is a time-dependent analysis to evaluate the global, and local, structural response of the spacecraft to a localized micrometeoroid impact. The objective is to gain insights into the momentum transfer to the spacecraft, the tumbling response, and the structural vibrations and resonances introduced by the impact.

A representative micrometeoroid with a diameter of 0.01 cm is considered, which has an impact frequency of once per year per m^2, as discussed section 5.1. Assuming a spherical particle with a typical chondritic density of 2500 kg/m^3, the particle would have a mass of 1.309×10^{-9} kg. With a common (average) velocity of 20 km/s, the resulting momentum would become 2.618×10^{-5} N · s. Subsequently, the dynamic impulse is approximated by:

$$J_{total} = \beta \cdot p = 1.5 \cdot \left(2.618 \times 10^{-5}\right) = 3.927 \times 10^{-5} \text{ N} \cdot \text{s} \tag{5.1}$$

where β is the momentum enhancement factor that accounts for the additional momentum generated by ejecta during the impact. While values of 2.5 are common for aluminium, CFRP dissipates a larger fraction of the impact energy through mechanisms such as delamination and resin vaporization. Assuming the particle does not perforate the structure, a conservative value of $\beta = 1.5$ is applied.

The impact duration is approximated as the time required for the particle to traverse its own diameter, resulting in an impact window of 5 nanoseconds. Assuming a triangular impulse profile, the corresponding peak force is:

$$F_{max} = \frac{2 \cdot \left(3.927 \times 10^{-5} \text{ N} \cdot \text{s}\right)}{5 \times 10^{-9} \text{ s}} = 15708 \text{ N} \tag{5.2}$$

The equivalent impulse load is applied to a singular node near the upper tip of the CFRP structure. This location is chosen, because it represents a worst-case scenario, where the maximum global tumbling is introduced. The resulting response provides insights into the global tumbling motion, which is important for the AOCS budgets. Additionally, the analysis provides insights into the introduced resonances, by analysing the stress propagation waves through the CFRP structure, while also monitoring the changes in baseline distances because of vibrations. The results of the analyses can be found in section 6.4.

5.3. Mass Distribution

The spacecraft structure is intended to maintain the mechanical and thermal integrity of the optical assemblies during launch and operation. At this stage, the detailed implementation of the mirror assemblies is not feasible due to unknown baseline distributions, number of mirrors, and other system-level design choices. Thus, a generic mirror distribution is assumed, in which the longitudinal locations of the mirror assemblies are fixed, while their distribution over the available cross-sectional area remains unclear. A general visualization of the baseline configuration and relative mirror positioning is shown in Figure 5.5.

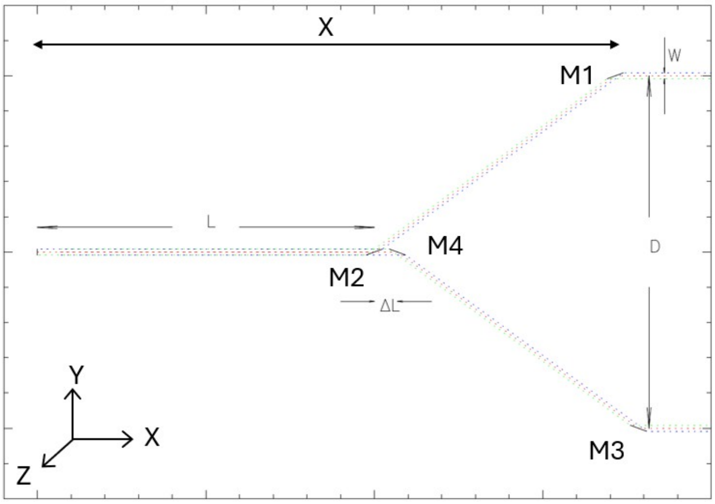

Figure 5.5: General depiction of the mirror distribution for any arbitrary baseline, with X the total length of the mirror assembly, L the beam overlap length (camera plane – M2/M4), ΔL being the distance between M2 and M4, and $B = X - L$ the length between the M2/M4 location and the M1/M3 location.

To ensure that the structural design remains applicable to the full mission goals, three representative baselines are considered. These baselines are 0.01, 0.1, and 1.0 m and thus include the largest, the smallest, and an intermediate baseline. For each baseline, the parameters X, L, and B are determined, assuming that ΔL is negligible compared to the overall structure length. The corresponding dimensions are summarized in Table 5.2.

Table 5.2: Dimensional parameters of mirror assembly distribution, based on optimizations ran by Aditya Garde & Henk Hoevers (Garde and Hoevers [63]).

Parameter	0.01 m Baseline	0.10 m Baseline	1.00 m Baseline
X	3.5 m	7.0 m	15.0 m
L	3.0 m	3.1 m	2.2 m
B	0.5 m	3.9 m	12.8 m

At this stage, two different mass distribution concepts are evaluated. The main difference is the location of the camera planes and the entrance mirror assemblies. In Configuration 1 (Figure 5.6a), all camera planes are located at the spacecraft bus, whereas in Configuration 2 (Figure 5.6b) the entrance slits and M1/M3 mirror assemblies remain at the spacecraft tip. Combining both configurations would lead to unrealistically low grazing angles for the mirrors, and is thus not feasible.

Keeping the camera planes near the spacecraft bus offers several practical advantages. It minimizes electrical harness lengths, reduces risk of thermal radiation from the cameras towards the optical elements and structures, and it keeps a larger part of the spacecraft mass close to the launch vehicle. The main disadvantage is that additional optical solutions are required to relocate the entrance mirrors closer to the spacecraft bus.

The assigned masses are first-order estimates based on comparable mirror assemblies from the Athena mission. Based on internal discussions, a total mirror assembly mass equal to twice the Athena mirror mass was adopted, resulting in a total mirror mass of 532 kg. An additional 250 kg was allocated for mirror mounts and support structures. The mass was distributed uniformly over the M1/M3 and M2/M4 assemblies, resulting in 130.33 kg per mirror combination. Additionally, each camera plane was assigned an arbitrary 50 kg. The resulting mass distributions for both configurations are shown in Figure 5.6.

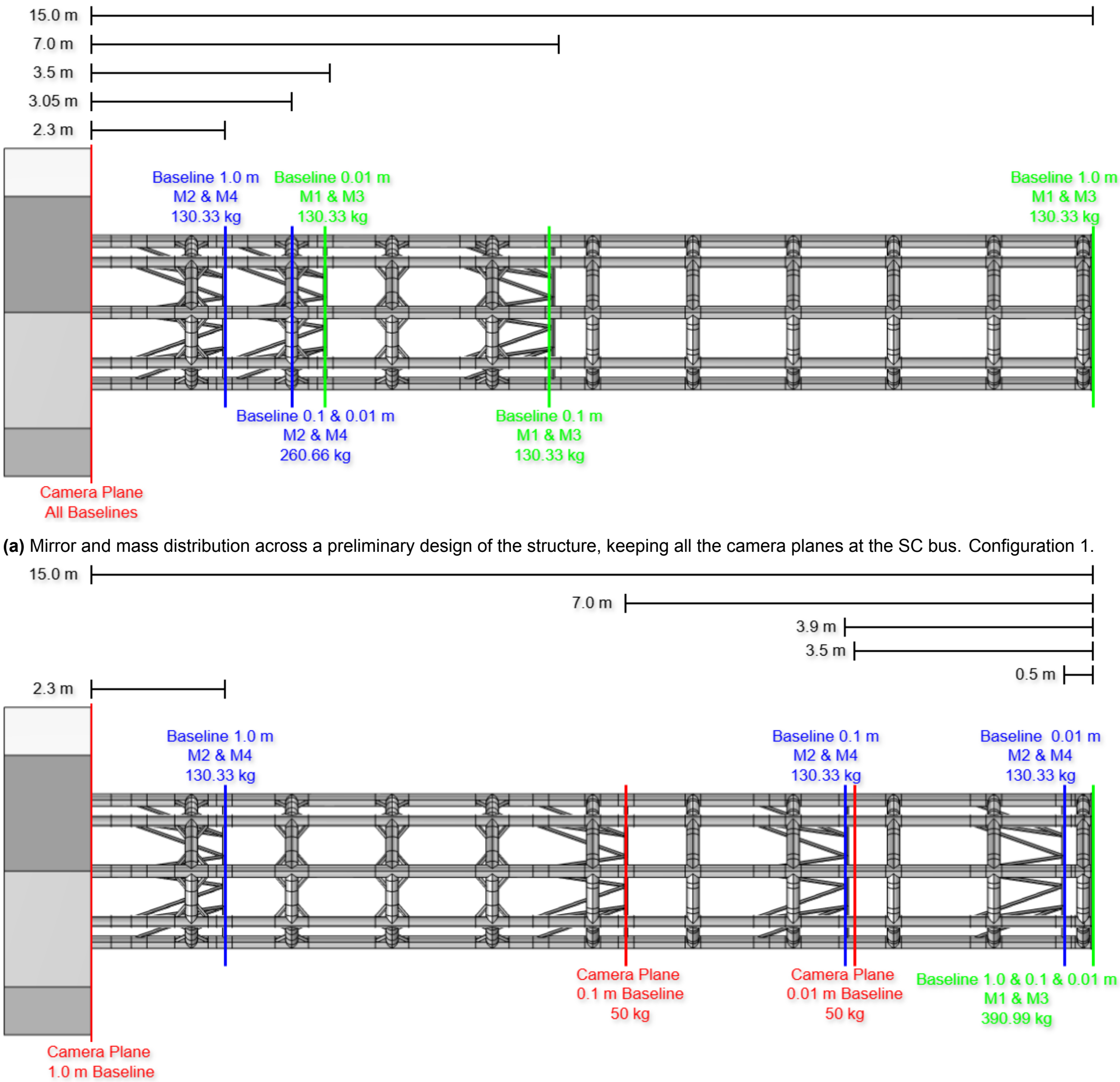

(a) Mirror and mass distribution across a preliminary design of the structure, keeping all the camera planes at the SC bus. Configuration 1.

(b) Mirror and mass distribution across a preliminary design of the structure, keeping all the entrance slits at the tip of the spacecraft. Configuration 2.

Figure 5.6: Two different options for mass distribution and mirror assembly integration into the spacecraft, differing regarding the camera planes and/or the entrance slits/mirrors for different baselines.

Both configurations were subsequently evaluated under the aerodynamic and end-of-flight launch loads, as well as through eigenfrequency analyses.

The comparison showed that Configuration 2 significantly degrades the structural behaviour of the spacecraft. While Configuration 1 is within the limits of the CoG requirement (HR-007), the CoG of the second configuration does not satisfy the requirement at this stage. The acceptable range according to the Ariane 6 manual, for a 6.9 tonne spacecraft is:

$$0.2 + 0.14 \times M < H_{CoG}\ [m] < 2.85 + 0.2 \times M \quad (5.3)$$

$$1.166\ [m] < H_{CoG}\ [m] < 4.230\ [m] \quad (5.4)$$

Configuration 2 also performs significantly worse during the aerodynamic launch phase. The maximum stresses increase by 51% relative to Configuration 1, fairly exceeding the allowable compressive and tensile design limits of 254 MPa (compressive) and 533.76 MPa (tensile) for M40J/PMT-F33. The maximum lateral tip deflection increases by 158% to 209.55 mm, exceeding the allowable limit of 125 mm. Additionally, the critical buckling factor decreases by 42.4% to 1.75, below the minimum required value of 2.0. Lastly, the fundamental lateral eigenfrequency decreases by 43.2% to 2.21 Hz, substantially below the required minimum of 6 Hz.

Based on these results and further internal discussion, Configuration 1 was selected as the baseline mass distribution for the remainder of the detailed design phase.

5.4. Detailed Design Methodology

The design methodology during the detailed design phase can be described as an iterative requirement-driven structural refinement. During the process, parameters are often individually, or in small batches, adjusted and optimized to obtain satisfactory performance for specific requirements. These parameters are identified and summarized in Table 5.3, with each parameter's structural purpose. The detailed design approach is illustrated as flow diagram in Figure 5.7.

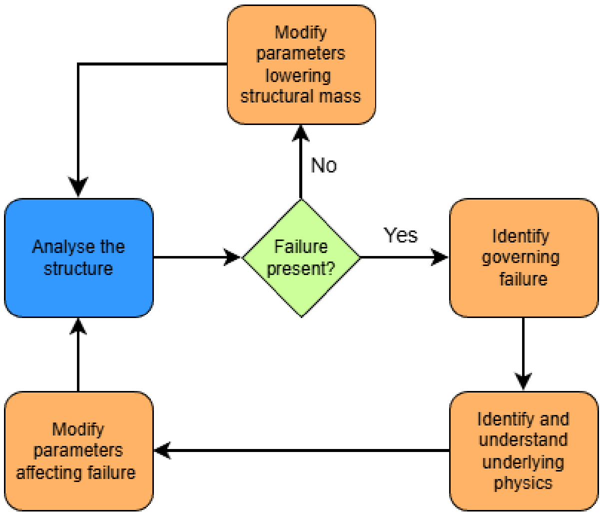

Figure 5.7: Flow diagram of the detailed design approach, showing the requirement-driven iterative design process.

The detailed design process contains six phases as identified and described below:

1. **Global structural model –** which started from the final conceptual design and focussed on the global parameter refinements. This includes the number of support rings, beam diameters, and wall thicknesses. The objective of this phase is to increase the eigenfrequency and buckling performance, while still aiming for minimized mass.
2. **Local stress refinement –** which focussed on the stress concentrations as a result of the launch loads. Initially these local refinements focussed on the reinforcement of the support rings with several structural solutions implemented and evaluated to reduce stress at the interfaces of the support rings and longitudinal beams.
3. **Beam/bus interface refinement –** which focussed on the reduction of stress concentrations at the interface of the spacecraft bus and the longitudinal beams, as that became the governing stress location.
4. **Realistic mass implementation –** which introduced the mass distribution of the mirror assemblies across the longitudinal locations as indicated in Figure 5.6a. Structural behaviour changed drastically as a result, requiring further refinement and structural reinforcements.
5. **System integration –** which introduced additional structures such as the lid, mylar blanket, and solar panels for the thermal analyses, as well as the solar panel's affect on the structural behaviour.
6. **Additional structural configuration –** which is a parallel design during the detailed design phase, focussed on increasing the utilized area/volume inside the Ariane 64 fairing. The design implements a multi-octagon structural approach.

Table 5.3: Identification of design parameters and their structural purpose during the iterative design approach.

Parameter	Purpose
Main beam diameter	Governs the global bending stiffness, second moment of inertia, load-carrying capacity, and influences the lateral eigenfrequency.
Main wall thickness	Dominates the axial and bending stiffness, controls buckling resistance, stress levels in shell elements, and has a large mass penalty.
Support ring diameter	Defines the lateral support span of the longitudinal beams, influences global stiffness distribution, and affects buckling mode shapes.
Support ring thickness	Contributes to local stiffness at beam intersections, reduces local deformation and stress concentrations, and increases joint rigidity. Increases support ring buckling resistance.
Number of support rings	Controls the global structural stability, suppresses global and local buckling, and increases load redistribution across the structure.
Support ring spacing	Determines the effective buckling length of the longitudinal beams, influences stress distribution between structural elements, and affects the eigenfrequencies.
Diagonal members	Introduce shear load paths, increase torsional stiffness, improve global stability against lateral loads, and suppress asymmetric deformation modes.
Diagonal member diameter	Controls stiffness contribution of diagonal load paths and influences mass efficiency against torsional rigidity.
Diagonal member thickness	Governs local stiffness and buckling resistance of diagonal struts.
Cross-volume structures	Provide a load redistribution between structural elements, increase global stiffness, and offer a platform for mirror assembly mass distribution.
Local ring reinforcement	Reduces stress concentrations at the beam-ring intersections and improves joint stiffness.
Local SC bus reinforcement	Reduces stress transfer concentrations between the structure and the SC bus, improves boundary condition stiffness realism, and increases lateral eigenfrequency.
Solar panel inclusion	Introduces distributed mass along the structure, affects eigenfrequency behaviour, and creates additional bending and torsional load paths.
Number of solar panel brackets	Defines discrete load paths between panels and the structure, influences local stress concentrations, and affects dynamic coupling between panels and structure.

To allow for justifiable design choices, the effectiveness of individual structural support options can be quantified, highlighting the structural performance of different options. The individual assessed components are discussed in more detail in section 5.5.

The lateral eigenfrequency has been identified as the main structural design driver during the detailed design phase, hence the individual effectiveness assessment has been performed against the lateral eigenfrequency. The structural effectiveness can be seen in Figure 5.8, providing insights into each support option regarding their benefits and their mass costs. These insights, in combination with the design approach, form the foundation of the choices made to obtain the final configurations, as discussed in section 5.6 and section 5.7.

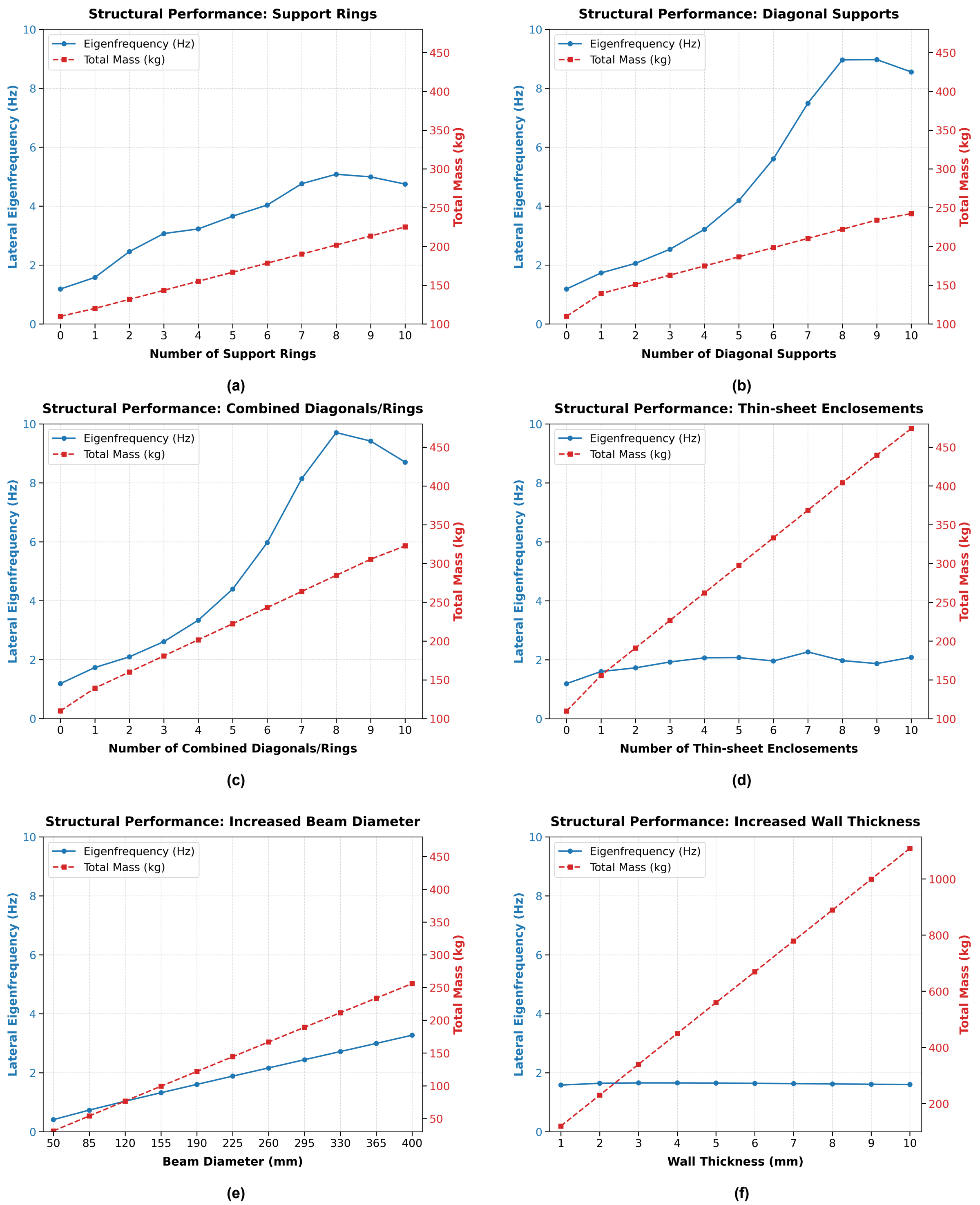

Figure 5.8: Structural performance of different support structures, quantifying the effectiveness of reinforcement options. Applied to the M40J/PMT-F33 structure with an longitudinal outer beam diameter of 187.2 mm and a wall thickness of 1 mm. The support rings, diagonals, and GFRP thin-sheet are summarized in Table 5.6. All options have been investigated regarding their influence on lateral eigenfrequencies. **a)** Structural effectiveness of 0 – 10 support rings, the first ring is placed at the tip, the second at the middle, and the remaining from the bottom upwards. **b)** Effectiveness of diagonal struts in 'diamond' pattern around the structure, starting at the bottom going upwards. The first addition also included the top support ring for convergence purposes. **c)** Effectiveness of a combination of support rings and diagonal structures. The first addition included the top support ring and bottom diagonal, going upwards hereafter. **d)** Structural effectiveness of 2 mm GFRP, representing the substrate of solar panels. The additions are from bottom to top, with the top support ring already included in the first addition. **e)** Effectiveness of increasing the beam diameter of the longitudinal beams. Assessment includes the top ring from the start. **f)** Effectiveness of increasing the longitudinal beam wall thickness, including the top support ring at all times.

5.5. Individual Component Design

The detailed design is developed by considering the individual structural components separately before integrating them into the complete spacecraft assembly. This approach allows for each component to be designed according to its primary structural purpose, allowing for a modular and parametric design approach. The following sections discuss the main design considerations, including the CFRP/Aluminium connection, the simplified spacecraft lid, the support rings, diagonal structures, and cross-volume structures, as well as the integration of the multi-layer insulation (MLI) and the solar panels.

5.5.1. CFRP/Aluminium Connection

Connecting thin-walled circular CFRP beams to a perpendicular aluminium surface is a challenging problem for the structural integration. Throughout the COMSOL analyses, these connections have thus been modelled as rigid connections to the SC bus. In practice, a dedicated connection has to be designed to maintain sufficient stiffness while ensuring reliable load transfer between the CFRP structure and the aluminium bus. A preliminary design for such a connection is shown in Figure L.1 and is described in detail in Appendix L.

The proposed connection is based on a similar concept developed for the multi-stage geometric anti-spring (GAS) vibration isolation system of the Einstein Telescope. A demonstrator is currently being developed at Leiden University (Langendorff [64]). The connection uses a combination of LOCTITE Stycast 2850 FT and CAT 9 adhesive. This adhesive is suitable for cryogenic temperatures and satisfies the spacecraft outgassing requirements HR-014 & HR-015, with a TML of 0.25 % and a CVCM of 0.01 %. Additionally, it has CTEs of 35.0 ppm and 98.9 ppm, a glass transition temperature of 86 °C, and a density of 2.29 g/cm^3 (Henkel Corporation [65]).

Preliminary launch analyses indicate stress concentrations at the interface between the longitudinal beams and the SC bus, where the maximum bending moment occurs under lateral acceleration. Rather than explicitly modelling the entire connection geometry, the behaviour has been approximated by locally reinforcing the first two 300 mm sections of the longitudinal beams adjacent to the SC bus. These locally increased wall thicknesses provide a representative approximation of the increased stiffness introduced by the connection while limiting the COMSOL modelling complexity.

5.5.2. Spacecraft Lid Design

At the current stage of the study, a detailed spacecraft lid design is not required, nor possible, as the final baseline distribution and several subsystem interfaces have yet to be defined. The primary purpose of the simplified lid design is therefore: to represent the payload mass located at the spacecraft tip and to provide a closed upper surface for the evaluation of the aerothermal flux on the spacecraft after fairing separation.

To satisfy these objectives, a simplified aluminium lid is modelled, as shown in Figure 5.9. The lid consist of a hollow box with a uniform wall thickness of 3 mm, representing a realistic configuration that could open after launch. At the current stage, this simplified representation is sufficient to capture both the structural contribution of the lid as its influence on the thermal behaviour.

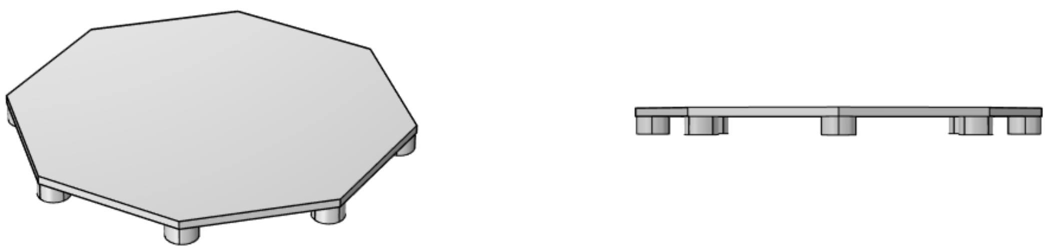

Figure 5.9: Simplified spacecraft lid design, made out of aluminium, with an overall wall thickness of 3 mm all around. The lid is modelled as a hollow box to represent a design that could open its doors after launch.

5.5.3. Support Rings and Diagonal & Cross-Volume Structures

Several different types of support structures are evaluated in the detailed design phase, of which the supporting structures, depicted in Figure 5.10, are present in one of the final designs. These structures are modelled as individual geometrical elements, applying a parametric approach that allows quick adjustments of parameters such as thickness or diameters.

Figure 5.10a shows the basic support ring that is locally reinforced to avoid the stress concentrations at the interface of the horizontal ring section and the vertical sleeve section that overlaps with the longitudinal beam.

In Figure 5.10b, a similar support ring structure is shown that is not locally reinforced, but rather includes diagonal support trusses that connect to receiving sockets on the ring above. These diagonal beams are similar thin-walled beams that can be altered in diameter, angle, and thickness.

Figure 5.10c depicts the same principle as Figure 5.10b, but without the horizontal beam elements that make it a singular ring. This support structure contains four individual vertical sleeves with diagonal beams to minimize the mass in certain sections of the global architecture.

Figure 5.10d shows the cross-volume structure that is implemented in the final design at the location where the mirror masses cannot be directly distributed to surfaces at the right longitudinal location. It acts as a first conceptual step towards the integration of optical benches and the connection to mirror assemblies. The horizontal beams of this structure can be used to distribute the mirror mass across, while the diagonal beams are meant as load-bearing beams.

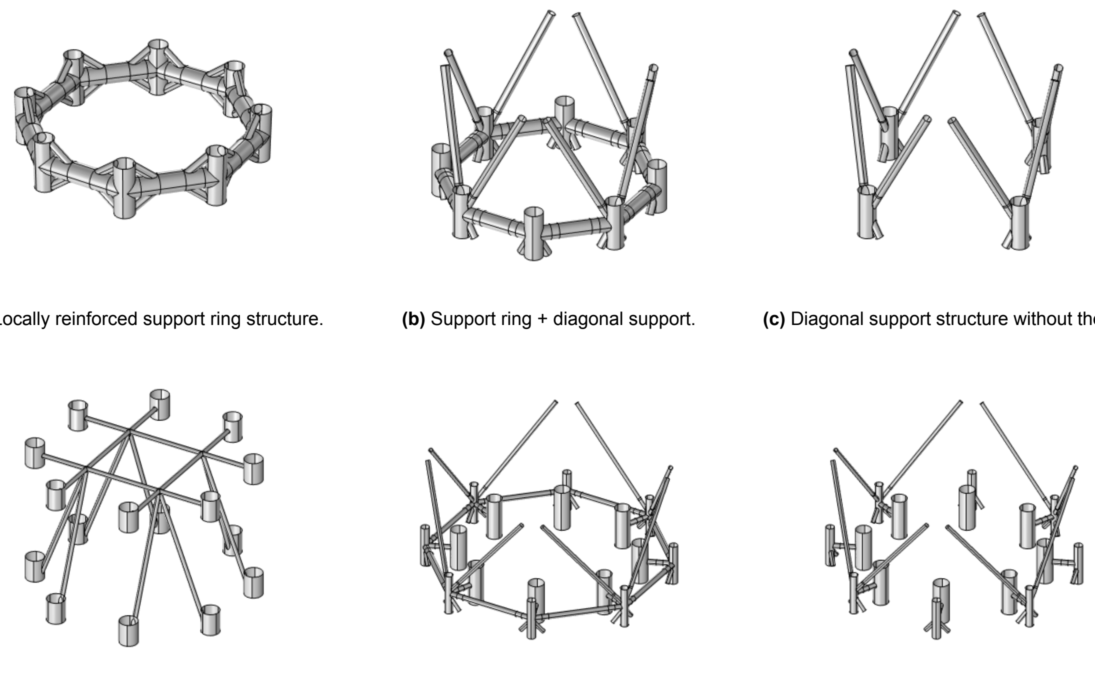

(a) Locally reinforced support ring structure. **(b)** Support ring + diagonal support. **(c)** Diagonal support structure without the ring.

(d) Cross-volume structure. **(e)** Support ring + diagonals (outer octagons). **(f)** Diagonal support (outer octagons).

Figure 5.10: The six different support structures that are implemented during the final design phase and are present in either of the final detailed design models.

The last two images, Figure 5.10e & Figure 5.10f, are specific to the final design that utilizes multiple octagonal structures, as can be seen in Figure 5.1b. The structural purpose of this design is to increase the structural performance by adding more structures around the base. To connect the outer and inner octagons, the previous support ring designs, including diagonals, need to be adjusted to connect with the other octagons.

5.5.4. Mylar and Solar Panels

Before thermal analyses can be evaluated, additional properties have to be determined regarding emissivity and absorptivity. These can differ based on the material, coating, and the colour. The determination and approximation of properties can be found in Appendix N, with summarized properties in Table 5.4.

Table 5.4: Summary of applied solar absorptivities and IR emissivities.

Component / Boundary	Material	Solar Absorptivity (α_{abs})	IR Emittance (ϵ)
Multi-layer insulation (MLI)	Aluminized Teflon Aluminized Kapton	Outer layer: 0.20 Inner layers: 0.15 Inner-most layer: 0.45	Outer layer: 0.80 Inner layers: 0.04 Inner-most layer: 0.71
Spacecraft bus (bottom surface)	AZ-93 Paint	0.15	0.91
Spacecraft bus (remaining exposed surfaces)	MLI	See row 1	See row 1
Spacecraft lid	Anodized Aluminium	0.27	0.76
Solar panels (front side)	GFRP + Solar Cells	0.5892	0.816
Solar panels (rear side)	GFRP	0.51	0.75
Structural beams	CFRP	0.90	0.85

Multi-Layer Insulation
To include the thermal insulation in the COMSOL model, without physically modelling each individual layer, the MLI is approximated as a single shell while utilizing the radiation shielding node in COMSOL. This allows for the definition of radiative MLI properties per individual layer.

The following assumptions are made:

- Vacuum is assumed between the layers, resulting in negligible gas conduction ($k_{\text{gas}} = 0$).
- The spacer material is neglected for both the structural behaviour, thermal behaviour, and mass estimation.
- The MLI does not contribute to the global structural stiffness and is therefore decoupled from the spacecraft for structural assessment.
- Thermal properties are represented using orthotropic in-plane ($\|$) and through-thickness ($\perp$) directions.

A MLI configuration of 17 layers in total is assumed, as is a common configuration (Gilmore [66]). The outermost layer (sun-facing) consist of a 254 μm thick layer of aluminized Teflon fluorinated ethylene propylene (FEP) film. The inner 15 layers are 50.8 μm thick single-aluminized Kapton films. The innermost layer is commonly a 50.8 μm thick double-aluminized Kapton film (Gilmore [66]). The absorptivity and emissivity properties have been described in Appendix N. The total solid material thickness can be determined as follows:

$$t_{\text{solid}} = (1 \times 254 \times 10^{-3}\ \text{mm}) + (15 \times 50.8 \times 10^{-3}\ \text{mm}) + (50.8 \times 10^{-3}\ \text{mm}) = 1.0668\ \text{mm} \tag{5.5}$$

Assuming a total MLI thickness of 5 mm, the solid volume fraction then becomes:

$$\phi_{\text{solid}} = \frac{t_{\text{solid}}}{t_{\text{total}}} = \frac{1.0668\ \text{mm}}{5.0\ \text{mm}} = 0.21336 \tag{5.6}$$

The effective density scales directly with the solid volume fraction:

$$\rho_{\text{eff}} = \phi_{\text{solid}} \cdot \rho_{\text{pure}} = 0.21336 \times 1390\ \text{kg/m}^3 = 296.57\ \text{kg/m}^3 \tag{5.7}$$

The specific heat capacity is normalized by mass and the vacuum layers do not contribute to the thermal mass, the effective specific heat capacity is assumed to be:

$$C_{p,\text{eff}} = C_{p,\text{raw}} = 1172.3\ \text{J/(kg} \cdot \text{K)} \tag{5.8}$$

To prevent the MLI from artificially increasing the structural stiffness of the spacecraft, an artificial Young's modulus of 1 MPa is assigned, together with a Poisson's ratio of 0.

These equivalent material properties allow for the thermal influence of the MLI to be included in the thermal analyses while preventing the insulation from introducing stiffness into the model.

Solar Panels
The solar panels have both a thermal and a structural functionality, during thermal analyses it is meant to shield the structure from incoming radiation, while also radiating towards the MLI. During the structural analyses the solar panels are introducing additional rigidity, while also adding mass to the model.

The solar panels are modelled as 1.5 m long panels with a width of 0.8 m and a thickness of 2 mm. Similarly to the MLI blanket, the panels are modelled as shell surfaces to which the properties of glass-fibre reinforced polymer (GFRP) have been assigned. GFRP is a common solar panel substrate, with the properties as defined in Table 5.5 (Blom [67]).

Table 5.5: Isotropic GFRP material properties as provided by the Ansys database and extracted from Blom [67].

Material	Density [kg/m^3]	CTE [10^{-6}/K]	Young's Modulus [GPa]	Heat Capacity [J/(kg·K)]	Poisson's Ratio [–]	Thermal Cond. [W/(m·K)]
GFRP	1800	$\parallel = 8.64$ $\perp = 33.0$	20.0	1000	0.315	$\parallel = 0.55$ $\perp = 0.45$

To gain insights into the potential power generation of the solar panels, a brief approximation can be done to quantify how much power can be generated at any time. The relevance of this insight is that it dictates how many solar panels are required and whether the entire spacecraft should be covered or whether less panels would be sufficient. With the provided length and width of a single octagon face, the area of a single side is given as:

$$A_{\text{face}} = 11.96 \text{ m}^2 \tag{5.9}$$

Given the octagonal shape, the total surface area of all faces is:

$$A_{\text{total}} = 8 \cdot 11.96 = 95.68 \text{ m}^2 \tag{5.10}$$

Due to the orientation of the panels relative to the incident sunlight, the effective projected area (A_{proj}) is calculated using a geometric correction factor for a 45° inclination:

$$A_{\text{proj}} = A_{\text{face}}\,(1 + 2\cos 45^\circ) = 11.96 \cdot (1 + 2 \cdot 0.7071) \approx 28.88 \text{ m}^2$$

Assuming an active surface cell coverage of 90%, the actual active solar cell area (A_{active}) is:

$$A_{\text{active}} = A_{\text{proj}} \cdot 0.90 = 28.88 \cdot 0.90 \approx 25.99 \text{ m}^2 \tag{5.11}$$

Finally, the total electrical power output (P) is calculated by multiplying the solar irradiance (1361 W/m^2), the active area, and the solar cell efficiency. The solar cell efficiency is taken from multi-junction GaAs solar cells, with an efficiency of 35% (Blom [67]).

$$P = 1361 \cdot A_{\text{active}} \cdot 0.35 = 1361 \cdot 25.99 \cdot 0.35 \approx 12384 \text{ W} \approx 12.4 \text{ kW}$$

5.6. Single-Octagon Detailed Design Assembly

Based on the iterative methodology described in section 5.4 and the individually modelled components as shown in section 5.5, upwards of 50+ iterations have been assessed. With the lateral eigenfrequency as the main design driver behind iterations and reinforcement options. The final design, as shown in Figure 5.1a, is obtained with the parameter definition as summarized in Table 5.6. A visualization of where these parameters belong in the structure can be found in Appendix M, Figure M.1a.

Based on the performance indications as shown in Figure 5.8, the choice was made to use the combined structural support rings with their diagonal reinforcements as initial start. As a quantification of the structural performance with respect to the reinforcement location is difficult, the first major iteration included all 10 of the support structures. Including the proper mass distribution, the eigenfrequency requirement was not yet so easily obtained, requiring further refinement of the structural configuration. Logical choices led to the removal of mass located higher in the structure, leading to the elimination of several support rings at the top, while maintaining the diagonal supports.

While Figure 5.8 indicates that the diagonal support structures have a clear advantage over the support rings regarding the lateral eigenfrequency, a total of 6 support rings were maintained. These rings showed, through several iterations, to be valuable for the lateral eigenfrequency, but even more important to the load distribution under lateral accelerations. These rings ensure that the load is properly distributed and transferred to other structural components, such as the longitudinal beams.

The most lower support ring contains local reinforcements, with relatively small diagonal struts local to the ring. These are kept instead of the global diagonal support structures, as iterations indicated limited effect of the global diagonal supports in those specific locations in this configuration. Similarly, the lower support rings experience the highest local stresses during the aerodynamic and EOF phases, and thus require a local solution.

A total of three cross-volume structures are maintained, as they proved valuable interfaces for the mirror assembly mass distributions, while only adding limited mass. The structural advantages of these structures is not necessarily for the global behaviour, but rather for the local load distribution of the mirror masses to the longitudinal beams. The current preliminary design of these cross-volume structures is not further developed into highly detailed designs as the baseline choices and distribution is as of yet unknown.

A total of 8 global diagonal support structures are implemented in the final configuration. Figure 5.8b and Figure 5.8c clearly show a preference for 8 diagonals or diagonal/ring combinations. Many additional iterations have been assessed with more/less than 8 diagonal support sections, while the location has been assessed in these iterations as well. The COMSOL iterations confirmed the preferred inclusion of 8 global diagonal support structures in the locations as shown in Figure 5.1a.

The final structural configuration is obtained after a minimum 7.0 Hz lateral eigenfrequency is met to create an acceptable margin to the minimum 6.0 Hz that is imposed as hard requirement (HR-002). The structural configuration at this stage has a mass of 655.05 kilogram for a lateral eigenfrequency of exactly 7.00 Hz.

Additional iterations are executed to gain insights into the effects of the solar panels on the structure. The solar panels, as described in subsection 5.5.4, are placed around the entire spacecraft and have been connected to the structure through COMSOL line elements. These line elements have been given high mechanical properties to artificially simulate a rigid bracket connection between the spacecraft structure and the solar panels. The solar panels have a double-sided effect, of which the first is additional mass distributed along the spacecraft structure. The mass is based on only the 2 mm GFRP substrate, without the solar cells, electrical harnessing, or other subsystems. The second effect of the added solar panels is additional rigidity to the structure. Figure 5.8d clearly indicates that, regarding the lateral eigenfrequency, the added mass almost balances out the added rigidity. This results in a high mass cost, without gaining much structural advantage. The logical conclusion would be to limit the amount of solar panels to the minimum acceptable number regarding power consumption and production throughout the expected operational lifetime. In addition to this observation, the placement of the solar panels should be as close to the SC bus as possible to avoid negative structural influence.

The wall thickness of the longitudinal beams is another parameter assessed against its mass costs. As can be seen in Figure 5.8f, the additional mass of this increased wall thickness goes up significantly more than with any other support structure, quickly reaching 1000+ kg. It is important to notice that the results depicted in Figure 5.8f are based on a bare structure of 8 beams and a single top support ring. Many iterations on complex configurations show that increased wall thickness can be beneficial in combination with support structures. An effective compromise is to locally reinforce the wall thickness of the longitudinal beams at the interface with the SC bus, reducing stress concentrations and increasing the lateral eigenfrequency at a fairly limited mass cost.

Lastly, the effectiveness of the longitudinal beam diameter is quantified, as depicted in Figure 5.8e. It shows a steady correlation between the lateral eigenfrequency and an increased diameter, where the mass increases under a steeper slope than the eigenfrequency. The lateral eigenfrequency is not the only important factor that the beam diameter has an influence on, with the obstructed area/volume weighing heavy in the diameter choice. A smaller diameter would be beneficial for the available area/volume. Due to time restrictions, the final beam diameter of the longitudinal beams is kept at the resulting diameter of the conceptual phase, 187.2 mm.

5.7. Multi-Octagon Detailed Design Assembly

The design as shown in Figure 5.1b, is a further improvement on the single-octagon structural configuration. This multi-octagon configuration utilizes three octagonal structures that are connected to the spacecraft bus, as well as to each other. Several assumptions are made for this design, for example the selection of baselines, 0.01 m, 0.1

m, and 1.0 m. These are the same baselines as considered in section 5.3, and they are considered for the same reasons as explained previously.

The baseline choice dictates the length of each octagonal structure, with the main 15 m long, 2.33 m wide structure reserved for the 1.0 m baseline, the 7.5 m long structure for the 0.1 m baselines, and the 3.5 m long outermost octagonal structure for the 0.01 m baseline. The diameter of the two additional octagonal structures are taken to ensure a roughly equal area distribution, while maintaining an additional 1.0 m clearance to the outermost edge of the spacecraft. This is assumed reasonable to allow for additional systems such as star trackers to be placed around the structure. The effective diameter of the two outer octagons have been assumed equal at this stage, with an outermost diameter of 3.90 m and an intermediate diameter of 3.115 m. A top view visualization of the octagonal area distribution can be seen in Figure 5.11a, with a top view of the multi-octagon COMSOL model shown in Figure 5.11b.

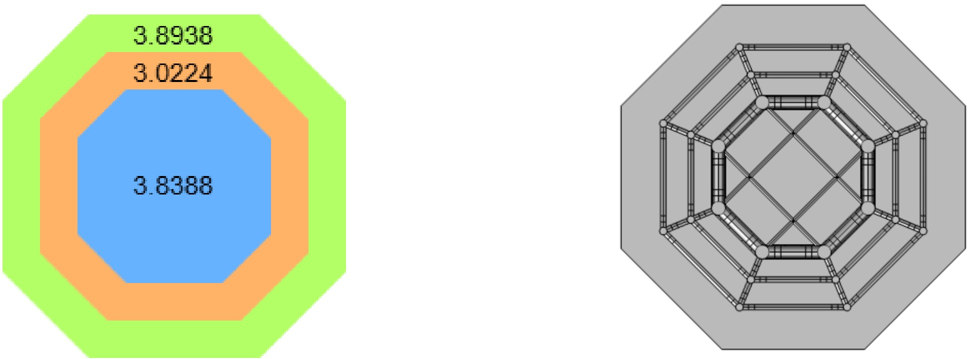

(a) (b)

Figure 5.11: a) Schematic overview of the multi-octagon area distribution. Values within their respective colours indicate the available area of each octagon. The areas are in m^2. **b)** Top view image of the multi-octagon COMSOL model, showcasing the three separate available cross-sectional areas, as well as showing the area/volume obstructed by structural elements.

The design approach is similar to the single-octagon structure, with less refinement and in-depth iterations due to time restrictions. After obtaining the final configuration assembly as discussed in section 5.6, the same principles are applied to the two outer octagons. They both have a combination of support rings and diagonals with reduced overall dimensions such as beam diameters and beam thicknesses. Additionally, and most advantageously, the added rigidity and stiffness closer to the spacecraft bus allows for a more rigid base of the structure, which then allows for the removal of mass near the top single-octagon section by reducing the beam thickness. Essentially, more mass is moved to lower sections of the structure while adding rigidity and global stiffness. The parameter differences can be seen in Figure M.1b, with a summarized table of the final parameters in Table 5.6. The results and comparison between the single-octagon and multi-octagon configurations are discussed in chapter 6.

5.8. Conclusion

The resulting concept from the conceptual design phase is further developed into a detailed structure through the iterative, requirement-driven design approach. From this detailed design phase, it can be concluded that the lateral eigenfrequency is the most difficult mechanical requirement to satisfy at this stage of the design, with the single-octagon structure showing an eigenfrequency of 7.0 Hz. As the requirement (HR-002) dictates a bare minimum eigenfrequency of 6.0 Hz, the single-octagon is considered marginally acceptable, while the multi-octagon configuration outperforms its single counterpart, with an eigenfrequency of 8.15 Hz. The structural effectiveness of individual support structures shows that a combination of support rings and diagonal struts provides the most efficient contribution to an increased lateral eigenfrequency. Increased longitudinal beam diameter has a significant, positive, influence on the lateral eigenfrequency as well, but is limited by the obstructed area/volume of these beams. An increase in structural volume directly limits the available volume for scientific instruments, hence the diameter has been maintained at the 187.2 mm resulting from the conceptual design. Increasing the longitudinal beam wall thickness shows a near-zero effect on the lateral eigenfrequency, while carrying a disproportional mass penalty compared to any other reinforcement option. Hence, wall thickness increases are only implemented locally, or globally when driven by the improved load distribution. Regarding the solar panels, it can be observed that their added mass and rigidity nearly cancel each other out when covering the entire spacecraft in solar panels. For mechanical performance, and provided that the power budget allows it, it would be beneficial to cover the spacecraft only partially, preferably on the lower half. From the mass distribution comparison, it can be concluded that keeping all camera planes at the SC bus (Configuration 1) is favoured over relocating the camera planes into the structure (Configuration 2). For thermal behaviour and mechanical performance, Configuration 1 is clearly the better option, with Configuration 2 also not satisfying the CoG requirement (HR-007). The detailed design phase resulted in four different configurations, SO-BR, SO-HP, SO-FP, and MO-BR. The MO-BR configuration is preliminarily identified as the best performing configuration, showing better static and dynamic behaviour, while satisfying launch constraints.

Table 5.6: Parameter definitions and comparison between the single-octagon and multi-octagon structural configurations.

Single-Octagon Configuration		**Multi-Octagon Configuration**	
Part	**Parameter Description**	**Part**	**Parameter Description**
Longitudinal beams	Diameter = 187.2 mm Thickness = 4 mm	Longitudinal beams	Diameter = 187.2 mm Thickness = 2 mm
Spacecraft lid	Hollow Wall thickness = 3 mm Mass = 130.33 kg	Spacecraft lid	Hollow Wall thickness = 3 mm Mass = 130.33 kg
Upper support ring	Diameter = 120 mm Thickness = 1.5 mm	Upper support ring	Diameter = 120 mm Thickness = 1.5 mm
Vertical sleeve sections	Diameter = 187.2 mm Thickness = 5.5 mm	Vertical sleeve sections	Diameter = 187.2 mm Thickness = 3.5 mm
Global diagonal beams	Diameter = 42.5 mm Thickness = 2 mm	Global diagonal beams	Diameter = 42.5 mm Thickness = 2 mm
1^{st} support ring	Ring: Diameter = 93.6 mm Thickness = 1.5 mm Local support: Diameter = 37.44 mm Thickness = 2.5 mm	1^{st} support ring	Ring: Diameter = 93.6 mm Thickness = 1.5 mm Local support: Diameter = 37.44 mm Thickness = 2.5 mm
2^{nd} – 5^{th} support ring	Diameter = 78.6 mm Thickness = 1.5 mm	2^{nd} – 5^{th} support ring	Diameter = 78.6 mm Thickness = 1.5 mm
Cross-volume structures	Diameter = 50 mm Thickness = 3 mm	Cross-volume Structures	Diameter = 50 mm Thickness = 3 mm
Beam / SC bus connection	Lower 300 mm: Thickness = 5 mm Upper 300 mm: Thickness = 5 mm	Beam / SC bus connection	Lower 300 mm: Thickness = 4 mm Upper 300 mm: Thickness = 3 mm
–	–	Longitudinal beams (outer octagons)	Diameter = 100 mm Thickness = 3 mm
–	–	Support rings (outer octagons)	Diameter = 35 mm Thickness = 1.5 mm
–	–	Vertical sleeve sections (outer octagons)	Diameter = 187.2 mm Thickness = 4.5 mm
–	–	Global diagonal beams (outer octagons)	Diameter = 25 mm Thickness = 2 mm
–	–	Horizontal connection to inner octagon	Diameter = 35 mm Thickness = 1.5 mm
–	–	Beam / SC bus connection (outer octagons)	Lower 300 mm: Thickness = 5 mm Upper 300 mm: Thickness = 4 mm

6 Results & Discussion Detailed Design

This chapter presents the results and the following discussion of several analyses evaluated on the detailed designs. The analyses are done for the configurations discussed in chapter 5, and depicted in Figure 5.1. Additional analyses and results are presented based on several sidetracks that have been (briefly) explored, such as the structural analyses with limited solar panel coverage. Visualizations of these additional models can be found in Appendix J, Figure J.1a & Figure J.1b. The many results of intermediate quick iterations have not been presented, with major changes or observations briefly explained. The chapter discusses the results of the static launch accelerations analyses, the eigenfrequency analyses, the vibrational analyses, the micrometeoroid impact analyses, and the thermal analyses. The chapter finishes with the verification of these results against the requirements, including a discussion on why requirements are satisfied or not.

Table 6.1: Summary of structural metrics analysed during the static load cases, representative for two critical launch environment phases. Evaluated for four different structural configurations.

Property	Launch Phase	Unit	Single-Octagon Bare	Single-Octagon Full Panels	Single-Octagon Half Panels	Multi-Octagon Bare
Max. induced stress	Aero	MPa	355.44	278.97	241.56	198.95
Margin of safety *	Aero	–	-0.285	-0.090	0.051	0.277
Max. induced stress	EOF	MPa	203.86	167.52	144.95	114.71
Margin of safety *	EOF	–	0.246	0.516	0.752	1.214
Max. tip displacement	Aero	mm	26.87	33.48	21.15	20.09
Max. tip displacement	EOF	mm	14.93	18.61	11.76	11.17
Critical buckling factor	Aero	–	9.64	0.11	0.134	10.73
Critical buckling factor	EOF	–	15.46	0.16	0.186	18.02
Lateral eigenfrequency	–	Hz	7.0189	7.0344	7.9558	8.1478
Longitudinal eigenfrequency	–	Hz	40.247	Unknown **	Unknown **	39.703
Structural Mass	–	kg	655.08	1009	832.64	640.99
Total spacecraft mass ***	–	kg	2937.08	3291	3114.64	2922.99
Center-of-mass (Z-coordinate)	–	m	2.842	3.638	3.000	2.390

* Margin of Safety (MoS) is calculated based on the quasi-isotropic laminate properties as shown in Table 4.6 and according to the approach discussed in Appendix I. Design requirements specify MoS $\geqslant 0.0$, Max. Tip Displacement $\leqslant 125$ mm, and Critical Buckling Factor $\geqslant 2.0$.
** Values are unknown, as the majority of eigenfrequencies is occupied with local solar panel modes.
*** Includes 1500 kg of the SC bus, structural mass, and 782 kg for the mirror assemblies.

6.1. Static Launch Accelerations

The static launch accelerations discussed in section 4.1, and summarized in Table 5.1, are implemented into stationary COMSOL analyses for the aerodynamic phase and the end-of-flight phase. The three main metrics analysed in this section are the stress distribution, the tip displacement, and the critical buckling factor.

For the single-octagon configuration, a distinction can be made for three different cases. The first case is the bare structure as seen in Figure 5.1a. The second case is when the entire spacecraft is covered in solar panels, as discussed in section 5.6 and shown in Figure J.1b. The third situation is when the spacecraft is only covered in solar panels along the bottom 7.5 m, also discussed in section 5.6 and shown in Figure J.1a. All three of the configurations are based on the same bare structure, using the parameters as presented in Table 5.6.

For the multi-octagon configuration, the only static acceleration analysis evaluated is for the structure without any solar panels, thus only including the structure as presented in Figure 5.1b. Due to time limitations, additional analyses including solar panels are not feasible.

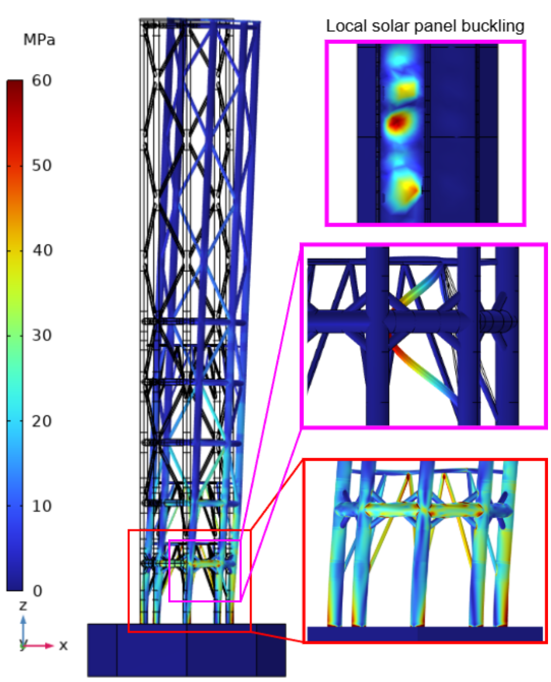

(a) Single-octagon structure after aerodynamic phase loading. Red box zoomed in on the most stress heavy region, depicting stress concentrations at the base, support ring, and cross-volume structure. Pink boxes show buckling modes and locations, either structural or local in the solar panel.

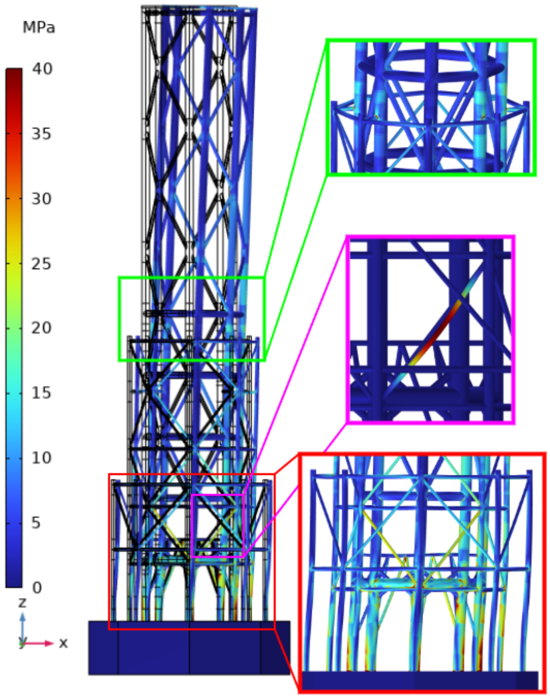

(b) Multi-octagon structure after aerodynamic phase loading. Red box zoomed in on the most stress heavy region, depicting stress concentrations at the base, support ring, and diagonal struts. The pink box shows the first buckling mode. The green box shows additional stresses.

Figure 6.1: Resulting single-octagon and multi-octagon structure after exposure to the aerodynamic phase of the launch profile. The main displacement has been visually scaled by a factor 25, whereas the buckling has been scaled by much larger factors. The maximum stresses correspond to Table 6.1, but for visualization purposes, the colour legends are adjusted to enable more detailed views.

6.1.1. Stress Distribution and Material Integrity

The static stress distribution across all the evaluated configurations is dominated by the aerodynamic phase load case, where combined longitudinal and lateral accelerations create a substantial bending moment at the spacecraft bus interface. As discussed in Appendix I, a 0.8 KDF is applied to the M40J/PMT-F33 material to obtain design limits. The KDF is applied to the values depicted in Table 4.6, resulting in $\sigma_t = 533.76$ MPa and $\sigma_c = 254$ MPa. The induced stress and corresponding MoS, as a result of the stationary COMSOL analyses, are summarized in Table 6.1.

Across all the configurations, the primary stress concentrations develop at the lower structural elements and at the interface where the lowest support ring transitions into the main longitudinal beams, as can be seen in Figure 6.1.

From the obtained stresses in the end-of-flight phase, it can be determined that all configurations have a positive MoS, with MoS > 0.3 considered to be acceptable, and 0.0 < MoS < 0.3 considered marginally acceptable. This is consistent with the assessment in subsection 4.6.2 and Appendix I.

During the aerodynamic phase, there is a clear distinction between the configurations:

- **Single-Octagon (Bare) –** experiences a peak stress of 355.44 MPa, which results in a negative (-0.285) MoS. According to the set acceptance criteria, this configuration will exceed the design limits during launch and thus potentially fail.
- **Single-Octagon (Full & Half Panels) –** integrating full solar panels around the structure reduces the peak aerodynamic stress to 278.97 MPa. While still resulting in a negative MoS, the panels offer load sharing and a reduced displacement. The upper panels introduce a significant bending mass, hence reducing the panel covered area to the lower 7.5 m (Half Panels) results in better performance. Half coverage results in a marginally positive MoS.
- **Multi-Octagon (Bare) –** demonstrates superior structural efficiency by optimizing the cross-sectional geometry and load distribution through internal diagonal struts and a reinforced base at the SC bus. The peak aerodynamic stress drops to 198.95 MPa, resulting in a MoS of 0.277, reaching the acceptance limits.

As can be seen in Figure 6.1a and Figure 6.1b, all the stress concentrations are in the lower regions and are fairly local. Hence these 'minor' exceeding stress peaks are not considered a major issue at this stage. These stress concentrations can relatively easily be avoided in further developments and with localized solutions. As the development process is still in its early phase, many more additions and adjustment might alter the load/stress distribution, limiting the importance of these local failures at this stage.

6.1.2. Displacement and Global Stiffness Performance

To ensure fairing dynamic clearance during launch, the maximum allowable lateral tip displacement is constrained to $0.5\times$ static clearance, consistent with the criteria applied in subsection 4.6.2 and provided by ArianeSpace [3].

As recorded in Table 6.1, all configurations across both assessed launch phases comfortably meet this requirement with substantial margins.

The center-of-mass is assessed individually, as all four configurations are well within the limits imposed by ArianeSpace [3], as recorded in Table 2.2 and defined by Equation 5.4. Additionally, the CoM has a clear influence on the global displacement, which can be seen when adding the full panel coverage. Increasing the structural mass from 655.08 kg to 1009 kg and shifting the CoM from 2.842 m to 3.638 m results in a tip displacement of 33.48 mm instead of 26.87 mm. Only applying half of the solar panels introduces the benefits of panel shear stiffening, while limiting the negative effect of added mass. Compared to the bare configuration, adding half panel coverage decreases the tip deflection from 26.87 to 21.15 mm.

The multi-octagon bare configuration displays the lowest tip displacement due to the overall increased global stiffness and rigidity.

6.1.3. Linear Buckling Stability

Linear critical buckling analyses are executed to evaluate structural stability against axial compression and bending. Consistent with the design requirement implemented in subsection 4.6.2, the critical buckling factors must be at least CBF $\geqslant 2.0$ under the applied loading conditions. The resulting factors highlight a fundamental distinction between the bare and panel-covered structures.

- **Single-Octagon & Multi-Octagon (Bare) –** both demonstrate exceptional global stability. The single-octagon bare structure yields a minimum CBF of 9.64, which is further improved by the multi-octagon structure with a minimum CBF of 11.17. As can be seen in Figure 6.1 (pink boxes), the primary buckling mode is local to one of the weakest beams in the structure, either the cross-volume structure, or one of the thin-walled diagonal beams.
- **Single-Octagon Panel-Covered Configurations –** introduce a drastic reduction in linear buckling factors far below the acceptance criteria. As shown in Figure 6.1a (pink annotated box), the linear buckling factor belongs to local buckling of the solar panel. The FEA solver in COMSOL Multiphysics discovers many localized low-stiffness skin buckling within the solar panels before actually finding global structural buckling. As the scope of this study does not include solar panel design, these failing buckling modes are accepted at this stage, knowing that the structural buckling is within requirements.

6.2. Eigenfrequency Analysis

The dynamic stiffness of the spacecraft structure was evaluated through eigenfrequency analyses. To prevent destructive dynamic coupling with the launch vehicle during ascent, ArianeSpace imposes strict minimum frequency constraints for both the lateral (HR-002) and longitudinal modes (HR-003), as discussed in Table 5.1 and Table 2.2.

The resulting fundamental frequencies for each configuration are summarized in Table 6.1 and the performance margins relative to design thresholds are visualized in Figure 6.2.

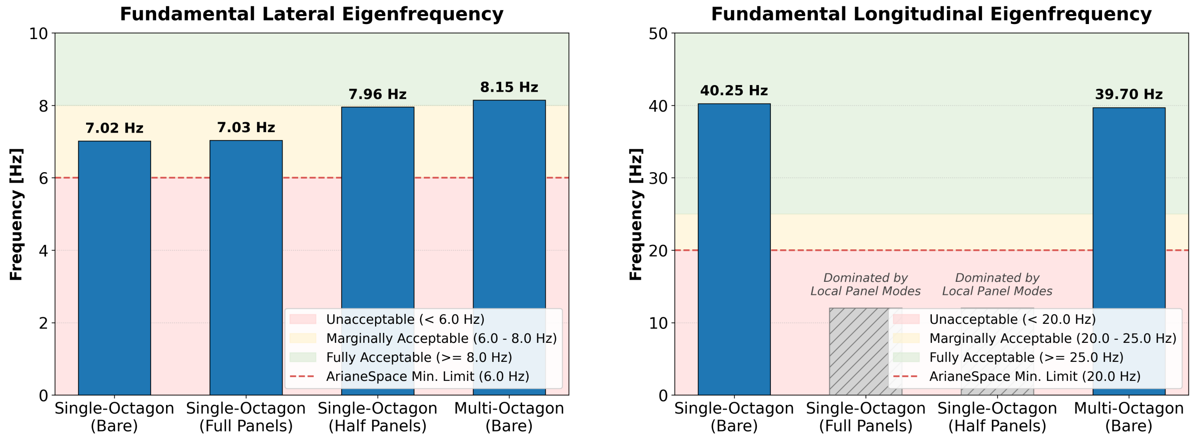

(a) Comparison between the obtained fundamental lateral eigenfrequencies.

(b) Comparison between the obtained fundamental longitudinal eigenfrequencies.

Figure 6.2: Comparison of the primary lateral and longitudinal eigenfrequencies for the four structural configurations. Background colouring indicates the requirement domains defined in subsection 4.6.2.

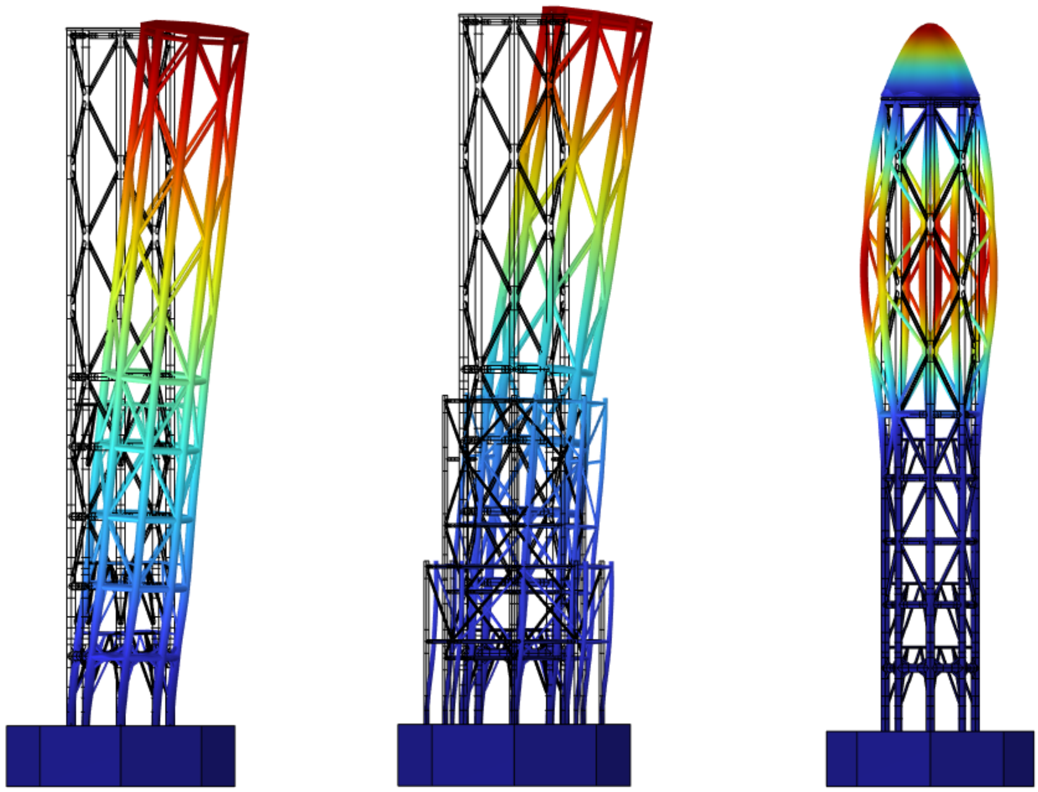

(a) Primary lateral frequency mode shape of single-octagon configuration. (7.0189 Hz)

(b) Primary lateral frequency mode shape of multi-octagon configuration. (8.1478)

(c) Primary longitudinal mode shape of single-octagon configuration. (40.247 Hz)

Figure 6.3: Visualizations of the first primary lateral and longitudinal modes. Mode shapes of the single-octagon structures including solar panels exhibit the same behaviour and motion as the visualized bare structure mode shapes. Similarly, the longitudinal mode shape is the same for each structural configuration, as it is dominated by the lid design.

6.2.1. Lateral Dynamic Stiffness

The Ariane 6 launch manual dictates an absolute minimum lateral eigenfrequency of 6.0 Hz (ArianeSpace [3]). Based on the evaluation criteria established in subsection 4.6.2, frequencies between 6.0 and 7.0 Hz are considered marginally acceptable due to uncertainties pertaining future developments and mass growth. Frequencies of 8.0 Hz and higher are categorized as fully acceptable.

- **Single-Octagon Variations –** the bare single-octagon structure yields a fundamental lateral eigenfrequency of 7.02 Hz placing it at the lower boundary of the acceptable domain. The addition of solar panels introduces competing effects of added stiffness versus added mass. While the fully covered configuration maintains a nearly identical frequency (7.03 Hz), reducing the coverage to half-panels successfully raises the lateral eigenfrequency to a more acceptable value of 7.96 Hz.
- **Multi-Octagon Configuration –** the multi-octagon design exhibits the highest dynamic stiffness, achieving a fundamental lateral frequency of 8.15 Hz. The expanded geometric footprint and internal load paths of this configuration provide sufficient rigidity to comfortably position it in the fully acceptable design region.

The global structural lateral modes are illustrated in Figure 6.3.

6.2.2. Longitudinal Dynamic Stiffness

The minimum required longitudinal eigenfrequency for the launch environment, as dictated by ArianeSpace [3], is 20.0 Hz. Similar to the lateral criteria, the conceptual trade-off designated 20.0 – 25.0 Hz as marginally acceptable and anything above 25.0 Hz as fully acceptable.

As shown in Table 6.1, the primary longitudinal frequencies for the bare configurations are approximately 40 Hz, thus exceeding the requirement with substantial margins. However, it is important to note that the longitudinal frequency seems to be fully governed by the spacecraft lid, as can be seen in Figure 6.3c. Any changes to the lid design, which is unavoidable, are directly impacting the longitudinal eigenfrequency. A lot of margin at this stage can easily disappear once the lid will be designed in detail according to the chosen baseline distribution.

6.3. Sinusoidal Excitation Analysis

The sinusoidal excitation analysis is explained in subsection 5.2.2, where the input in lateral and longitudinal directions are shown in Figure 5.4. Several metrics have been identified and evaluated, including transmissibility and maximum stress. All evaluated metrics are summarized in Table 6.2 for the SO-BR and the MO-BR configuration.

It is important to note the slight discrepancy between the eigenfrequencies of the sinusoidal excitation analysis, and those listed in Table 6.1 as a result of the separate eigenfrequency analysis. Though the difference is minimal, it can be explained by the fact that the sinusoidal excitation analysis is a prestressed modal analysis, which includes the static launch accelerations before determining the eigenfrequencies.

The dynamic transmissibility, Q, is the ratio between output and input acceleration and can be interpreted as either an amplifier $(Q > 1)$ or as a dampener $(Q < 1)$. The dynamic transmissibility can be determined as follows:

$$Q(f) = \left| \frac{a_{\text{output}}(f)}{a_{\text{input}}(f)} \right| \tag{6.1}$$

The lateral and longitudinal sinusoidal excitations are evaluated individually to match the common practice of experimentally testing them individually as well during vibration test campaigns.

As can be seen in Table 6.2, the lateral excitation results in a significant peak acceleration of 13.5g at a transmissibility of 16.72 for the single-octagon structure. The peak acceleration (and transmissibility) occurs, as expected, at the primary lateral eigenfrequency, as can be seen in Figure 6.4a. The significant acceleration results in significant stress in the structure, causing a negative MoS and thus potentially resulting in failure of the structure. On the contrary, for the multi-octagon structure, the peak acceleration and transmissibility are even further increased, but do not result in a negative MoS, thus no structural failure is expected. This indicates that the multi-octagon structure is better able to transfer the loads coming from the acceleration to avoid stress concentrations.

As depicted in Figure 6.4b, the lateral transmissibility is significantly less for the nodal location roughly halfway the axial distance of the structure. As expected, the peak amplitudes occur at the tip of the spacecraft, with accelerations anywhere lower on the structure significantly less.

Table 6.2: Summary of dynamic response metrics under Ariane 6 sinusoidal launch excitations (2 – 100 Hz), applied to the bare configurations SO-BR and MO-BR. All lateral assessments have been based on the sinusoidal base excitation in x-direction. All longitudinal assessments have been based on the sinusoidal base excitation in z-direction.

Metric	Unit	Axis / Plane	Single-Octagon Bare	Multi-Octagon Bare
Fundamental resonance	Hz	Lateral (X/Y)	7.00	8.13
Peak output acceleration	g	Lateral (X/Y)	13.50	20.40
Dynamic transmissibility (Q_x)	–	Lateral (X/Y)	16.72	25.50
Maximum displacement	mm	Lateral (X/Y)	68.42	77.70
Max. von Mises stress	MPa	Lateral (X/Y)	269.95	244.40
Margin of safety *	–	Lateral (X/Y)	-0.059	0.039
Fundamental resonance	Hz	Longitudinal (Z)	37.51	38.09
Peak output acceleration	g	Longitudinal (Z)	73.09	78.13
Dynamic transmissibility (Q_z)	–	Longitudinal (Z)	73.09	78.13
Maximum displacement	mm	Longitudinal (Z)	12.84	13.35
Max. von Mises stress	MPa	Longitudinal (Z)	1311.80	780.82
Margin of safety **	–	Longitudinal (Z)	-0.654	-0.418

* MoS is determined based on the CFRP design limits, $\sigma_t = 533.8$ MPa & $\sigma_c = 254.0$ MPa
** MoS is determined based on Al-7075-T6 limits, $\sigma_t = 454.5$ MPa & $\sigma_c = 454.5$ MPa

Figure 6.4c depicts the transmissibility of the longitudinal sinusoidal excitation, corresponding to the peak values summarized in Table 6.2. The longitudinal response is almost entirely dominated by the spacecraft lid design. The spacecraft lid is outside of the scope of this study and thus should the resulting response be treated with caution. The unacceptable MoS does not indicate a failure of the structure itself, but rather a failure of the spacecraft lid and highlights the importance of including a detailed lid design. Due to the dominance of the lid on the longitudinal response, the response shall be highly influenced by any design choices on lid material, geometry, thicknesses, and design details.

The maximum stress and displacement during lateral excitation can be seen in Figure 6.4d, indicating a too high stress for the single-octagon structure, with an acceptable stress level for the multi-octagon structure. It can be seen that the primary mode, as expected, is the bottleneck, with any secondary modes resulting in significantly lower stress levels. Overall, the maximum displacement is not an issue in any of the evaluated cases, as the maximum design limit of static fairing displacement has been set at 125 mm, as discussed in subsection 4.6.2 and Appendix I.

The maximum displacement and stress concentrations due to longitudinal excitation, Figure 6.4e, indicate the extreme stress levels occurring the in the spacecraft lid design. As the design is not final, the actual values do not carry a lot of weight, but rather prove the need for a detailed design of the spacecraft lid.

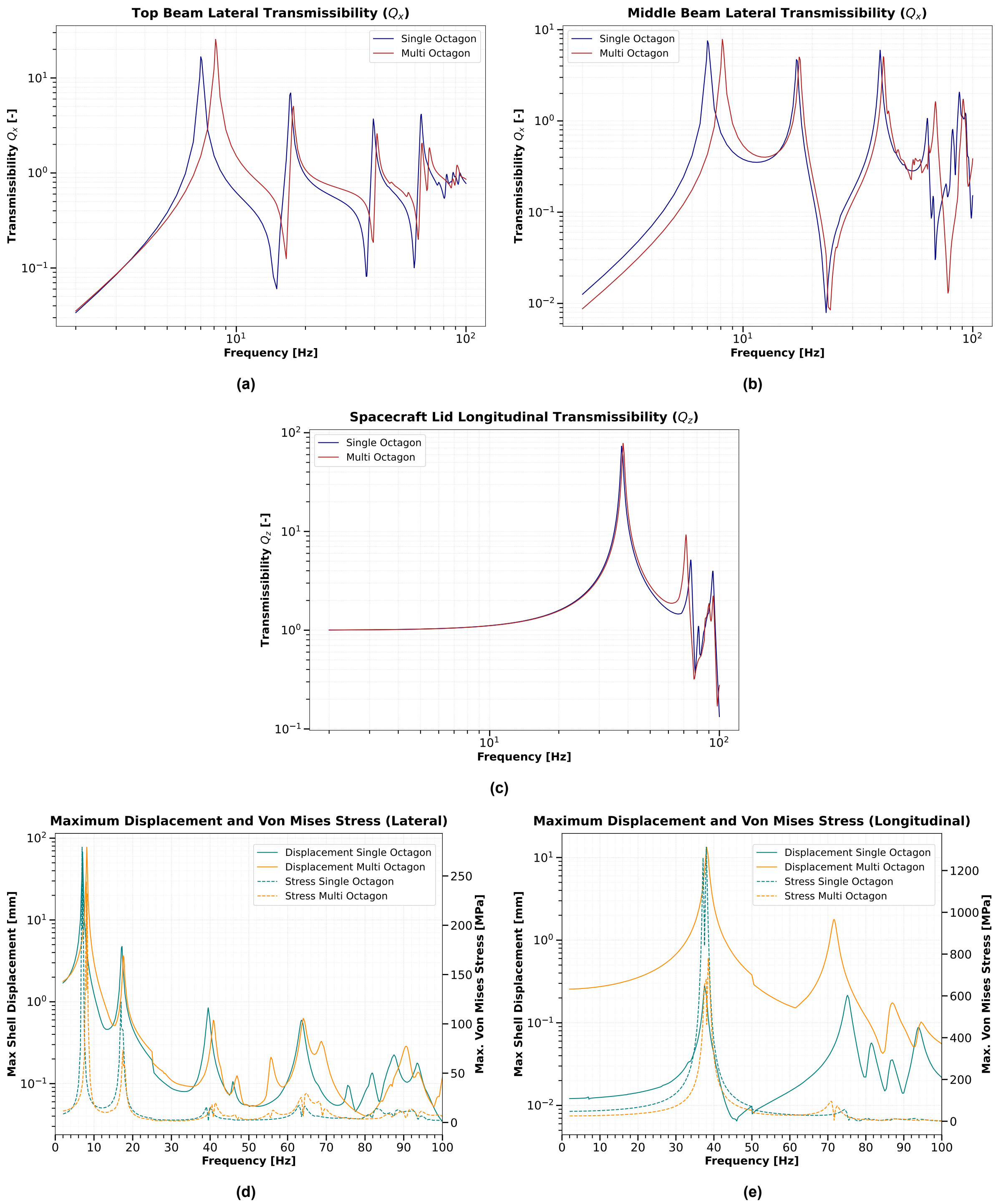

Figure 6.4: a) Lateral transmissibility at z = 16.15 m. **b)** Lateral transmissibility at z = 8.55 m. **c)** Longitudinal transmissibility at spacecraft lid (x, y, z) = (0, 0, 16.3 m). **d)** Maximum displacement and stress within spacecraft structure due to lateral excitation. **e)** Maximum displacement and stress within spacecraft structure due to longitudinal excitation.

6.4. Micrometeoroid Impact Analysis

The micrometeoroid impact analysis is discussed in subsection 5.2.3, and the choice is made to evaluate the impact of a micrometeoroid with a diameter of 0.01 cm, with an occurrence of once per m^2, per year.

The impact location is at the top of the spacecraft structure, directly on the bare CFRP structure, representing a worst case scenario. Figure 6.5 depicts the incoming direction and impact location, at a total height of 15.883 m above the global zero-height plane. The image also highlights some of the nodal points used in the assessment of lateral baseline deformations.

Besides local damage to heat shields, solar cells, structures, or any related consequences, the impact has three major effects on the structure that can be evaluated:

1. **Global tumbling motion –** which is the global tumbling of the entire spacecraft, assuming that the incident particle transfers 100% of its momentum to the spacecraft. As a result, the free-floating spacecraft will absorb the momentum and start rotating around its CoG.
2. **Stress-based wave propagation –** which is the propagation of stress waves throughout the structure as a result of the impact. From the direct impact location, the stress will propagate in all possible directions, causing potential stress concentrations and visualizing the load paths the stress takes.
3. **Resonance deformations –** which are lateral deformations due to the introduced resonances and vibrations into the structure. These vibrations cause CFRP beams in octagonal shape to globally squeeze and relax, resulting in a distance change between two diagonal points on the structure.

A quick verification can be made to check whether the wave propagation throughout the structure behaves as expected. Based on the COMSOL output, as provided in Table 6.3, the traversal time of the stress propagation between two vertically separated points (12.1 m separation) can lead to the wave propagation velocity. These values can be compared against the theoretical value of the wave velocity in a 1D rod as follows:

$$v_{wave} = \sqrt{\frac{E}{\rho}} = \sqrt{\frac{81.2 \times 10^9 \text{ (Pa)}}{1526 \text{ (kg/m}^2\text{)}}} \approx 7294.59 \text{ m/s} \tag{6.2}$$

As can be seen from the wave velocities in Table 6.3, the velocities match the theoretical value exceptionally well, boosting confidence in the analysis of wave propagation and its resulting distance deformations.

For the analyses on stress propagation, as well as the distance distortions, several nodal locations have to be identified. The assessed nodal locations are visualized in Figure 6.5. The "T" indication refers to the top of the spacecraft, where the nodes are located on the CFRP structure at a height of 15.883 m. The "B" indication refers to the bottom of the spacecraft, where the nodes are located on the CFRP structure at a height of 4.05 m. The referenced "-X", "+X", "-Y", and "+Y" refer to nodes on the CFRP structure at a height of 16.15 m and respective to each side of the spacecraft.

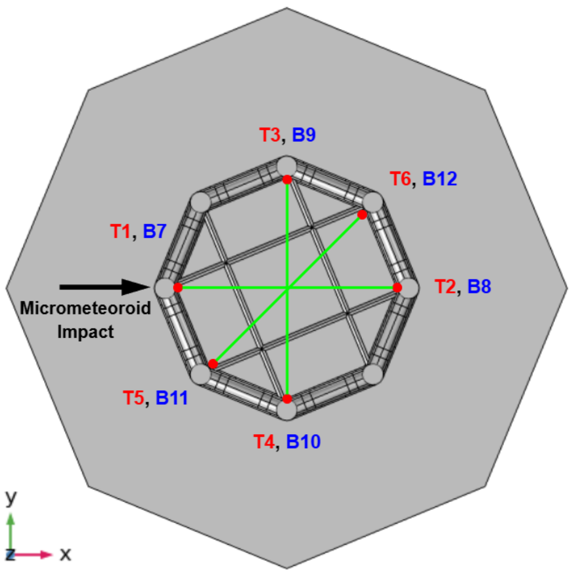

Figure 6.5: Visualization of nodal locations during the assessment of lateral baseline direction deformations due to micrometeoroid impact. "T" references to the top location at a height of 15.883 m and "B" refers to the bottom location at a height of 4.05 m.

Table 6.3: Summary of micrometeoroid impact response metrics, wave propagation velocities, peak stress, and distance distortion across structural configurations.

Metric	Unit	Single-Octagon Bare		Single-Octagon Full Panels		Multi-Octagon Bare	
		Value	Time	Value	Time	Value	Time
Maximum stress on impact	MPa	36.53	100 ns	34.26	100 ns	125.67	100 ns
Global tumbling angle	μrad	0.4152	5 s	0.2902	5 s	0.3997	5 s
Stress-wave propagation velocity	m/s	7562.50	–	7249.85	–	7469.14	–
Theoretical 1D wave velocity	m/s	7294.59	–	7294.59	–	7294.59	–
Peak stress Top (0.2–2.0 ms)	Pa	4199.3	1.52 ms	470.7	0.30 ms	1871.0	0.59 ms
Peak distance distortion Top (0.2–2.0 ms)	nm	3.90	1.51 ms	3.15	0.74 ms	7.31	1.53 ms
Peak stress Bottom (0.2–2.0 ms)	Pa	0.6930	2.00 ms	0.2060	1.96 ms	0.5566	2.00 ms
Peak distance distortion Bottom (0.2–2.0 ms)	pm	1.06	2.00 ms	0.33	2.00 ms	0.19	1.82 ms
Peak stress Top (50–80 ms)	Pa	0.0012	74.2 ms	0.0109	80.0 ms	0.0166	55.2 ms
Peak distance distortion Top (50–80 ms)	pm	1.06	72.8 ms	0.55	52.2 ms	1.06	64.4 ms
Peak stress Bottom (50–80 ms)	Pa	0.3537	76.0 ms	0.1422	68.2 ms	0.3074	80.0 ms
Peak distance distortion Bottom (50–80 ms)	pm	4.33	80.0 ms	1.29	77.2 ms	9.51	64.2 ms

Global Tumbling Motion

The global tumbling motion of the spacecraft as a result of a micrometeoroid impact has significant implications for instrument pointing stability and the potential need of active AOCS systems to counteract the tumbling. Because the impact analysis in COMSOL uses a linear elastic approach, no geometric nonlinearity is taken into account, thus global rigid-body rotation cannot be directly extracted from the output data.

Because the impact duration (5 ns) can be considered instantaneous compared to the response time, the event can be approximated as an ideal angular impulse acting on the free-floating spacecraft. The position of the CoG and the impact location can be expressed as position vectors $\mathbf{r}_{\text{CoG}} = [0, 0, \text{Z}_{CoG}]^{\text{T}}$ m and $\mathbf{r}_{\text{Impact}} = [-1.157, 0, 15.883]^{\text{T}}$ m.

Consequently, the cross product with the force vector $\mathbf{F}(t) = [F_x(t), 0, 0]^{\text{T}}$ results in the instant torque vector $\boldsymbol{\tau}(t)$:

$$\boldsymbol{\tau}(t) = \Delta\mathbf{r} \times \mathbf{F}(t) = \begin{bmatrix} 0 \\ \Delta Z \cdot F_x(t) \\ 0 \end{bmatrix} \tag{6.3}$$

The force is aligned with the x-axis in the positive direction, meaning that the x-offset of the impact location does not result in any torque and the only introduced torque is about the y-axis (τ_y). Integrating the torque over the impact duration of 5 ns, the total angular momentum can be obtained. Assuming a zero initial velocity and a free-floating spacecraft, the angular velocity due to impact can be calculated:

$$\omega_y = \frac{\Delta Z \cdot J}{I_{yy}} \tag{6.4}$$

where ΔZ is the z-distance between the CoG and the impact location, J is the impulse as defined in subsection 5.2.3, and I_{yy} is the second moment of mass. Multiplying with time results in the global tumbling angle:

$$\theta(t) = \left(\frac{\Delta Z \cdot I}{I_{yy}}\right) t \tag{6.5}$$

The resulting global tumbling angles of the three different configurations can be seen in Figure 6.6.

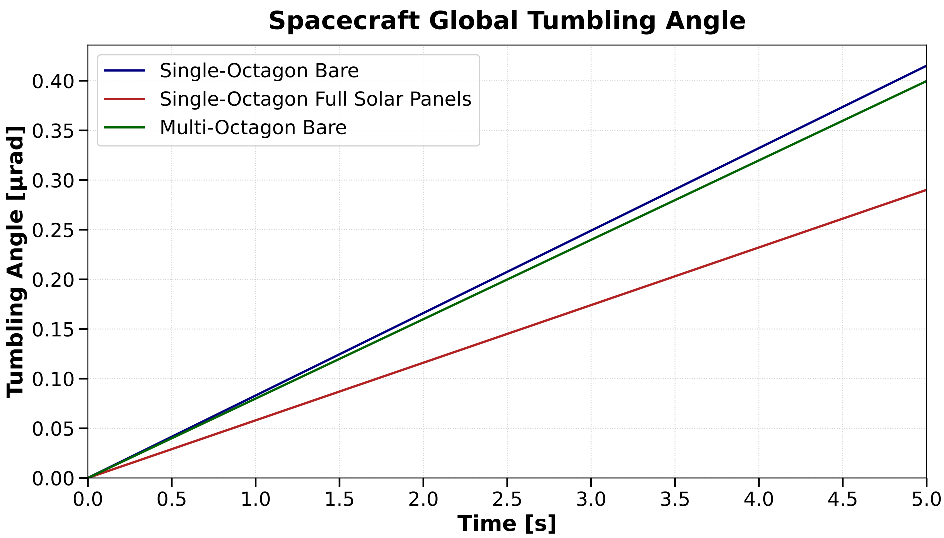

Figure 6.6: Analytically determined global tumbling angle for the three spacecraft structures.

The pointing precision needed for scientific observations depends on the aimed for wavelength (energy level) and the baseline it is observed with. The FOV for each baseline and energy combination can be determined by:

$$\text{FOV} = \frac{\lambda}{D} \cdot \frac{E}{\Delta E} \tag{6.6}$$

where λ is the wavelength (m), D the baseline (m), E the energy level (eV), and ΔE the energy resolution. For the XRIstel energy range of 1 – 7 keV and the baseline range of 0.01 – 1.0 m, the most stringent FOV precision is 10.5 nrad for the energy 7 keV and baseline of 1 m. The most relaxed FOV precision required is for the baseline of 0.01 m at 7 keV, with a precision required of 1.05 μrad.

As a result, the evaluated impact causes the spacecraft to almost instantaneously go outside the FOV of the 1 m baseline, while still within range of smaller baselines with corresponding energy levels. The global tumbling angle and deformation should thus be compensated by the AOCS system. While the preference would be to act as quickly as possible, the scientific loss of several tenths of seconds is fairly acceptable, giving the metrology system, onboard computers, and active AOCS system some time to react.

The assessed impact would not cause immediate danger for the global spacecraft pointing, as the coarse pointing systems such as star trackers have a FOV of 58 mrad, simultaneously highlighting the urgent need to act well before the spacecraft goes beyond coarse alignment FOVs.

Stress-Based Wave Propagation

Due to the impact, stress waves propagate from the location of impact throughout the structure in all possible directions, highlighting the load paths available to the waves. Four nodal locations have been selected at the top of the spacecraft at the -X, +X, -Y, and +Y locations at a height of 16.15 m and located on the outer most locations of the CFRP structure. This means that the -X nodal locations is near the impact zone at only 26.7 cm distance.

The global maximum stress levels occur near the moment of impact and at the location of impact. As can be seen in Table 6.3, the maximum stress levels vary across the structures. The maximum stress during impact on the single-octagon structures remains near 34 – 36 MPa, well below the design limits of the chosen CFRP. The stress level of the multi-octagon structure increases significantly to a maximum of 125.67 MPa, which can be explained by the much thinner CFRP wall thickness at the impact location. All evaluated stress levels are well below the design limits.

As can be seen from Figure 6.7e and Figure 6.7f, the stress concentrations differ significantly based on their lateral location around the structure, with the -X location clearly experiencing higher stresses. While the -X location near the impact zone reached above 4000 Pa, the other lateral locations seem to reach maxima of slightly above 700 Pa.

As of now, the peaks near 1.50 ms cannot be fully isolated and explained, but the observation can be made that these peaks are only present in the SO-BR and the MO-BR configurations (Figure P.2e and Figure P.2f), suggesting that the solar panels significantly influence the stress propagation. These stress peaks correspond with lateral deformation peaks as depicted in Figure 6.7a and Figure P.2a. The response of the SO-FP configuration can be seen in Figure P.1a, Figure P.1e, and Figure P.1f.

Although it cannot be determined with certainty, the suspicion involves a coming together of propagated waves, possibly constructively interfering with each other. The initial peak near 0.4 ms can be explained by the arrival of the stress wave at T2, with the wave having to travel halfway around the octagon (≈ 3.572 m, with a wave velocity of 7562.5 m/s). The peaks that start at around 1.4 ms seem to coincide with the time the wave requires to travel 1.5 times around the octagon, arriving once again at T2 at 1.417 ms. Additionally, the reflected stress waves by the spacecraft lid and/or the propagated waves through the lid could also play a role. To fully understand the occurring pattern, the phenomena should be isolated and investigated more rigorously, which has not been possible thus far due to time constraints.

As can be seen from Table 6.3, the stress also quickly dissipates, with the peak stress concentrations at the top nodal locations near 4199.3 Pa at 1.52 ms and only 0.0012 Pa at 74.2 ms for the single-octagon bare structure, which is a reduction of 100%. Similar reductions are the case for the SO-FP and the MO-BR structures over similar timespans.

Resonance Deformations

The lateral distance distortions between nodal pairs as shown in Figure 6.5, can be evaluated as well within the time windows of 0.2 – 2.0 ms and 50 – 80 ms. As can be seen in Figure 6.7a, the peak lateral distortion occurs between nodal pair T1-T2, as expected, because they are in line with the impact direction. These deformations can cause invalid or distorted observations results in the case such an impact occurs during fringe finding. The absolute peak deformation of the SO-BR configuration is 3.90 nm (HR-005), which is significantly more than the required maximum of 0.1 nm distance change in baseline direction during operation. These lateral distance deformations also quickly dissipate, just like the stress waves, and are therefore considered a hindrance but not critical. Therefore it would be important to identify, register, and flag these impacts while processing the data for the data end-user to decide whether to discard or keep the data right after impact.

The maximum occurring lateral baseline deformations for the SO-FP and the MO-BR are respectively 3.15 and 7.31 nm. Comparing Figure P.1a against Figure 6.7a and Figure P.2a again highlights the lacking peaks near 1.51 ms in the configuration containing the solar panels, suggesting that the solar panels absorb some of the suspected wave propagation and avoid the stress and deformation peaks around 1.5 ms.

Assessing the lateral deformations in the top nodal pairs during the 50 – 80 ms time window, it can be seen that the lateral deformations dissipated significantly, with only amplitudes of with maxima of 1.06 pm instead of several nanometers. These plots, Figure 6.7b, Figure P.1b, and Figure P.2b consistently show deformations on the picometer scale, with SO-FP once again showing less deformations, possibly due to the solar panels absorbing stresses early on.

The lateral distance deformations can also be assessed between the bottom nodal pairs, which are illustrated in Figure 6.7c and Figure 6.7d, with similar plots for SO-FP and MO-BR in Figure P.1 and Figure P.2. They clearly show the delayed response in the 0.2 – 2.0 ms window, which provide together with the stress plots the baseline for determination of the wave propagation and the wave velocity, translating into delayed response. In the 50 – 80 ms time window, it can be observed that the lateral deformations at the bottom nodal pairs are still very little, but larger than at the top nodal pairs in the same time window. This can be explained by the delayed response, whereas the top of the structure has already dampened out over time, the bottom of the structure is still experiencing relatively higher stresses and deformations.

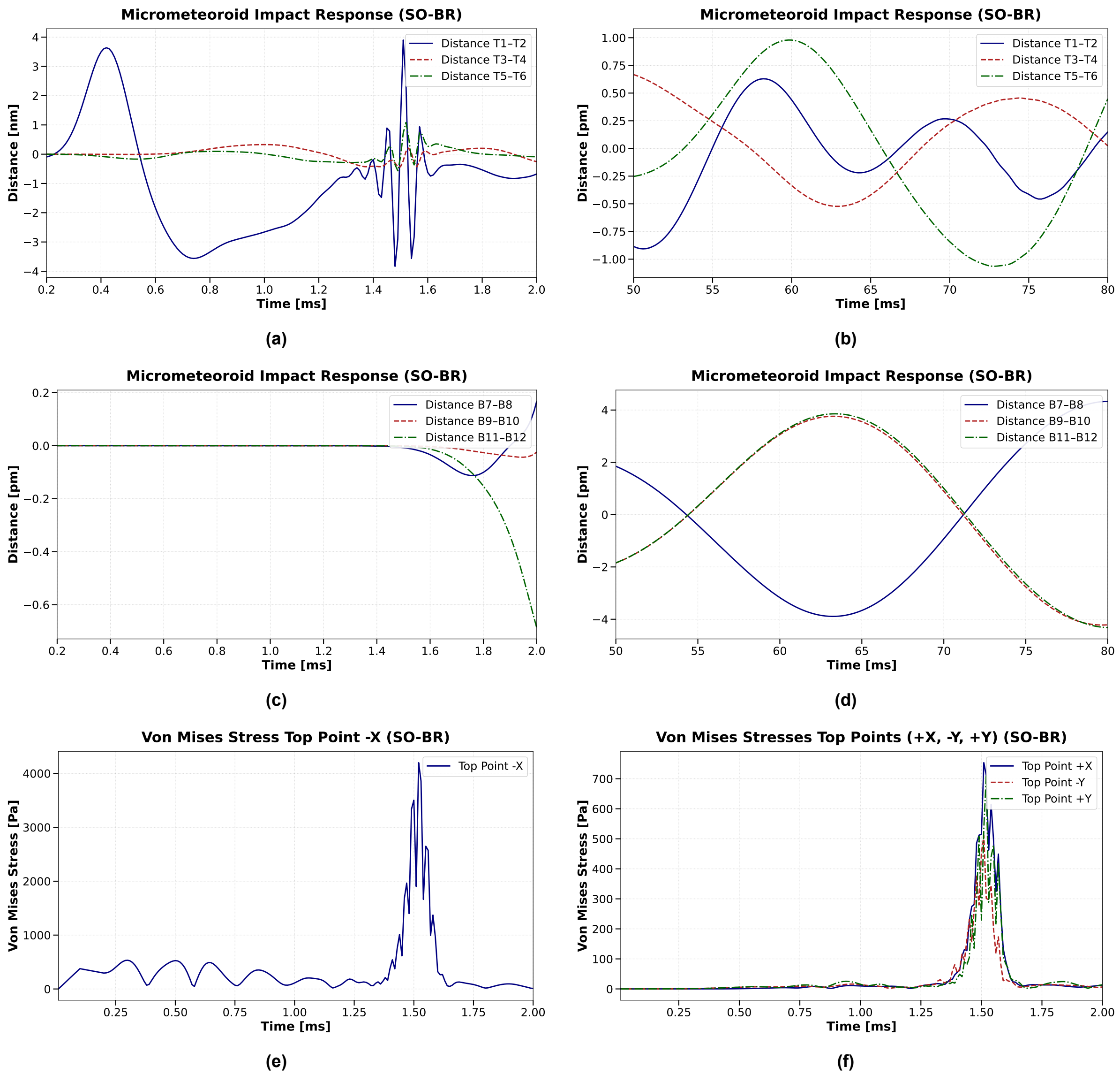

Figure 6.7: **a)** Response during time interval 0.2 –2.0 ms of lateral distances between three node pairs at the tip of the spacecraft. **b)** Response during time interval 50 – 80 ms of lateral distances between three node pairs at the tip of the spacecraft. **c)** Response during time interval 0.2 – 2.0 ms of lateral distances between three node pairs at the lower region of the spacecraft. **d)** Response during time interval 50 – 80 ms of lateral distances between three node pairs at the lower region of the spacecraft. **e)** Response during time interval 0.2 – 2.0 ms of von Mises stress at nodal location -X at the tip of the spacecraft. **f)** Response during time interval 50 – 80 ms of von Mises stress at nodal location +X, -Y, and +Y at the tip of the spacecraft.

6.5. Thermal Analysis (Fairing Separation)

Following fairing jettisoning during the Ariane 6 launch profile (t = 190s), the spacecraft is exposed to two different heat inputs: aerothermal drag and direct solar radiation. The aerothermal drag function has been provided by ArianeSpace [3] and is shown in Figure 5.3. The aerothermal flux has been applied to all surfaces perpendicular to the flight direction, thus experiencing drag, while the direct solar radiation has been applied in the positive x-direction, perpendicular to any surface in its path. The total transient thermal analysis spans from the moment the fairing is jettisoned (t = 190s) to an arbitrary t = 2180s. This time domain encapsulates the entire aerothermal drag profile, with an additional 13 minutes to depict the trend after aerothermal drag is removed as input.

The critical spacecraft structure and its instruments are protected by a coverage of MLI and solar panels, as further discussed in subsection 5.5.4. The temperature profiles of several locations can be evaluated to assess the impact of the dual-source heating on the spacecraft. The temperature profile of several nodal locations and maxima across solar panels / lid surfaces can be seen in Figure 6.8.

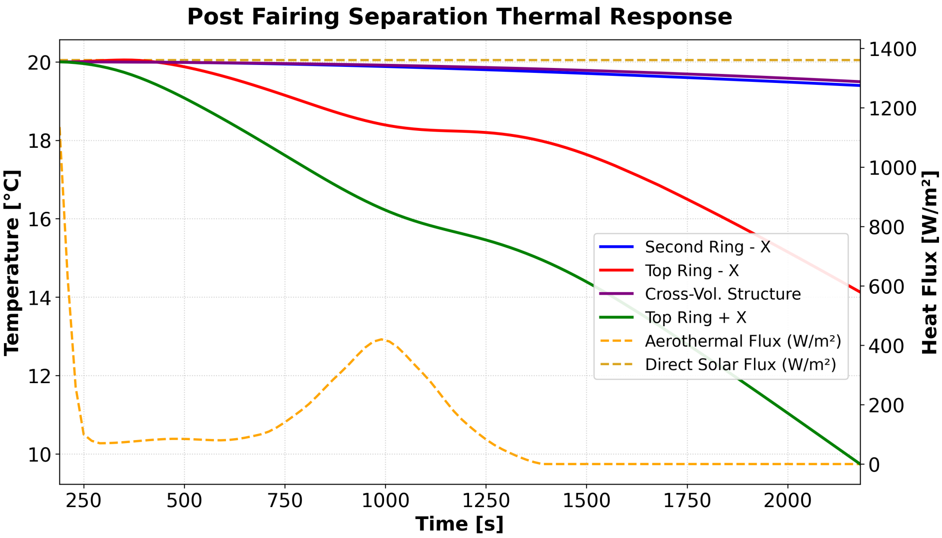

(a) Temperature profiles after fairing separation at specific nodes. The "- X" assignment indicates the node is on the sun-facing side of the spacecraft, while "+ X" is located on the shadow side of the spacecraft. The purple has been evaluated in the middle of the lowest cross-volume structure.

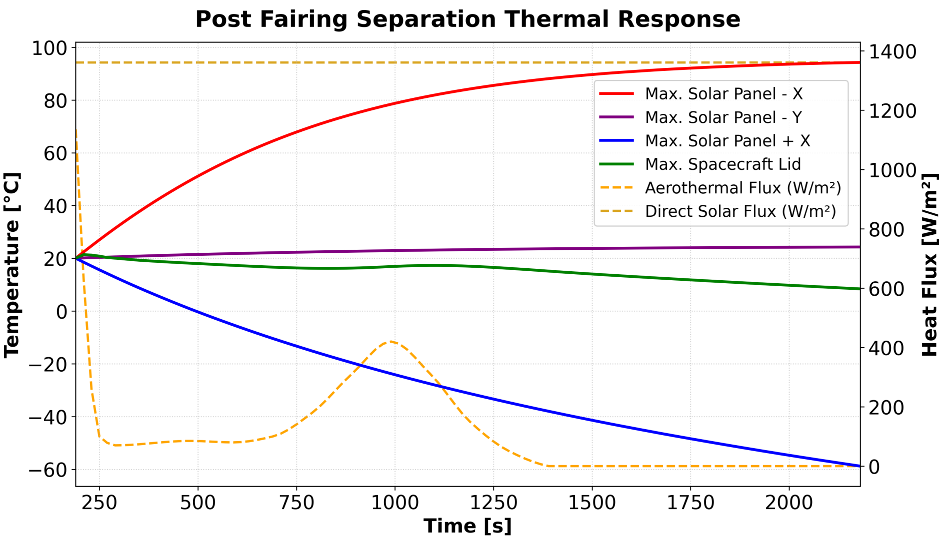

(b) Temperature profiles after fairing separation at collections of surfaces. Red, purple, and blue have been assessed as maximum temperatures across 20 solar panels, with "- X" in sun-facing direction, "- Y" parallel to the solar flux direction, and "+ X" shaded. Green represent the maximum temperature across the surfaces of the SC lid.

Figure 6.8: Thermal Response at different locations after fairing separation.

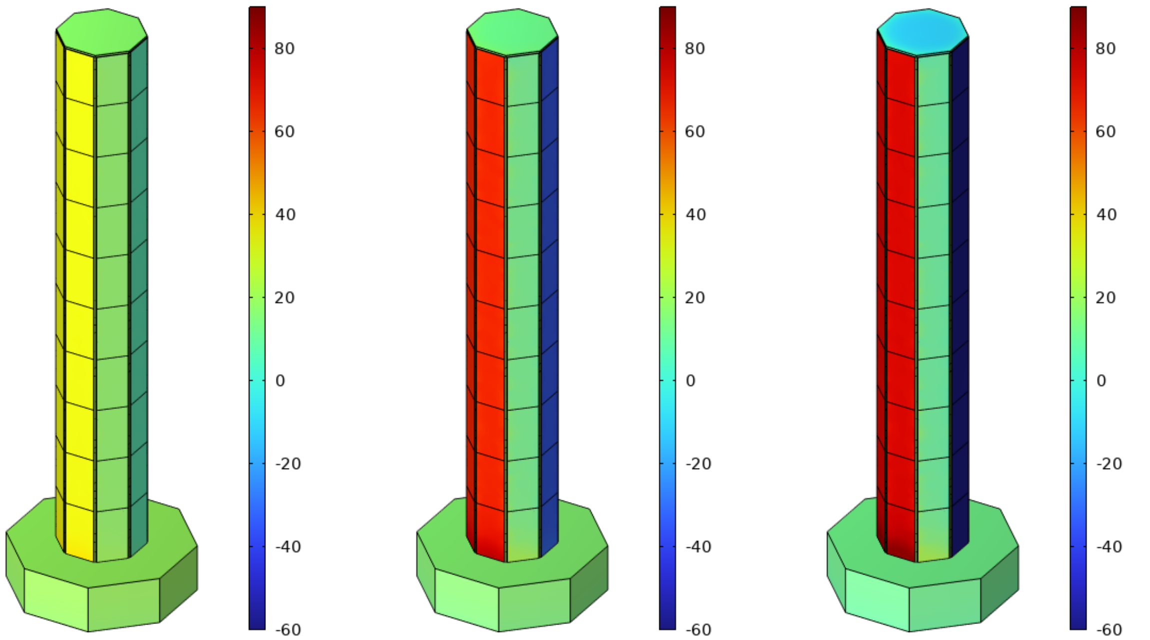

(a) Temperature Profile at t = 370 s.

(b) Temperature Profile at t = 1170 s.

(c) Temperature Profile at t = 2180 s.

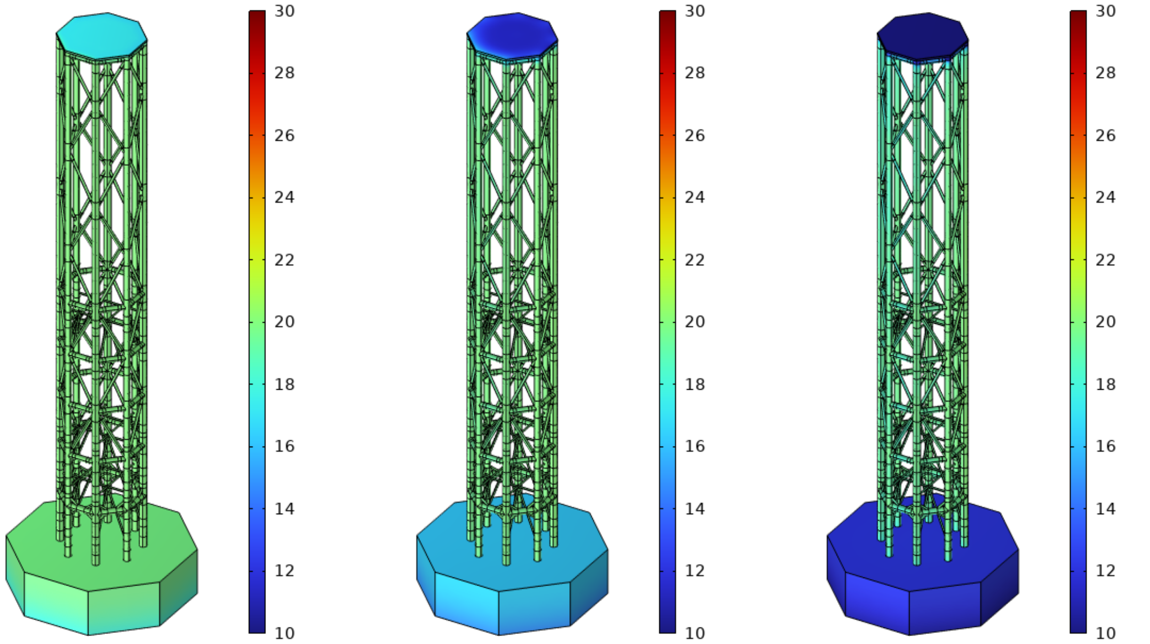

(d) Temperature Profile Structure at t = 370

(e) Temperature Profile Structure at t = 1170

(f) Temperature Profile Structure at t = 2180

Figure 6.9: Surface/nodal temperature profiles at three different timestamps and multiple locations on outer and inner surfaces.

The transient response shows very distinct thermal behaviours governed by surface radiative properties, component thermal mass, and its assessed locations.

The surfaces exposed to direct heat fluxes show expected behaviour, with Figure 6.8b clearly illustrating a significant increase in temperature on the sun-facing solar panels. As the solar flux is received on the same surfaces across the roughly 36 minute transient period, the solar panels keep increasing in temperature, reaching a temperature of almost 100 °C, after which the curve seems to flatten out. The shadow-facing solar panels show a significant cooling, as there is no thermal load applied to these surfaces, reaching temperatures of -60 °C after half an hour. The solar panels that are exactly parallel to the incoming solar flux ("- Y") seem to maintain their temperature quite well, with a very minimal increase. This means that the solar panels radiate as much outwards as it received, with a slightly higher radiative input on the solar panels near the SC bus, as can be seen in Figure 6.9.

The temperature of the receiving spacecraft lid seems to increase a tiny bit, but only in the first roughly 40 seconds. This can be explained by the fact that this surface sees a variable flux that does not match the significance of the direct solar flux. Additionally, the aluminium lid can transport the heat much faster and more efficiently away throughout the aluminium structure towards the CFRP structure. For the remainder of the assessed time response, the spacecraft lid cools down very gradually.

Based on the first-order approximations in Appendix O, it can be seen that almost no heat is transported through the MLI, and only 0.05% of the direct solar heat flux comes through. This can also be seen in the resulting cool-down of internal node locations on the CFRP structure. As Figure 6.8a shows, each nodal CFRP location cools down, with nodes close to the spacecraft lid clearly showing the effects of the aerothermal flux. This can be explained by the decrease in temperature of the SC lid after its initial input, acting as a heat sink for nearby CFRP structures. Nodal locations deeper in the spacecraft structure cool down as well, but much less rapidly, as all nearby structures cannot radiate towards a heat sink, but only towards each other.

Because the thermal environment during launch is only temporal, the induced thermal gradients do not necessarily affect operational capabilities of the spacecraft. The more critical aspect during the launch environment is to avoid permanent damage due to thermal gradients or peak temperatures. The thermal analysis provides insights in the cooling down of the spacecraft and thus whether it requires any active thermal control system to avoid unwanted behaviour.

As discussed in subsection 5.5.1 and depicted in Appendix L, the idea was to connect the CFRP structure to the aluminium bus and lid through an adhesive connection, using LOCTITE Stycast 2850 FT and CAT 9. This adhesive has a glass transition temperature of 86 °C and should thus be kept below this temperature, preferably with some margin. This means that it should be prevented that the temperature rises above, or that a different connection type / adhesive should be considered.

Similarly, too high temperatures on the solar panels should be avoided to mitigate the risks on permanently damaging solar panels or electrical infrastructure exposed to these temperatures. Thermal gradients should be controlled in such a way that no mechanical damage occurs beyond elastic behaviour of materials.

6.6. Verification of Requirements

This sections discusses the verification of several of the initial requirements formulated in section 2.4, and summarized in Table 2.2. The results, as obtained and discussed in chapter 6, allow for the binary assessment of several requirements (satisfied/not satisfied). Additionally, the results provide valuable insights into closely related metrics for other requirements, such as the first-order insights into the effects of micrometeoroid impacts, or the in-orbit thermal environment.

Launcher Constraints

The launcher constraints are imposed by ArianeSpace and dictated by the Ariane 6 launch manual, specifically for the Ariane 64 long fairing. The spacecraft length requirement (HR-011), the structural tip diameter (HR-012), and the spacecraft mass (HR-013) have all been satisfied in the current designs.

The satisfaction of these requirements/constraints are not a result of the analyses performed, but have been utilized as boundary conditions during the design process. The length and the diameter are hard constraints during the spacecraft structural design, whereas the spacecraft mass currently satisfies the constraint due to minimal knowledge on mass allocations. Throughout the future development of XRIstel, more (sub)systems will be added, and mass allocation and mass budgets will become more relevant, possibly requiring the mass budget for the structure to be adjusted. The summarized verification can be found in Table 6.4.

,

Table 6.4: Summary of requirement verification, where based on results obtained in chapter 6, the verification of the requirements in Table 2.2 are assessed.

Requirement	ID	Satisfied?	Remarks
Spacecraft length	HR-011	Yes	–
Spacecraft diameter	HR-012	Yes	–
Spacecraft mass	HR-013	Yes	Much mass will be added throughout mission development, mass allocation for structure is first-order approximation.
Launch survivability	HR-001	Partially	The SO-BR configuration satisfies partially, similar to SO-HP and SO-FP. The MO-BR satisfies fully.
Spacecraft CoG	HR-007	Yes	–
Lateral eigenfrequency	HR-002	Yes	–
Longitudinal eigenfrequency	HR-003	Yes	–
Spacecraft material (1)	HR-014	Yes	–
Spacecraft material (2)	HR-015	Partially	Partially satisfactory does not necessarily mean any issues. A too high RML is often considered acceptable if the CVCM is low enough.
Sinusoidal excitation	HR-009	Partially	Longitudinal (inherent to the lid design) excitation causes failure. SO-BR fails due to lateral excitation as well, with Mo-BR satisfying the requirement for lateral excitation.
Micrometeoroid impact	SR-002	Partially	The structural response to a micrometeoroid impact has been analysed and investigated, with global stress levels satisfactory and the global tumbling angle acceptable.
Mechanical stability	HR-005	No	The deformations during impact in lateral baseline direction become too high (> 0.1 nm), but only temporarily.

Launch Survivability

The major design requirement is the survivability of the launch environment (HR-001), which dictates that the spacecraft must be able to withstand launch accelerations, including the proper safety factors. According to ECSS standards, for the CFRP structure, a FoS of 2.0 has to be applied, resulting in the launch accelerations as defined in Table 4.1. The survivability of the launch environment can be determined by a set of metrics, which are discussed in section 6.1 and summarized in Table 6.1. The metrics upon which the survivability is assessed, are the induced stress, tip displacement, and critical buckling factor. Additionally, the thermal environment and temperature profiles of the structure after fairing separation provide insights into the thermal survivability during launch.

As summarized in Table 6.4, some of the assessed configurations satisfy the launch survivability constraint partially, while the only configuration that fully satisfies the requirement is MO-BR.

The SO-BR configuration satisfies all the launch survivability metrics regarding critical buckling factors and tip displacement with significant margins. The maximum induced stress prevents the configuration from completely satisfying the requirement, as the resulting MoS is negative. Local stress concentrations result in too much induced stress. Similarly, configuration SO-HP experiences the same issue, though the MoS is less negative. Additionally, both the SO-HP and SO-FP experience critical buckling factor issues, which are not inherent to the structure, but are rather a characteristic of the solar panels. Because solar panel design is outside of the scope of this study, these failing criteria have been accepted and deemed an insignificant issue.

The MO-BR configuration is the sole assessed configuration that satisfies the MoS, the critical buckling factor, and tip displacement, all with significant margins.

It can thus be stated that only one of the configurations fully satisfies this major requirement, while the other configurations partially satisfy. The metrics that are not yet sufficient in the "failing" configurations are relatively of minimal impact, with the local stress concentrations relatively easily resolved by implementing local solutions. Similarly, the solar panel buckling can be relatively easily resolved with proper solar panel design and adequate integration onto the spacecraft.

Center of Gravity

The spacecraft CoG requirement is a fixed requirement/constraint imposed by the launch vehicle. It is thus also not a result of simulations discussed in this chapter, but is rather a result of design choices made in chapter 5. As can be seen in Table 6.1, the z-coordinate of the center-of-mass for each configuration lays well within the 1.166 – 4.230 m range. The requirement is thus satisfied with the current mass distribution and structure.

Eigenfrequencies

Eigenfrequency requirements are imposed by the launch vehicle provider, ArianeSpace, and dictate a minimum lateral eigenfrequency of 6 Hz (HR-002) and a minimum longitudinal eigenfrequency of 20 Hz (HR-003). As implemented in the conceptual trade-off (subsection 4.6.2) and later discussed again in section 6.2, a distinction is made between marginally acceptable and fully acceptable eigenfrequencies.

As can be seen in Figure 6.2, regarding the lateral eigenfrequency, all configurations satisfy the requirement of minimum 6 Hz. The three single-octagon configurations satisfy the requirement, but are considered marginally satisfactory. The MO-BR configuration is with minimal margin considered fully acceptable and thus also satisfies the requirement.

Regarding the longitudinal eigenfrequency, both the SO-BR and MO-BR configurations are satisfactory, with the SO-HP and SO-FP not assessed. Due to the structural design, hollow tubes, and the global configuration, the longitudinal eigenfrequency is mainly dominated by the spacecraft lid design. As the spacecraft lid has been designed as a simplified component and the detailed design of this lid is considered outside of the scope of this study, the results should be accepted with some caution.

The mass and detailed design of the spacecraft lid will eventually determine the global longitudinal eigenfrequency when assessed the structure without any of the scientific assemblies. Hence, the resulting (satisfactory) eigenfrequency can rapidly change with design changes and should thus not be considered acceptable unconditionally.

Outgassing

The outgassing requirements (HR-014 and HR-015) are constraints on the available materials and are thus considered to be a critical part of the design choices in early development. A distinction can be made between the outgassing requirements for general spacecraft components and those that are located near optical elements such as mirrors, detectors, or other essential components that could be harmed by condensation.

As Table 4.6 shows, the M40J/PMT-F33 material has satisfactory properties to adhere to the HR-014 requirements, with a TML and CVCM respectively below 1% and 0.1%. To satisfy HR-015, the material should also have a RML which is less than 0.1% and a CVCM less than 0.01%. The latter it satisfies, but the RML criteria is not automatically acceptable.

M40J/PMT-F33 has a RML of $\leqslant 0.21$, which can be considered unsatisfactory. The actual RML value of this material is not known and is expected to be lower than above-mentioned value, as the TML can range between 0.066 and 0.21, the RML has to be lower than the TML. In the case the TML would be 0.1, the RML would as a result be lower and thus satisfy the requirement. Additionally, it is important to note that a too high RML can still lead to the proper space certification and can still be accepted in case the CVCM is considered low enough.

As a result of this ambiguity, it cannot with certainty be concluded whether the material satisfies the outgassing requirement near optical components (HR-015).

Sinusoidal Excitation

The Ariane 6 launch manual does not dictate any verifiable metric regarding the sinusoidal excitation. There are not aimed for values regarding peak accelerations, transmissibilities, or damping factors. The metric to be verified is the survivability of the sinusoidal excitations (HR-009), which can be expressed as the MoS, with a positive $0 <$ MoS < 0.3 considered marginally acceptable, and a MoS > 0.3 fully acceptable, as defined in subsection 4.6.2 and Appendix I.

Based on the results discussed in section 6.3, it can be seen that the longitudinal MoS does not satisfy the requirement in any assessed case. As discussed, this is not due to the structural design, bur rather due to the lack of a detailed lid design. The failing longitudinal MoS can thus be considered acceptable during this study. The lateral MoS of the single-octagon is unsatisfactory and thus not meet HR-009, but the multi-octagon MoS is considered marginally acceptable, thus satisfying HR-009.

Micrometeoroid Impact

No strict quantitative metrics or guidelines are attached to the response to micrometeoroid impacts on spacecraft structure according to mission's system requirements. The impact analysis is performed to gain insights into the behaviour, and to assess the global metrics such as stress levels that translate to a MoS, lateral displacement in baselines directions, and global tumbling. Based on the maximum occurring stress level as documented in Table 6.3, the stress levels are nowhere near the material design limits, making the stress levels insignificant for material integrity.

For the global tumbling angle, the response behaviour is investigated to gain insights in future AOCS budgets and to determine whether pointing stability is maintained during and after impact. Based on the baseline and energy dependent FOV for observations, as documented in section 6.4, the global tumbling causes the spacecraft to rotate well outside of the most stringent FOVs, while still within certain FOVs of the shorter baselines at high energies. These global tumbling angles are not disastrous, as long as the AOCS can react and compensate within an acceptable time-frame (0 – 100 s). It is important that the observation data during these types of events are flagged, isolated, and assessed with care by the end-user.

Regarding the lateral deformations in baseline direction, the deformations as documented in Table 6.3 go beyond the acceptable 0.1 nm allowable displacement. This does not mean that the structure is not sufficient, but rather shows that during direct impact on the CFRP structure, these displacements should be picked up by the RLGs or the optical bench metrology (OBM) to flag the data obtained while displacements are too high. The data end-user then has to decide whether to include or discard the data during this time frame.

6.7. Conclusion

Based on the evaluated analyses and their corresponding results, it can be concluded that a majority of the pre-defined requirements are satisfied either fully or partially. Only the mechanical stability requirement (HR-005) is consistently unsatisfactory across the configurations in the case of a micrometeoroid impact. It is important to note that these lateral deformations are only temporary and do not cause permanent issues. In line with the conclusions of the detailed design phase, the multi-octagon structure outperforms the single-octagon structure in many evaluations, including the available cross-sectional area, stress level during launch conditions, eigenfrequencies, the CoG location, the total mass, and the sinusoidal excitation response. The MO-BR configuration is the only assessed configuration that fully satisfies the launch survivability requirement (HR-001). The results also show that the longitudinal eigenfrequency, and subsequently the longitudinal sinusoidal excitation response are dominated by the spacecraft lid design, which is currently included as a highly simplified design. Additionally, the highest stress concentrations are located at the interface between the main CFRP beams and the SC bus, modelled in a simplified manner. Both these cases highlight the need for detailed design of the spacecraft lid, as well as the connective joints between the CFRP and the SC bus. The micrometeoroid impact analyses show that the induced stress remain well within the material design limits across all configurations. The lateral deformations exceed the allowable 0.1 nm mechanical stability significantly, but only temporarily, with only several picometer displacements left after 50 ms. The micrometeoroid impact also causes the spacecraft to globally rotate, causing the spacecraft almost instantly to exceed the FOV of many of the baselines, including the most stringent baseline of 1.0 m with a FOV of 10.5 nrad. As a result, the AOCS should counteract the global rotation. Both the global rotation and the lateral deformations require flagging of the observed data, for the end-user to decide on its relevance. The Thermal analysis after fairing separation shows that the MLI is very effective at blocking direct solar radiation, while also identifying the originally proposes adhesive connection between the CFRP beams and the aluminium lid as an issue. During the assessed time frame after fairing separation, the critical CFRP beams near the spacecraft lid experience temperature above the glass transition temperature of the proposed adhesive. Based on the results of these first detailed design iterations, it can be concluded that the path to large ultra-stable structures for XRIstel is still within the possibilities, creating a baseline for future developments.

7 Conclusions

The purpose of this design study, as described in chapter 2, is to overcome the first step in the design and analysis of an ultra-stable spacecraft structure for the XRIstel mission. Based on the design and assessment of the simulation results, it can be concluded that several of the original study goals are achieved successfully, while others remain a challenge and form the basis for further development.

The literature review showcased that XRIstel's stringent combination of requirements has no direct heritage example, but that individual lessons can be drawn from heritage missions such as LISA and JWST. Both LISA and JWST demonstrated that CFRP offers promising properties and behaviour for ultra-stable structures, including sufficient outgassing performance. CFRP could be complemented by metallic materials such as Invar or ALLVAR Alloy 30 for critical optical bench components, or for joints and interfaces. The conceptual design phase continued on this literature review through a combination of analytical and numerical methods in search of conceptual designs. During the conceptual design phase, a conceptual design was obtained consisting of Toray M40J fibres in combination with PMT-F33 cyanate ester resin, including circular cross-sectional beams, and five additional support rings.

The detailed design phase identified the lateral eigenfrequency as the hardest launch-related requirement to satisfy. Ultimately, the single-octagon and the multi-octagon satisfied the requirement with 7.0 and 8.15 Hz respectively. A combination of lateral support rings and diagonal struts was identified as the most efficient manner to increase the lateral eigenfrequency, while minimizing structural mass. Additional support options such as increased diameter or increased wall thickness were deemed insufficient or impractical for many reasons. As for the two assessed mass distributions, the mechanical performance and expected thermal behaviour clearly favour the Configuration 1, which maintains all the camera planes at the SC bus instead of moving them higher into the structure.

Expanding the detailed design into an additional configuration, MO-BR, is a further improvement on the single-octagon structural design. During the evaluation of the load cases, response behaviour, and assessment against the requirements, the multi-octagon structure outperforms the single-octagon structure in almost every metric. The eigenfrequencies, the stress levels during launch, the lateral displacement during launch, the critical buckling factors, total mass, CoG location, and the sinusoidal excitation response are all more favourable for the multi-octagon structure. The multi-octagon satisfies nearly all assessed requirements as listed in Table 6.4, of which several with sufficient margins. The two main requirements that are not satisfies are the global tumbling as part of SR-002 and HR-005, due to the micrometeoroid impact as well. Both of these are temporary exceedances of the requirement limits, of which the global tumbling angle should be brought back within the 10.5 nrad FOV of the 1 m baseline by the AOCS, and the lateral deformations are passively dissipated within tens of milliseconds.

The results confirm the preliminary observation that the simplified lid design as implemented in this study, as well as the connection between the CFRP and the aluminium lid/bus are reason for major uncertainties. Both of these simplifications are outside of the scope of this study, but should be detailed further to allow for accurate modelling of the stress concentrations near the SC bus and the longitudinal response behaviour of the spacecraft lid.

The thermal analysis results after fairing separation confirm the effectiveness of MLI as heat shielding, while also showing that the proposed CFRP/aluminium connection using an epoxy-based adhesive might be problematic. After fairing separation, as currently modelled, the upper connection between the CFRP beams and the aluminium lid reaches the glass transition temperature of the proposed adhesive, which should be avoided at all time.

With this first detailed design for the XRIstel spacecraft structure, a precedent has been set for future developments and continued iterations towards the ultra-stable structure, identifying CFRP as the main structural material to make the XRIstel structure a success.

Reflection on Research Objective, Questions, and Hypothesis

The objective of this study was to design and evaluate an ultra-stable spacecraft structure for the XRIstel mission that satisfies the launch survivability and mission constraints, while minimizing thermo-mechanical deformations during operation. This objective has been partially achieved, with the main achievements centered around the launch survivability and the mission constraints. The multi-octagon (MO-BR) concept satisfies the predefined constraints regarding length, diameter, mass, CoG, eigenfrequencies, launch survivability, and the sinusoidal excitation response.

The operational environment and thus the thermo-mechanical stability during operation has been addressed only partially, with time and computational limitations eliminating the thermal analysis at the L2 environment from this study. While mechanical stability has been assessed for the launch environment, sinusoidal excitation response, and in-orbit micrometeoroid impacts, the thermal behaviour has only been evaluated during launch, after fairing separation. The mechanical stability of the structure showed acceptable stress levels, displacements, and buckling factors for several of the configurations, including the MO-BR configuration. As a result of the micrometeoroid impact, the lateral deformations and the global spacecraft rotation exceed allowable limits, but can quickly return, either passively or actively, to acceptable values. The thermal environment after fairing separation has been identified and can be implemented in future design iterations, while the operational thermal response remains unknown at this stage.

Research Question – *How can a large spacecraft structure be designed to achieve ultra-high thermo-mechanical stability, while satisfying launch survivability, mass, and optical accessibility requirements?*

This study provides a first answer to this question, with a global octagonal structure, consisting of eight circular thin-walled CFRP beams, reinforced support rings, diagonal beams, cross-volume structures, and an even further improved version in the form of a multi-octagon structure (MO-BR). The latter configuration satisfies most of the requirements, while outperforming the single-octagon (SO-BR) structure in every metric.

Joints and interfaces have only been investigated to a limited extend in this study, as the modelling required simplifications in this area. To what extent the joints and structural interfaces will play a part in the structure's stability has not been quantified. Nevertheless, it can be concluded from the many design choices and iterations that joints will play a crucial part in the thermal matching of components, the stress distribution, and the assembly and integration process.

Research Question – *To what extend can material selection enable a large ultra-stable spacecraft structure for the XRIstel mission?*

Material selection has been identified as one of the major design choices that can lead to ultra-stable structures. As highlighted in subsection 4.4.5 and subsection 4.6.2, the material has a significant influence on the structure regarding handling of stress, sizing of structural components, and the thermal behaviour. As a result, the material selection should always be kept in mind during the design process, never fixating on the currently chosen material. Early design such as the design in this study focusses on the strength of the material to satisfy launch survivability. Later design iterations might not have launch survivability as their main design driver, allowing a material with more stiffness instead of strength to outperform the previously chosen material. The M40J/PMT-F33 material as chosen during this study is a high-modulus fibre, with still a focus on material strength. Future developments might benefit from even higher-modulus fibres such as M55J or M60J.

Many material properties are of importance during material selection, of which the obvious ones are density, strength, and stiffness. Additionally, and especially when working with composite materials, the outgassing properties are of importance, as there are stringent requirements on outgassing for space-grade materials. CFRP allows for a wide variety of properties, generally having a very low density, and high specific stiffness and strength. Properties such as the CTE can be tailored by tuning the laminate stacking and layup. This also introduces the material's anisotropy, which can be utilized to reinforce properties in certain directions, while tuning them down in other directions.

Research Hypothesis

It was hypothesized that a spacecraft structure based on advanced composite materials, combined with an optimized structural configuration and a minimized need for connective joints can satisfy the launch survivability, mass, and volume constraints of the XRIstel proposal, while achieving thermo-mechanical stability.

Based on the results of this study, the hypothesis is still supported with respect to the launch survivability, mass, and volume/CoG constraints, with an optimized multi-octagon CFRP configuration. Two main aspects of the hypothesis are not fully supported at this stage: the minimized need for connective joints and the thermo-mechanical stability during operation. The inclusion of joints has not been fully investigated and integrated in the modelling of the structure; thus the effects and the implications are not fully identified and understood. While the thermo-mechanical stability has been assessed and confirmed in two launch phases and right after fairing separation, the main thermal behaviour and response during operation has not been identified, leaving uncertainties regarding operational stability.

8 Recommendations

As this study is an early-phase conceptual design study, many recommendations can be given, but few are considered to be relevant in the near future during the next design steps. These recommendations have been presented here.

- One of the main recommendations is the integration of the optical benches and the fusion between optical benches and the main load path structure. The implementation of the optical benches will, most likely, lead to enhanced structural performance, allowing for trimming of the structural shell created thus far. The near-future implementation of optical benches into the structure will lead to renewed insights in global and local structural and thermal behaviour.

- Due to time and computational constraints, the thermal analysis of the spacecraft at L2 in its operational environment has not been evaluated. It is recommended that future work will incorporate the thermal evaluation of design iterations at L2 for different rotation rates. A frequency domain study is preferred due to its computational efficiency, immediately allowing for the comparison of thermal behaviour for the range of rotation rates (1700 – 23400 s). It should be investigated for which exact purposes the frequency study is valid, as FEM solvers often use a Taylor expansion linearization to compute the radiative non-linear equations. A transient study is often suggested for highly non-linear environments that contain large thermal gradients, but is considered immensely demanding on computational resources.

- The design iteration has utilized CFRP structural elements, without the detailed design of connective joints. It is highly recommended to implement proper modelled and analyses on connective joints to allow for realistic assembly and integration. The evaluation of structural and thermal behaviour due to these connective elements will lead the way for a realistic structure that can be manufactured and assembled, while maintaining sufficient performance. Specific materials to consider are Invar and ALLVAR Alloy 30, which have all extensive heritage as joint structures and show the right characteristics for ultra-stable structures.

- The design has utilized a simplified quasi-isotropic CFRP material, which could theoretically be tailored to specific directional needs. It is recommended that in future structural iterations, the material selection will be expanded by tailoring the layup of the laminates utilized. Additionally, it is recommended to investigate the need or possibility to switch to higher-modulus fibres as soon as material strength is not the dominant requirement anymore. This would be the case once strength is sufficient with such a margin, that lower strength fibres, but with higher modulus, can provide enough strength to survive launch, while providing a higher modulus for stability. Recommended fibres and materials could include the M55J and M60J fibres.

- For future design iterations, it is recommended to continuously monitor the behaviour and response of the structure, including a more detailed response analysis to a spectrum of micrometeoroid impacts. During the current study, a single impact has been modelled and analysed, while the true L2 environment will provide an almost continuous bombardment of smaller and larger micrometeoroids. It is recommended to explore this environment in more detail, gaining insights into pointing stabilities, required AOCS budgets, and the potential need for impact shielding.

- Based on the thermal analysis after fairing separation, the initial solution of connecting the CFRP beams to the aluminium element using the proposed LOCTITE Stycast 2850 FT with CAT 9 seems to be insufficient. Either the connection between CFRP and aluminium should be revisited, or a solution has to be found to retain these connections from warming up beyond the glass transition temperature of the adhesive.

References

[1] Phil Uttley et al. “An x-ray interferometry concept for ESA’s Voyage 2050 programme”. In: *Space Telescopes and Instrumentation 2020: Ultraviolet to Gamma Ray*. Ed. by Jan-Willem A. Den Herder, Kazuhiro Nakazawa, and Shouleh Nikzad. SPIE, Dec. 2020. ISBN: 978-1-5106-3675-0 978-1-5106-3676-7. DOI: 10.1117/12.2562523.

[2] Roland den Hartog. *Preliminary Design Report and Technology Development Roadmap*. Tech. rep. SRON and INFN, Jan. 19, 2026.

[3] ArianeSpace. *Ariane 6 User’s Manual, Issue 2 Revision 0*. Évry-Courcouronnes, France, Feb. 2021. URL: https://ariane.group/app/uploads/sites/4/2024/10/Mua-6_Issue-2_Revision-0_March-2021.pdf.

[4] ECSS. *ECSS-E-HB-32-20 Part 1A: Structural materials handbook - Part 1: Overview and material properties and applications*. European Cooperation for Space Standardization (ECSS). ESA-ESTEC, Requirements & Standards Division, Noordwijk, The Netherlands, Mar. 2011. URL: https://ecss.nl/wp-content/uploads/handbooks/ecss-e-hb/ECSS-E-HB-32-20_Part1A.pdf.

[5] Lee D. Feinberg et al. “Ultra-stable structures lab (USS)”. In: *Space Telescopes and Instrumentation 2022: Optical, Infrared, and Millimeter Wave*. Vol. 12180. SPIE, Aug. 2022. DOI: 10.1117/12.2626490.

[6] Adrianus L Verlaan et al. “LISA Telescope Assembly Optical Stability Characterization for ESA”. In: (2012). URL: https://publications.tno.nl/publication/100803/YbbHXs/verlaan-2012-lisa.pdf.

[7] S. Lucarelli et al. “The Breadboard model of the LISA telescope assembly”. In: *International Conference on Space Optics — ICSO 2012*. Vol. 10564. SPIE, Nov. 2017. DOI: 10.1117/12.2309050.

[8] Karsten Danzmann et al. *Laser Interferometer Space Antenna*. Feb. 2017. DOI: 10.48550/arXiv.1702.00786.

[9] Benjamin Soldo. *Ultrastable Structures for LISA and Beyond*. Apr. 2020. URL: https://ufdcimages.uflib.ufl.edu/IR/00/01/11/42/00001/Ben_Soldo_26APR2020.pdf.

[10] Airbus Defence and Space. *Airbus Defence and Space’s Gaia spacecraft delivers data on 1.1 billion stars*. https://www.airbus.com/en/newsroom/press-releases/2016-09-airbus-defence-and-spaces-gaia-spacecraft-delivers-data-on-11. Sept. 2016.

[11] European Space Agency. *Gaia enters its operational orbit*. https://www.esa.int/Science_Exploration/Space_Science/Gaia/Gaia_enters_its_operational_orbit. Jan. 2014.

[12] E. A. Meijer et al. “Picometer metrology for the GAIA Mission”. In: ed. by Penny G. Warren et al. San Diego, CA, Aug. 2009. DOI: 10.1117/12.826124.

[13] M Bougoin and J Lavenac. “Large and highly stable structures made of SiC”. In: (2012).

[14] ESA ESA. *Constructing the Gaia torus - Gaia - Science Portal*. URL: https://sci.esa.int/web/gaia/-/45332-constructing-the-gaia-torus.

[15] W. Gielesen et al. “Gaia basic angle monitoring system”. In: ed. by James B. Heaney and E. T. Kvamme. San Diego, California, United States, Sept. 2013. DOI: 10.1117/12.2026928.

[16] Michael W. McElwain et al. “The James Webb Space Telescope Mission: Optical Telescope Element Design, Development, and Performance”. In: *arXiv preprint arXiv:2301.01779* (2023). DOI: 10.48550/arXiv.2301.01779.

[17] Renee Gracey et al. “Structural, thermal, and optical performance (STOP) modeling and results for the James Webb Space Telescope integrated science instrument module”. In: *Modeling, Systems Engineering, and Project Management for Astronomy VII*. Ed. by George Z. Angeli and Philippe Dierickx. International Society for Optics and Photonics. SPIE, 2016. DOI: 10.1117/12.2233641.

[18] Albert McKeon. *The Backplane of NASA’s Webb Telescope Offers a Strong, Steady Hand*. URL: https://www.northropgrumman.com/what-we-do/space/spacecraft/webb-telescope/the-backplane-offers-a-strong-steady-hand.

[19] NASA Science. *Webb’s Backplane*. 2024. URL: https://science.nasa.gov/mission/webb/webbs-backplane/.

[20] Cengiz O. Kunt et al. “Development and sizing of the JWST Integrated Science Instrument Module (ISIM) metering structure”. In: *Optomechanical Technologies for Astronomy*. Ed. by Eli Atad-Ettedgui, Joseph Antebi, and Dietrich Lemke. SPIE, 2006. DOI: 10.1117/12.670112.

[21] NASA Goddard Space Flight Center. *NASA Scientific Visualization Studio: ID 20395*. NASA Scientific Visualization Studio. 2024. URL: https://svs.gsfc.nasa.gov/20395.

[22] Habitable Worlds Observatory. *HWO Science*. Habitable Worlds Observatory. URL: https://habitableworldsobservatory.org/science.

[23] Lee D. Feinberg et al. *Habitable Worlds Observatory’s Concept and Technology Maturation: Initial Feasibility and Trade Space Exploration*. 2026. arXiv: 2601.11803.

[24] Alain Carrier et al. “Ultrastability evaluation of pathfinder architecture for Habitable Worlds Observatory”. In: *UV/Optical/IR Space Telescopes and Instruments: Innovative Technologies and Concepts XII*. Ed. by Jonathan W. Arenberg and H. Philip Stahl. Vol. 13623. International Society for Optics and Photonics. SPIE, 2025. DOI: 10.1117/12.3067621.

[25] Aerospace Structures & Materials Dept. Delft University of Technology. *Spacecraft Structures: Lecture Slides*. AEASM1x Module 3 PDF, DelftX / TU Delft Online Learning. 2018. URL: https://delftxdownloads.tudelft.nl/AEASM1x_Introduction_to_Aerospace_Structures_and_Materials/Module_3/AEASM1x_2018_384_Spacecraft_Structures-slides.pdf.

[26] Frances Zhu. “4.4 General Arrangement and Design Drivers”. In: *A Guide to CubeSat Mission and Bus Design*. 1st ed. ISBN: 978-1-948027-11-3.

[27] Harijono Djojodihardjo. “Structural integrity of spacecraft structures subject to motion, thermo-structural dynamics and environmental effects - An overview”. In: *Acta Astronautica* 222 (Sept. 2024). ISSN: 00945765. DOI: 10.1016/j.actaastro.2024.05.034.

[28] Cyril Annarella et al. *Spacecraft Structures*. 1991.

[29] Suraj Rawal. “Materials and structures technology insertion into spacecraft systems: Successes and challenges”. In: *Acta Astronautica* 146 (2018). ISSN: 0094-5765. DOI: https://doi.org/10.1016/j.actaastro.2018.02.046.

[30] Jun Young Choi and Sung-Hoon Ahn. “Mesoscale carbon fiber lattices with foam-like weight and bulk strength”. In: *Nature Communications* 17 (Apr. 2026). ISSN: 2041-1723. DOI: 10.1038/s41467-026-72105-4.

[31] Tony Hull et al. “Addressing the HWO/LISA generation of requirements: How Zerodur®’s attributes and efficient geometries address ultra-stable mirrors and structures”. In: *International Conference on Space Optics — ICSO 2024*. Vol. 13699. SPIE, July 2025. DOI: 10.1117/12.3075139.

[32] SCHOTT. *Technical Details of ZERODUR® Glass-Ceramic*. 2025. URL: https://www.schott.com/en-gb/products/zerodur-p1000269.

[33] ALLVAR. *Creating the Future of Ultra-Stable Telescopes - ALLVAR Alloys*. 2025. URL: https://allvaralloys.com/creating-the-future-of-ultra-stable-telescopes/.

[34] Editorial Team NASA. *A New Alloy is Enabling Ultra-Stable Structures Needed for Exoplanet Discovery - NASA Science*. July 2025. URL: https://science.nasa.gov/science-research/science-enabling-technology/technology-highlights/a-new-alloy-is-enabling-ultra-stable-structures-needed-for-exoplanet-discovery/.

[35] ALLVAR Alloys. *ALLVAR Alloy 30 Round Bar and Tube Sizing: Negative Coefficient of Thermal Expansion Products and Applications*. 2025. URL: https://allvaralloys.com/negative-coefficient-of-thermal-expansion-products-applications/round-bar-and-tube/.

[36] Joseph Robichaud et al. “Silicon carbide optics for space and ground based astronomical telescopes”. In: *Modern Technologies in Space- and Ground-based Telescopes and Instrumentation II*. Vol. 8450. SPIE, Sept. 2012, pp. 31–38. DOI: 10.1117/12.926831.

[37] B Harnisch et al. *Ultra-lightweight C/SiC Mirrors and Structures*. 1998. URL: https://www.esa.int/esapub/bulletin/bullet95/HARNISCH.pdf.

[38] Efthymios Koutsounanos. “Constitutive modeling and characterization of C/C-SiC CMC material”. MA thesis. Delft: Delft University of Technology, 2023. URL: https://repository.tudelft.nl/record/uuid:6c59a621-bee2-4ff2-ae41-02c9a1225950#metadata.

[39] Arceon B.V. *Arceon — Engineering Materials for Extremes*. 2025. URL: https://arceon.nl/.

[40] Sumon Sarkar. *Carbon fiber in space systems*. Mar. 2025. DOI: 10.13140/RG.2.2.16286.86081.

[41] Rizalman Mamat et al. “Carbon fibre for applications in aerospace: A review”. In: *Journal of Alloys and Metallurgical Systems* 12 (Dec. 2025). ISSN: 29499178. DOI: 10.1016/j.jalmes.2025.100227.

[42] Yeong-Deok Noh, Young-Woo Nam, and Byeong-Su Kwak. “Enhanced thermal and mechanical properties of PAN-based carbon/epoxy composites reinforced with graphite sheets and stitched pitch-based carbon fibers”. In: *Polymer Testing* 149 (Aug. 2025). ISSN: 01429418. DOI: 10.1016/j.polymertesting.2025.108856.

[43] Leslie L. Harner. *The Uses for Invar Continue to Multiply*. URL: https://www.carpentertechnology.com/blog/the-uses-for-invar-continue-to-multiply.

[44] High Temp Metals. *Invar 36 Technical Data*. 2015. URL: https://www.hightempmetals.com/techdata/hitempInvar36data.php.

[45] Meltio. *Invar Material Guide: Properties and Additive Manufacturing uses*. URL: https://meltio3d.com/invar-a-historic-alloy-serving-modern-manufacturing/.

[46] Changru Liu et al. “Optimization Design of Core Ultra-Stable Structure for Space Gravitational Wave Detection Satellite Based on Response Surface Methodology”. In: *Aerospace* 11 (June 2024). ISSN: 2226-4310. DOI: 10.3390/aerospace11070518.

[47] B. Argence et al. “Prototype of an ultra-stable optical cavity for space applications”. In: *Optics Express* 20 (Nov. 2012). ISSN: 1094-4087. DOI: 10.1364/OE.20.025409.

[48] Sankalpa Banerjee et al. “Modelling and design of ultra-high stable Fabry–Pérot cavity”. In: *International Journal of Mechanical Sciences* 250 (July 2023). ISSN: 00207403. DOI: 10.1016/j.ijmecsci.2023.108299.

[49] WorkingGroup ECSS. *Space engineering - Structural factors of safety for spaceflight hardware*. Noorwijk, May 2019. URL: https://ecss.nl/wp-content/uploads/2019/05/ECSS-E-ST-32-10C_Rev.2(15May2019).pdf.

[50] European Space Agency (ESA). *Structures - XMM Mechanical Design*. https://www.esa.int/TEC/Structures/SEMH1H91M9H_0.html.

[51] Sana Ullah et al. “Multiscale Modeling of C/SiC Ceramic Matrix Composites (CMCs)”. In: *Engineering Proceedings* 111 (2025). ISSN: 2673-4591. DOI: 10.3390/engproc2025111032.

[52] Vincent Calard et al. *THERMAL, ELECTRICAL AND MECHANICAL PROPERTIES OF CARBON NANOTUBE REINFORCED CYANATE ESTER POLYMER*. Noordwijk, Netherlands. URL: http://esmat.esa.int/materials_news/isme09/pdf/4-New/S6%20-%20Calard.pdf.

[53] Megan Conniff and Mahder Tewolde. *7075 Aluminum Alloy: Composition, Properties, Strength, and Common Uses*. Oct. 2022. URL: https://www.xometry.com/resources/materials/7075-aluminum-alloy/.

[54] Pengcheng Ju et al. “Novel milling cutter structure for high-quality milling of CF/PEEK composites via enhanced shear cutting”. In: *Composites Part B: Engineering* 315 (Apr. 2026). ISSN: 1359-8368. DOI: 10.1016/j.compositesb.2026.113465.

[55] Global VICTREX. *VICTREX PEEK Properties Guide*. Europe, Sept. 2016. URL: https://www.victrex.com/en/material-properties.

[56] NASA. *SPACEMATDB - Space Materials Database. Materials details*. 2006. URL: https://www.spacematdb.com/spacemat/datasearchID.php?name=11833.

[57] Admin eoPortal. *Spektr-RG/SRG - eoPortal*. 14-09-2014. URL: https://www.eoportal.org/satellite-missions/spektrg-srg#spacecraft.

[58] Admin ESA. *Spacecraft - Gaia - Science Portal*. Jan. 2019. URL: https://sci.esa.int/web/gaia/-/39993-spacecraft.

[59] Admin eoPortal. *XMM-Newton (X-ray Multi-Mirror Mission-Newton) - eoPortal*. July 2017. URL: https://www.eoportal.org/satellite-missions/xmm-newton.

[60] M. Menzel et al. “The Design, Verification, and Performance of the James Webb Space Telescope”. In: *Publications of the Astronomical Society of the Pacific* 135 (May 2023), p. 058002. ISSN: 0004-6280, 1538-3873. DOI: 10.1088/1538-3873/acbb9f.

[61] Lockheed Martin Technical Operations. *L2 Natural Environment Summary*. Tech. rep. REV A 3/99. Lockheed Martin Technical Operations, Sept. 1998. URL: https://www.rcktmom.com/njlworks/L2%20Environments%20White%20PaperREVA.pdf.

[62] Ralf Kohley et al. “The radiation environment at L2 as seen by Gaia”. In: *High Energy, Optical, and Infrared Detectors for Astronomy VI*. Vol. 9154. SPIE, July 2014. DOI: 10.1117/12.2056420.

[63] Aditya Garde and Henk Hoevers. *Internal Discussion, mass distribution*. Internal discussion with Henk Hoevers and Aditya Garde on the dimensional parameters of different baselines. May 2026.

[64] Jurriaan Langendorff. *Personal communication on CFRP tube to aluminium mount connections*. Personal communication with Jurriaan Langendorff, PhD student in the Oosterkamp Group. Discussion on the bonding and adhesive joining of CFRP tubes to aluminium mounts, May 2026. May 2026.

[65] Henkel Corporation. *LOCTITE® STYCAST 2850FT CAT 9: Technical Data Sheet*. Henkel Corporation. Oct. 2024. URL: https://datasheets.tdx.henkel.com/LOCTITE-STYCAST-2850FT-CAT-9-en_GL.pdf.

[66] David G. Gilmore. *Spacecraft Thermal Control Handbook*. Second Edition. Vol. Volume I: Fundamental Technologies. El Segundo Boulevard, California 90245-4691: The Aerospace Press, 2002. ISBN: 1-884989-11-X.

[67] Joran Blom. *Design of Flexible Solar Arrays for Small Satellites*. Leiden, 2021.

[68] R. Willingale. “A practical system for X-ray Interferometry”. In: vol. 1. Leicester, May 2004. DOI: 10.1117/12.552917.

[69] Webster Cash et al. “Laboratory detection of X-ray fringes with a grazing-incidence interferometer”. In: *Nature* 407 (Sept. 2000). ISSN: 1476-4687. DOI: 10.1038/35025009.

[70] Yoshio Suzuki. “Measurement of x-ray coherence using two-beam interferometer with prism optics”. In: *Review of Scientific Instruments* 75 (Apr. 2004), pp. 1026–1029. ISSN: 0034-6748, 1089-7623. DOI: 10.1063/1.1651640.

[71] Toray Carbon Fibers Europe. *Torayca M40J Carbon Fiber Data Sheet*. Toray Carbon Fibers Europe S.A. Paris, France, July 2024. URL: https://toray-cfe.com/wp-content/uploads/2025/02/Torayca-M40J-Technical-Data-Sheet.pdf.

[72] Toray Carbon Fibers Europe. *Torayca M55J Carbon Fiber Data Sheet*. Toray Carbon Fibers Europe S.A. Paris, France, July 2024. URL: https://toray-cfe.com/wp-content/uploads/2025/02/Torayca-M55J-Technical-Data-Sheet.pdf.

[73] Toray Advanced Composites. *RS-3 Cyanate Ester Product Data Sheet*. Tech. rep. Toray Advanced Composites. URL: https://www.toraytac.com/product-explorer/products/o90_/RS-3RS-3C.

[74] Patzmandt. *PMT F33 Toughened Cyanate Ester Resin System and M55J Composite Properties*. Patzmandt. URL: https://www.patzmandt.com/systems.

[75] Hexcel Corporation. *HexPly® 954-3 US Product Data Sheet*. Hexcel Corporation. 2024. URL: https://www.hexcel.com/wp-content/uploads/2025/12/HexPly_9543_us_DataSheet.pdf.

[76] Nachiket Dighe. *Numerical-Experimental Analysis of CFRP Specimen under Multi-Directional Thermo-Mechanical Loading*. Delft, 2025. URL: https://resolver.tudelft.nl/uuid:750566ed-d326-4185-b550-d399b85fa95b.

[77] Michael Scheerer et al. “ANALYSES AND TESTING OF THE THERMO-MECHANICAL BEHAVIOUR OF CRYOGENIC COMPOSITE PROPELLANT FEED LINES”. In: Apr. 2014. URL: https://

www.researchgate.net/publication/277714239_ANALYSES_AND_TESTING_OF_THE_THERMO-MECHANICAL_BEHAVIOUR_OF_CRYOGENIC_COMPOSITE_PROPELLANT_FEED_LINES.

[78] Secretariat ECSS. *Buckling of Structures*. Tech. rep. ECSS-E-HB-32-24A. European Cooperation for Space Standardization (ECSS), Mar. 2010. URL: https://ecss.nl/wp-content/uploads/standards/ecss-h/ECSS-HB-32-24A24March2010.pdf.

[79] Secretariat ECSS. *Space Engineering: Structural General Requirements*. Tech. rep. ECSS-E-ST-32C Rev.1. European Cooperation for Space Standardization (ECSS), Nov. 2008. URL: https://ecss.nl/wp-content/uploads/standards/ecss-e/ECSS-E-ST-32C_Rev.115November2008.pdf.

[80] Masae Kanda, Kazuaki Matsumoto, and Sataro Yamaguchi. "Heat transfer through multi-layer insulation (MLI)". In: *Physica C: Superconductivity and its Applications* 583 (2021), p. 1353799. ISSN: 0921-4534. DOI: https://doi.org/10.1016/j.physc.2020.1353799.

[81] SQUID3 Space. *Aluminized Teflon FEP Film*. https://www.squid3.space/product-page/aluminized-teflon. n.d.

[82] SQUID3 Space. *ITO Coated Aluminized Kapton Film*. https://www.squid3.space/product-page/ito-coated-aluminized-kapton-film. n.d.

[83] AZ Technology, Inc. *AZ-93 White Thermal Control Paint*. https://www.aztechnology.com/product/1/az-93. 2026.

[84] John H. Henninger. *Solar Absorptance and Thermal Emittance of Some Common Spacecraft Thermal-Control Coatings*. NASA Reference Publication NASA-RP-1121. NASA Goddard Space Flight Center, Apr. 1984. URL: https://ntrs.nasa.gov/api/citations/19840015630/downloads/19840015630.pdf.

[85] Spectrolab, Inc. *28.3% Ultra Triple Junction (UTJ) Solar Cells*. Oct. 2010. URL: https://www.spectrolab.com/DataSheets/cells/PV%20UTJ%20Cell%205-20-10.pdf.

[86] António P.C. Duarte et al. "Thermal response of pultruded glass fibre-reinforced polymer profiles subjected to outdoor environmental conditions". In: *Construction and Building Materials* 463 (2025). ISSN: 0950-0618. DOI: https://doi.org/10.1016/j.conbuildmat.2025.139971.

A

X-Ray Interferometry Fundamentals and Principles

Interferometry, more specifically VLBI is already a mature measurement technique for radio astronomy, relying on the combination of 2 or more antennas to simulate a large telescope to create high-resolution images by measuring interference patterns, fringes. The same principle can be applied to X-ray signals instead of radio signals, reducing the required baseline lengths significantly, due to the much smaller wavelengths of X-rays in comparison to radio-waves. In this section, the basic principle of XRI is explained, while also providing a proposed system setup by (Willingale [68]), and finally the proposal of the XRIstel which is in early development and of which this study is part.

Basic Principle of X-Ray Interferometry

The study as presented by (Willingale [68]) discussed the basic principles of X-ray interferometry and the scientific advantages it brings. XRI has the potential to provide imaging capabilities with ultra-high angular resolutions up to 100 μas or even better. Though the design and implementation of such a system is not straightforward and requires advanced technological developments regarding optics and stability. Achieving a sufficiently high collecting area while minimizing the required mass and volume to a single spacecraft brings engineering challenges that still need to be addressed. In comparison to radio bandwidths, X-rays have an extremely small wavelength, which would allow XRI to acquire a very high angular resolution with relatively small baselines. Previous experiments with a baseline of 1 mm showed fringes at 1.25 keV, 1 nm wavelength, equivalent to an angular resolution of 0.1 as at the source (Cash et al. [69]). In a separate experiment at a wavelength of 0.1 nm, the angular resolution of 20.0 mas was obtained using an effective baseline of 0.3 mm (Suzuki [70]). These experimental results indicated that high angular resolution with XRI is possible.

The diffraction limit results in an Airy disk as point spread function (PSF) for an unobstructed and circular aperture with a diameter of D. To which Rayleigh's criterion imposes the diffraction limited resolution through $\Delta\theta = 1.22\lambda/D$, where λ is the wavelength. In order to achieve this diffraction limited resolution, all the optical paths must be identical, which can be done for a thins lens in the optical bandwidth by using a dielectric retarder. Similarly, in the case of reflection instead of refraction, a normal incidence mirror has to be parabolic to achieve the same diffraction limited resolution result. Both of these options are unsuitable for X-rays. For X-rays, two grazing incidence reflections at X-ray wavelengths and identical path lengths could provide diffraction limited imaging for a small field of view (FOV) (Willingale [68]).

To obtain two-source interference fringes, the geometry depicted in Figure A.1 can be used. This image depicts two incident beams from two different angles with each a beam width of W. These beams converge towards the left until they fully overlap, creating a volume where interference fringes can be observed. The length L is an arbitrary length that is needed for the two beams to overlap.

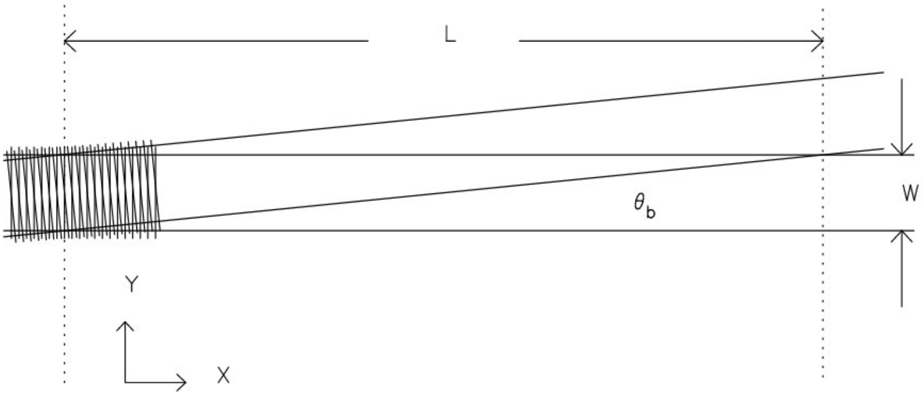

Figure A.1: Required geometry to produce two-source interference fringes (Willingale [68]).

The wavelength λ can be divided by the angle between the two incident beams, θ_b, to obtain the y-direction fringe spacing, Δy. This angle, θ_b, can be obtained by dividing the beam width W by the length required to let the beams overlap, L. To obtain the number of fringes seen in the overlapping volume, the beam width W should simply be divided by the fringe spacing, Δy, to obtain N_f. The combination and manipulation of these equations finally result in the equations for fringe spacing and beam width as indicated below.

$$\Delta y = \sqrt{\frac{\lambda L}{N_f}} \tag{A.1}$$

$$W = \sqrt{\lambda L N_f} \tag{A.2}$$

When the beam width is very small, many identical systems must be operational in parallel to achieve a sufficiently large collecting area. To minimize the number of identical systems needed, the parameter L must be maximized, essentially requiring a longer instrument.

Willingale's Proposed Design

(Willingale [68]) describes in his paper an initial proposal for a relatively simple setup that could provide XRI capabilities. The proposed design utilizes a 20 meter long instrument with a diameter of 2 meter, as such as system would provide sufficient sensitivity for a broad range of X-ray targets. The setup consists of four flat mirrors that are used to collect two bundles with a width W and a separation $D = 2R$ from the aperture to produce the overlapping beams as depicted in Figure A.2, where the mirror configuration can be seen.

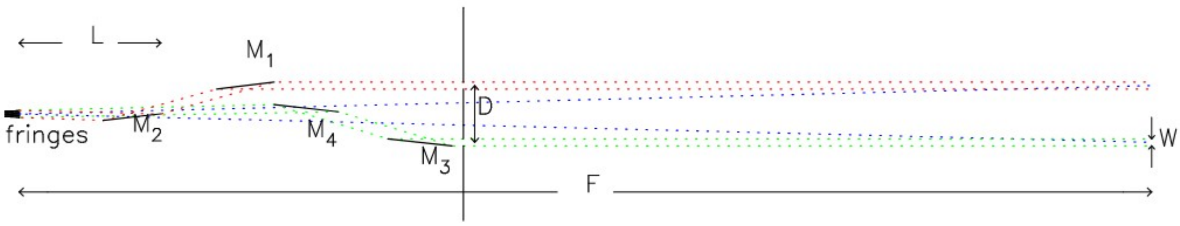

Figure A.2: Four flat mirror configuration which is depicted not to scale and provided by (Willingale [68]).

All mirrors are positioned with grazing angles that provide high reflectivity and operate in the soft X-ray band between 0.1 and 2.0 keV, which requires grazing angles at roughly 2°. The proposed configuration is in many ways similar to the setup used by (Cash et al. [69]), but with minor differences regarding for example the placement of M_2 being closer to the location of maximum overlap in the design by (Willingale [68]).

The collecting area of this single four-mirror setup is still insufficient to allow high-resolution XRI imaging. Hence, (Willingale [68]) proposes to implement a series of identical configurations stacked and operating in parallel. To allow for the stacking of multiple duplicates, mirrors M_1, M_3, and M_4 must be extended in the axial direction and mirror M_2 must be split and turned into a slatted mirror. The principle of this slatted mirror is depicted in Figure A.3

and allows for the beams originating from M_4 to be divided into a series of beams with width W. These beams are then combined with the reflected beam set coming from M_1 due to the slatted mirror. The slatted M_2 mirror essentially serves as a macroscopic transmission grating.

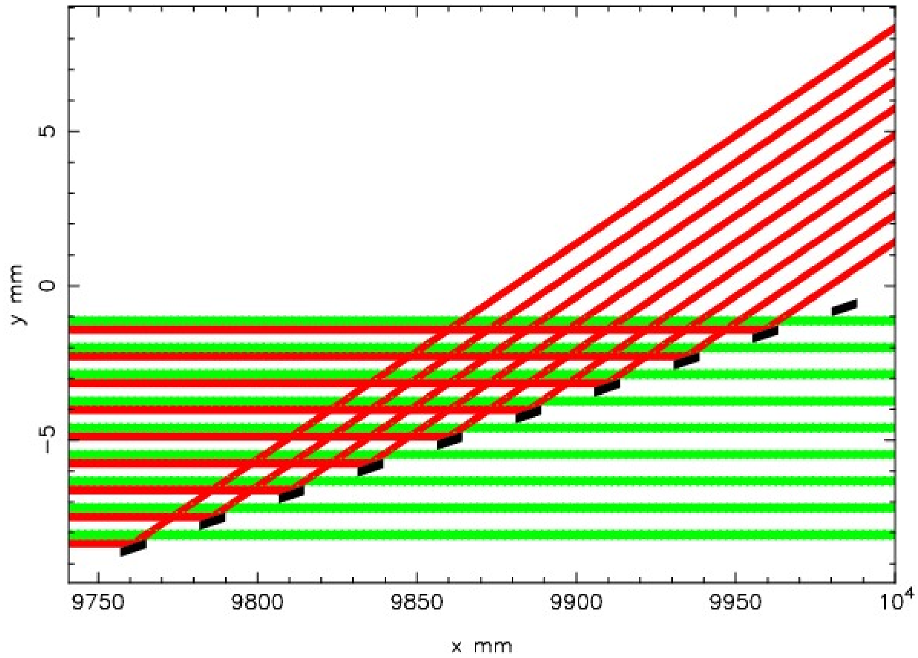

Figure A.3: Beam paths for the slatted mirror configuration, where each slat is a long thin mirror extending into the plane of the paper (Willingale [68]).

Optical Path Difference & Stability

The proposal by (Willingale [68]) also explains how the optical path differences (OPD) can be determined and where they lead to. The study shows that the optical path difference can be calculated by subtracting the path length P_{34} from path length P_{12}, where the subscripts are respective to the mirrors.

$$\Delta = P_{12} - P_{34} = -\Delta L\left(\frac{1}{\cos(\theta_b/2)} - 1\right) + 2y\sin(\theta_b/2) + D\sin(\theta) \tag{A.3}$$

Where θ is the off-axis angle of the x-ray source, which is the same for both arms and all positions across the detector. y is herein the position across the detector plane. The difference in optical paths between the two arms are the reason that interference fringes become visible. The first term in Equation A.3 is a fixed term and does not influence the outcome, the coincidence point on the detector plane at $\Delta = 0$ can be determine by the equation below.

$$y = -\frac{D\sin(\theta)}{2\sin(\theta_b/2)} \approx -F\theta \tag{A.4}$$

The small-angle approximation can be applied to the above equation, with additionally the focal length F defined as follows.

$$F = \frac{R}{\tan(\theta_b/2} \approx \frac{D}{\theta_b} \tag{A.5}$$

This indicates that the interferometer can be seen as a telescope with focal length F, the center of the fringe pattern at the expected location of an off-axis angled point source. The negative sign originates from the expected inversion of the focal plane in lateral direction.

According to (Willingale [68]), the baseline separation D is determined by the distances between the mirror centres as follows.

$$D = \frac{d_{12} + d_{34}}{\sin(2\theta_g)} \tag{A.6}$$

Where d_{12} is the distance between mirror centres of M_1 and M_2, d_{34} respectively represent the same, while θ_g is the grazing incidence angle. These baseline distances can be reduced to a minimum value at $D_{min} = 4WN_s$, with W the beam width and N_s the number of slats in mirror M_2. Distances below this minimum would lead to loss of observed fringes due to the mirror edges blocking optical paths and the outer slats in M_2 not doing anything. Hence, in principle it is possible to go below D_{min}, but not without loss of collecting area and thus this should be avoided.

To ensure identical two beams, distances d_{12} and d_{34} must be the same and in case the baseline, both mirrors M_1 and M_3 must be repositioned. An off-axis angle, θ, would result in a path difference according to Equation A.3, indicating that distances d_{12} and d_{34} are coupled to the pointing direction θ. This coupled relation between the distances and the pointing direction is why the visibility and the phase of the fringes contains data on the angular distribution of the source.

The total OPD between the two beams must be smaller than the coherence length of the X-rays to preserve fringe visibility. For astronomical observations, the source spectrum is generally dominated by continuum radiation for which the coherence length is based on the detector system's energy resolution. For charge-coupled device (CCD) detectors operating around 1 keV, the coherence length corresponds to about 10 wave cycles, which imposes stringent stability requirements. The difference $d_{12} - d_{34}$ must be controlled to the order of 10 nm, or equivalently the pointing must satisfy $\theta < \frac{10\lambda}{D}$. For a baseline of 10 mm, this would result in a maximum allowable pointing error of 0.2 arcsecond (Willingale [68]).

B

Additional Spacecraft Requirements

Table B.1: Additional system requirements and constraints for the XRIstel spacecraft structure. HR = Hard Requirement, SR = Soft Requirement.

ID	Title	Description
HR-019	Optical path differences	Optical path differences should be kept within 0.1 - 1 nm. During operation (2π rotation) and collection of fringes the optical path differences need to be per requirement. Alternatively they can be monitored and corrected for in data processing with the same accuracy.
HR-020	Pointing accuracy (1)	The pointing of the telescope should be stable to $\leqslant 118$ µarcseconds.
HR-021	Acoustic vibration on ground	The spacecraft must be able to withstand 94 dB acoustic noise on ground (ArianeSpace [3]).
HR-022	Ground thermal environment	The spacecraft must withstand extended duration of the by ArianeSpace defined ground thermal environment [3].
HR-023	Thermal conditions before fairing jettisoning	The spacecraft must be able to withstand a net flux density from the fairing of 1000 W/m^2 not taking the spacecraft thermal dissipation power into consideration (ArianeSpace [3]).
HR-024	Transversal inertia	The transverse inertia momentums expressed at the CoG must be $<$90000 kg·m^2. The nominal spacecraft transverse momentums at the CoG in any axes perpendicular to the launcher longitudinal direction must satisfy the requirement (ArianeSpace [3]).
HR-025	Roll inertia	The roll inertia momentums expressed at the CoG must be $<$45000 kg·m^2. The nominal spacecraft roll inertia momentums expressed at the spacecraft CoG in the spacecraft axis parallel to the launcher longitudinal direction must meet this requirement (ArianeSpace [3]).
HR-026	Safety factors qualification and testing	For qualification and testing the flight limit levels should be increased according to ArianeSpace's margins. For different spacecraft tests, different safety factors are given that the spacecraft should satisfy. Depending on who dictates the highest safety factor, either the safety factor from ArianeSpace or according to ECSS is applied (ArianeSpace [3], ECSS [49]).
SR-003	Pointing accuracy (2)	The pointing of the telescope should be stable to 5 - 10 µarcsec or 25-50 prad. Although this is not the hard limit, the aim of the system is to achieve this pointing accuracy.

C
Carbon Fibre / Resin / UD Ply Properties

This appendix summarized the material data and analytical approximations used to derive the orthotropic material properties of several quasi-isotropic CFRP laminates. The derivation follows a two-step homogenization process, which are derived in detail in Appendix D and Appendix E.

Raw Fibre Properties
In order to extract three-directional material properties, it is needed to define the material properties of a unidirectional (UD) single-ply of carbon fibre with resin incorporated. Several different carbon fibres have been considered in combination with several different resins. Appendix D discusses the analytical approximations through micromechanics to determine UD ply properties for different combinations

The fibres considered for the CFRP laminates are mainly the Toray M40J and M55J fibres, these are high modulus carbon fibres with great mechanical properties, as well as heritage in the space industry. According to (McKeon [18]), the M55J fibres are also utilized in the large backplanes of the JWST mirrors, suggesting that they exhibit the right properties for large spacecraft applications. The neat fibre properties can be found in Table C.1

Additionally, Table C.4 depicts available data on UD plies from different fibre/resin combinations, as well as UD ply properties of CF/PEEK. The immediately available UD ply properties of IM7/8552 can be utilized to approximate a quasi-isotropic laminate, while the UD ply properties of M55J/PMT-F33 and M55J/954-3 can be used to verify the current micromechanics approach for approximating the UD ply properties of fibre/resin combinations.

Resin Matrix Options
The ECSS standards (ECSS [4]) provide data on different fibres, resins, and their properties. Section 3.2.2 from the ECSS-E-HB-32-20-1A document provides some mechanical properties of three different epoxies. Whereas section 6.6.4 discusses specifically the resin properties of Narmco 5208. With sections 5.3.2 & 5.9.2 providing additional mechanical and thermal properties of certain materials and laminate combinations. Narmco 5208 is a common epoxy resin used for composite laminates, and is therefore considered. Additionally, three more resins have been considered, all of which are cyanate ester resins, known for their extremely low outgassing and moisture absorption, making them ideal for space applications. All resin properties can be found in Table C.2.

Table C.1: Comparison of material properties for the Toray M40J and M55J carbon fibres. The material properties are uni-directional along the fibres. Data provided by (Toray Carbon Fibers Europe [71], Toray Carbon Fibers Europe [72]).

Fibre	Tensile Strength [MPa]	Young's Modulus [MPa]	Density [kg/m^3]	Specific Heat [J/(kg·K)]	CTE [1/K]	Thermal Cond. [W/(m·K)]
M40J	4400	377000	1750	711.3	-8.3×10^{-7}	68.6
M55J	4020	540000	1910	711.3	-1.1×10^{-6}	155.7

To validate the micromechanics approach to obtain UD ply properties, the `Python Input` for M55J/PMT-F33 and M55J/954-3 can be compared against the available ply properties as defined in Table C.4 and summarized in Table C.3. As can be seen from the comparison, most of the values are very close, and at the least in the same ballpark as the available data, providing confidence in the micromechanics approach for UD ply data. Some of the values differ slightly, most likely due to the simplified approximation and assumptions contained within the micromechanics approach. Additionally, the compressive strength for the HexPly-954-3 resin has been assumed to be the same as for PMT-F33 because of lacking data from the supplier.

Table C.2: Resin material data on Narmco 5208 (ECSS [4]), RS-3/RS-3C (Toray Advanced Composites [73]), PMT-F33 (Patzmandt [74]), and HexPly 954-3 (Hexcel Corporation [75]).

Property	Unit	Narmco 5208	RS-3/RS-3C	PMT-F33	HexPly 954-3
Density	kg/m^3	1260	1190	1190	1190
Tensile strength	MPa	54.5	80	72.40	57
Tensile modulus	MPa	3930	3000	3034	2800
Compressive strength	MPa	-	-	139.3	-
Compressive modulus	MPa	-	-	3999	-
Poisson's ratio	–	0.35	0.35*	0.35*	0.35*
Specific heat	J/(kg·K)	1100	-	-	-
CTE	$\times 10^{-6}$ 1/K	40	43	-	55.1
Thermal conductivity	W/(m·K)	0.5	-	-	-
Outgassing (TML)	%	-	0.22	0.21	0.20
Outgassing (RML)	%	-	-	-	0.16
Outgassing (CVCM)	%	-	0.01	0.01	0.01

*Assumed value as typical values range from 0.3 to 0.4 for cyanate ester resins.

Table C.3: Comparison between available UD ply data and approximated data through micromechanics for M55J/PMT-F33 and M55J/954-3

Property	Unit	M55J/PMT-F33 Available	M55J/954-3 Available	M55J/PMT-F33 Approximated	M55J/954-3 Approximated
Tensile modulus (0°)	GPa	338	324	325	325
Tensile modulus (90°)	GPa	9.0	6.2	7.7	7.4
Tensile strength (0°)	MPa	2137	2303	2441	2435
Tensile strength (90°)	MPa	33	35	36	29
Compression strength (0°)	MPa	883	951	880	880
Compression modulus (0°)	GPa	317	306	325	325

Table C.4: Comparison of unidirectional (UD) ply material properties at 293 K. Elastic material properties of IM7/5208 are taken from (Dighe [76]) (Table 2.11 and Table 2.12), originally sourced from (Scheerer et al. [77]) (Table 4). Anisotropic material properties of CF/PEEK are based on (Ju et al. [54]). The coefficient of thermal expansion (CTE) for CF/PEEK is not provided in the primary source and is therefore taken from CF/PEEK (90HMF40) data by VICTREX (VICTREX [55]). The properties of the M55J/PMT-F33 combination is provided by (Patzmandt [74]). The properties of the M55J/954-3 are provided by (Hexcel Corporation [75]). Direction 1 corresponds to the fibre direction (0°), while directions 2 (90°) and 3 (out-of-plane) are transverse to the fibres.

Property	Unit	IM7/5208	CF/PEEK	M55J/PMT-F33	M55J/954-3
E_1	GPa	160	127	338	324
E_2	GPa	9.6	10.3	9.0	6.2
E_3	GPa	9.6	10.3	-	-
G_{12}	GPa	5.01	5.7	-	-
G_{13}	GPa	5.01	5.7	-	-
G_{23}	GPa	3.56	3.2	-	-
ν_{21}	–	0.0162	0.0243	-	-
ν_{31}	–	0.0162	0.0243	-	-
ν_{32}	–	0.34	0.30	-	-
α_1	$\times 10^{-6}$ 1/K	-0.05	3.0	-	-
α_2	$\times 10^{-6}$ 1/K	33.8	35.0	-	-
α_3	$\times 10^{-6}$ 1/K	33.8	35.0	-	-
λ_1	W/(m·K)	-	5.5	-	-
λ_2	W/(m·K)	-	0.75	-	-
λ_3	W/(m·K)	-	0.75	-	-
Tensile strength (0°)	MPa	-	-	2137	2303
Tensile strength (90°)	MPa	-	-	33	35
Compression strength (0°)	MPa	-	-	883	951
Compression modulus (0°)	GPa	-	-	317	306

D

Analytical Approximation of UD Ply Properties

This appendix describes the approach used for the analytical approximation of UD ply properties through a micromechanics approach.

Variable Definitions:

E	Young's modulus
G	Shear modulus
ν	Poisson's ratio
α	Coefficient of thermal expansion
λ	Thermal conductivity
V_f	Fibre volume fraction
V_m	Matrix volume fraction
$_f$	Fibre property
$_m$	Matrix property
$_{11}$	Fibre direction
$_{22}$	Transverse in-plane direction
$_{33}$	Through-thickness direction

Unidirectional Ply Properties

The elastic and thermal properties of a unidirectional ply can be estimated using relations between fibre and matrix properties. A constant fibre volume fraction of $V_f = 0.60$ is assumed, with matrix fraction:

$$V_m = 1 - V_f \tag{D.1}$$

The longitudinal Young's modulus along the fibre direction can be approximated using the Rule of Mixtures (ROM):

$$E_{11} = V_f E_f + V_m E_m \tag{D.2}$$

The transverse modulus is matrix dominated and is approximated using the Halpin–Tsai relation:

$$E_{22} = E_m \frac{1 + \xi_E \eta_E V_f}{1 - \eta_E V_f} \tag{D.3}$$

with:

$$\eta_E = \frac{\dfrac{E_{f2}}{E_m} - 1}{\dfrac{E_{f2}}{E_m} + \xi_E} \tag{D.4}$$

where E_{f2} is an assumed transverse fibre modulus and ξ_E is a shape parameter, typically taken as $\xi_E = 2$.

The out-of-plane modulus is assumed equal to the transverse modulus:

$$E_{33} \approx E_{22} \tag{D.5}$$

The in-plane shear modulus of a single ply can also be approximated using the Halpin–Tsai relation:

$$G_{12}^{ply} = G_m \frac{1 + \xi_G \eta_G V_f}{1 - \eta_G V_f} \tag{D.6}$$

with:

$$\eta_G = \frac{\dfrac{G_{f12}}{G_m} - 1}{\dfrac{G_{f12}}{G_m} + \xi_G} \tag{D.7}$$

where the matrix shear modulus is derived from isotropic elasticity relations:

$$G_m = \frac{E_m}{2(1 + \nu_m)} \tag{D.8}$$

and ξ_G is a shape parameter, typically taken as $\xi_G = 1$.

The remaining shear moduli are assumed equal:

$$G_{13}^{ply} = G_{23}^{ply} = G_{12}^{ply} \tag{D.9}$$

The major Poisson's ratio is approximated using the Rule of Mixtures:

$$\nu_{12} = V_f \nu_f + V_m \nu_m \tag{D.10}$$

Thermal Properties of a Single Ply

The longitudinal thermal conductivity along the fibre direction of a single ply is approximated using the Rule of Mixtures:

$$\lambda_{11} = V_f \lambda_f + V_m \lambda_m \tag{D.11}$$

The transverse thermal conductivity is assumed to be matrix dominated:

$$\lambda_{22} \approx \lambda_{33} \approx \lambda_m \tag{D.12}$$

The longitudinal coefficient of thermal expansion (CTE) is calculated using a stiffness weighted rule of mixtures:

$$\alpha_{11} = \frac{V_f E_f \alpha_f + V_m E_m \alpha_m}{V_f E_f + V_m E_m} \tag{D.13}$$

The transverse CTE is approximated using a simple mixture relation between fibre and matrix transverse expansion:

$$\alpha_{22} = V_f \alpha_{f2} + V_m \alpha_m \tag{D.14}$$

The out-of-plane expansion is assumed equal to the transverse value:

$$\alpha_{33} \approx \alpha_{22} \tag{D.15}$$

E

Analytical Approximation Quasi-Isotropic Laminate Properties

This appendix describes the analytical approximation of a quasi-isotropic laminate properties, building upon the UD ply properties as defined in Appendix C and Appendix D.

Quasi-Isotropic Laminate Properties

For a symmetrical quasi-isotropic laminate consisting of $0^\circ/\pm 45^\circ/90^\circ$ plies, the in-plane properties are determined using Classical Laminate Theory (CLT). Firstly, the reduced stiffness matrix Q for a single unidirectional ply in the material coordinate system is defined as:

$$Q = \begin{bmatrix} Q_{11} & Q_{12} & 0 \\ Q_{12} & Q_{22} & 0 \\ 0 & 0 & Q_{66} \end{bmatrix} \tag{E.1}$$

with:

$$Q_{11} = \frac{E_{11}}{1 - \nu_{12}\nu_{21}}, \quad Q_{22} = \frac{E_{22}}{1 - \nu_{12}\nu_{21}}, \quad Q_{12} = \frac{\nu_{12}E_{22}}{1 - \nu_{12}\nu_{21}}, \quad Q_{66} = G_{12}^{ply} \tag{E.2}$$

where the minor Poisson's ratio follows from:

$$\nu_{21} = \nu_{12}\frac{E_{22}}{E_{11}} \tag{E.3}$$

Each ply is transformed to the laminate coordinate system using standard transformation relations, resulting in the transformed stiffness matrix $\bar{Q}$ for each ply. The laminate extensional stiffness matrix A is obtained by:

$$A = \sum_{k=1}^{n} \bar{Q}^{(k)} t_{ply} \tag{E.4}$$

where t_{ply} is the thickness of a single ply and n is the total number of plies.

The effective in-plane engineering constants of the laminate are then determined from the inverse of the A-matrix:

$$\begin{bmatrix} \varepsilon_x \\ \varepsilon_y \\ \gamma_{xy} \end{bmatrix} = A^{-1} \begin{bmatrix} N_x \\ N_y \\ N_{xy} \end{bmatrix} \tag{E.5}$$

From this, the laminate properties are obtained as, where $h = n\, t_{ply}$ is the total laminate thickness:

$$E_1^{lam} = \frac{1}{A_{11}^{-1}\, h}, \quad E_2^{lam} = \frac{1}{A_{22}^{-1}\, h} \tag{E.6}$$

$$G_{12}^{lam} = \frac{1}{A_{66}^{-1}\, h} \tag{E.7}$$

$$\nu_{12}^{lam} = -\frac{A_{12}^{-1}}{A_{11}^{-1}} \tag{E.8}$$

Out-of-Plane Laminate Properties

The out-of-plane modulus is assumed to be dominated by the transverse ply modulus:

$$E_3^{lam} \approx E_{33} \tag{E.9}$$

The Poisson's ratios are estimated using the reciprocity relation for orthotropic materials:

$$\nu_{31}^{lam} = \nu_{13}^{lam} \left(\frac{E_3^{lam}}{E_1^{lam}} \right) \tag{E.10}$$

where the main Poisson ratio is approximated using the matrix Poisson's ratio scaled with stiffness ratios:

$$\nu_{13}^{lam} \approx \nu_m \tag{E.11}$$

The transverse shear moduli are assumed equal to the ply values:

$$G_{13}^{lam} = G_{23}^{lam} = G_{12}^{ply} \tag{E.12}$$

Laminate Thermal Conductivity

The laminate in-plane thermal conductivity is assumed to be approximately isotropic and reduced compared to the fibre direction due to the multidirectional stacking sequence. The effective in-plane conductivity is approximated:

$$\lambda_1^{lam} = \lambda_2^{lam} \approx \frac{\lambda_{11}}{4} \tag{E.13}$$

reflecting the distribution of fibre orientations in the laminate.

The out-of-plane thermal conductivity is assumed to be dominated by the matrix material:

$$\lambda_3^{lam} \approx \lambda_m \tag{E.14}$$

Laminate Strength Estimation

The tensile strength of a unidirectional ply in the fibre direction is estimated using the Rule of Mixtures:

$$\sigma_{UD,t} = V_f \sigma_{f,t} + V_m \sigma_{m,t} \tag{E.15}$$

The compressive strength of the unidirectional ply is taken from available fibre data.

For a quasi-isotropic laminate, the strength is reduced due to the multidirectional stacking sequence. This reduction is approximated using a scaling factor f_0, representing the fraction of fibres aligned with the loading direction:

$$\sigma_{lam,t} = f_0 \sigma_{UD,t} \tag{E.16}$$

$$\sigma_{lam,c} = f_0 \sigma_{UD,c} \tag{E.17}$$

where a typical value of

$$f_0 = 0.25 \tag{E.18}$$

is used for a $0^\circ / \pm 45^\circ / 90^\circ$ laminate.

Laminate Density

The laminate density is estimated using the Rule of Mixtures:

$$\rho_{lam} = V_f \rho_f + V_m \rho_m \tag{E.19}$$

These calculated laminate properties are then used as input parameters for the structural analysis code.

F
Analytical Geometry Comparison

To obtain first-order approximations on the differences between a circular thin-walled beam cross-section and an octagonal thin-walled beam cross-section, they have been analytically described for simple load cases. The analytical comparison followed the approach as described in this section, with several important assumptions to be noted.

Assumptions

- The loads considered are 6.0 g (longitudinal) and 1.8 g (lateral), with a 100 kg added tip mass. No additional safety factor was applied, as the focus is on the comparison and not absolute performance.
- Both cross-sections have an arbitrary maximum outer diameter of 200 mm and an arbitrary wall thickness of 2.5 mm.
- The material properties of C/C-SiC are considered for both beams.
- The material behaviour is assumed to be linear elastic.
- No local buckling, shell buckling, imperfections, or connection effects are taken into account.
- Beams are considered as perfect cantilever beams for buckling and bending.
- Combined loading is not considered to isolate the fundamental geometrical performance.

Geometrical Properties

For both the circular and the octagonal cross-section, the cross-sectional area A and the second moment of inertia I can be determined. For the circular cross-section as follows:

$$A = \frac{\pi}{4}\left(D^2 - d^2\right) \tag{F.1}$$

$$I = \frac{\pi}{64}\left(D^4 - d^4\right) \tag{F.2}$$

with inner diameter $d = D - 2t$. For the octagonal cross-section, it can be approximated as the difference between the outer and inner octagon, following:

$$A = A_{\text{outer}} - A_{\text{inner}} \tag{F.3}$$

$$I = I_{\text{outer}} - I_{\text{inner}} \tag{F.4}$$

This follows the determination of the apothem h and the side length a, which for an octagon defined by circumradius R (distance center to corner), are given by:

$$h = R\cos\left(\frac{\pi}{8}\right) \tag{F.5}$$

$$a = 2R\sin\left(\frac{\pi}{8}\right) \tag{F.6}$$

The area of a solid octagon is:

$$A = \frac{8}{2}ah \tag{F.7}$$

The polar moment of inertia is approximated:

$$I_p = A\left(\frac{h^2}{2} + \frac{a^2}{24}\right) \tag{F.8}$$

and the planar second moment of inertia is:

$$I = \frac{I_p}{2} \tag{F.9}$$

The hollow octagonal cross-section is obtained by subtracting the inner octagon from the outer octagon.

Mass per beam

The mass for an individual beam can be computed using:

$$m = \rho A L \tag{F.10}$$

with ρ being the density, A the cross-sectional radius, and L the length of the beam.

Load Distribution

The beams are carrying their own respective mass m_{beam} and an additional 100 kg on the top of each beam. To be consistent with the FEM verification, the load on a single beam can be divided into:

$$F_{\text{top}} = m_{\text{top}} a, \quad F_{\text{beam}} = ma, \quad w = \frac{m}{L} a \tag{F.11}$$

The two load cases considered in the comparison are:

- Longitudinal acceleration (a_{long}) (6.0 g)
- Lateral acceleration (a_{lat}) (1.8 g)

Longitudinal Performance

The longitudinal performance can be assessed by looking at the nominal maximum stress, the average surface stress, and the tip displacement. The effective longitudinal force can be determined by:

$$\sigma_{\text{axial}} = \frac{F}{A} \tag{F.12}$$

The effective force can be written as:

$$F_{eff} = F_{top} + \frac{F_{beam}}{2} \tag{F.13}$$

where the F_{top} is the force due to the additional mass at the top of the beam, and F_{beam} is the distributed force due to the beam's own mass simplified to an acting point load at the middle of the beam. The average surface stress, tip displacement, and maximal axial stress can be determined as follows:

$$\sigma_{\text{avg}} = \frac{F_{\text{eff}}}{A}, \quad \delta_{\text{long}} = \frac{F_{\text{eff}} L}{EA} \tag{F.14}$$

And the maximum axial stress at the root can be determined by:

$$\sigma_{\text{max,long}} = \frac{F_{\text{top}} + F_{\text{beam}}}{A} \tag{F.15}$$

Buckling Performance

A pure cantilever ($K = 2$) Euler buckling approximation is used to determine the critical buckling load:

$$P_{cr} = \frac{\pi^2 EI}{(KL)^2} \tag{F.16}$$

with E the Young's modulus, I the moment of inertia, K the Euler factor, and L the length of the beam. The critical buckling factor can then be determined by:

$$\text{Buckling Factor} = \frac{P_{cr}}{F_{top} + F_{beam}} \tag{F.17}$$

which assumes pure axial compressions, only global Euler bending modes, perfect geometry, constant EI, and no shell effects. These underlying assumptions can differ from FEM approaches.

Lateral Performance

The beams are considered cantilever beams subjected to a lateral force, allowing for the resulting bending moment to be determined by:

$$M = F \cdot L \tag{F.18}$$

with the maximum momentum defined by:

$$M_{max} = F_{top}L + \frac{wL^2}{2} \tag{F.19}$$

for which the bending stress is:

$$\sigma_{lat} = \frac{My}{I} \tag{F.20}$$

where y is the outer most fibre, in this case defined by $y = \frac{200[\text{mm}]/1000}{2}$. The lateral displacement can then be given by:

$$\delta_{lat} = \frac{F_{top}L^3}{3EI} + \frac{wL^4}{8EI} \tag{F.21}$$

which assumes pure bending and a rigid cross-section and does not account for local wall bending, shear deformation, or stress concentrations.

Eigenfrequency

The effective mass can be determined by:

$$m_{eff} = m_{top} + \frac{33}{140}m_{beam} \tag{F.22}$$

where the factor $\frac{33}{140}$ represents the modal mass participation of the first bending mode of a cantilever beam. The natural circular frequency is then given by:

$$\omega_n = \sqrt{\frac{3EI}{m_{eff}L^3}} \tag{F.23}$$

and the first eigenfrequency follows as:

$$f_1 = \frac{\omega_n}{2\pi} \tag{F.24}$$

G
Analytical Concept Generation

This appendix shows the analytical approximations, assessments, and assumptions used in the early conceptual design. An extended `Python Code` based on the general process described in this appendix has been used to obtain initial design parameters, which are material and cross-section specific. This appendix is complementary to the explanation given in section 4.3.

1. Evaluate eight individual circular beams under the combined loading conditions corresponding to the aerodynamic and end-of-flight launch phases.
2. Assess compressive stresses by comparing the induced stresses with the compressive strength of the selected material.
3. Evaluate Euler buckling by comparing the applied compressive load with the critical buckling load.
4. Iteratively introduce support rings to reduce the effective buckling length until the buckling requirement is satisfied.
5. Verify that the resulting slenderness ratio is still within the validity regime of the Euler buckling approximation.
6. Re-evaluate the longitudinal, lateral, and buckling performance of the now supported structure.
7. If the longitudinal requirements are satisfied, but lateral stiffness is still insufficient, two additional support structures are evaluated, taking note of their added mass.
   - **Diagonal support beams** are introduced between the primary beams and the support rings. These are approximated as equivalent spring elements, where only the lateral stiffness contribution of these diagonal members are considered.
   - **Thin-sheet enclosure** consisting of a 2 mm cylindrical shell surrounding the beam structure, providing additional global lateral stiffness.
8. Discard any configurations that do not satisfy the launch requirements regarding the quasi-static loads.
9. Repeat procedure for outer beam diameters between 50 and 300 mm. Wall thicknesses between 0.5 and 10 mm are considered for Al-7075-T6 and C/C-SiC, while thicknesses between 1.0 and 10 mm are considered for CFRP and CF/PEEK.
10. Compare the valid configurations based on the structural mass.
11. Select the configuration with the lowest mass that survives the launch loads, providing the outer diameter, wall thicknesses and mass estimates.

Geometry and Baseline Mechanics

The main spacecraft framework consist of N_{beams} longitudinal thin-walled columns, distributed symmetrically across an octagonal shape characterised by a corner-to-corner radius R_{st}. Each beam is characterised by an outer diameter D and a wall thickness t, which define the local cross-sectional area A and moment of inertia I.

Global Structural Stiffness

The general area moment of inertia for an unreinforced framework consisting of these thin-walled columns can be defined using the parallel axis theorem:

$$I_{\text{global, base}} = N_{\text{beams}} \left(I + A \cdot R_{\text{st}}^2 \right) \tag{G.1}$$

The structure can be divided in an arbitrary number of segments along the total length L_{st}, depending on the number of added support rings, n_{rings}, that connect individual beams together:

$$n_{\text{segments}} = \begin{cases} 1 & \text{if } n_{\text{rings}} = 0 \\ 2 & \text{if } n_{\text{rings}} \in \{1, 2\} \\ n_{\text{rings}} & \text{if } n_{\text{rings}} \geqslant 3 \end{cases}$$

where individual segment length can be determined by:

$$L_{\text{seg}} = \frac{L_{\text{st}}}{n_{\text{segments}}} \tag{G.2}$$

Lateral Support Options

Depending on the load cases, the optimization loop has the choice between three distinct lateral reinforcement options; none, diagonal columns, and enclosing skin structure. These options have effect on the global inertia I_{global}.

1. **Option 'none':** No additional reinforcement structures.

$$I_{\text{global}} = I_{\text{global, base}} \tag{G.3}$$

2. **Option 'diagonal columns':** Eight diagonal trusses are mapped along the outer chord width W_{panel} of the perimeter:

$$W_{\text{panel}} = 2R_{\text{st}} \sin\left(\frac{\pi}{N_{\text{beams}}}\right) \tag{G.4}$$

where the length L_{diag} and orientation angle θ_{diag} of these diagonals are modelled as:

$$L_{\text{diag}} = \sqrt{L_{\text{seg}}^2 + W_{\text{panel}}^2} \tag{G.5}$$

$$\theta_{\text{diag}} = \tan^{-1}\left(\frac{L_{\text{seg}}}{W_{\text{panel}}}\right) \tag{G.6}$$

The equivalent lateral stiffness contribution of the truss structure $k_{total,diag}$ is derived from the individual axial member stiffness:

$$k_{\text{diag}} = \frac{E \cdot A}{L_{\text{diag}}} \tag{G.7}$$

$$k_{\text{total, diag}} = 8 \cdot k_{\text{diag}} \sin^2(\theta_{\text{diag}}) \tag{G.8}$$

Approximating the global framework as an equivalent cantilever structure under a tip loading, the truss stiffness is converted into an equivalent area moment of inertia increment:

$$I_{\text{global}} = I_{\text{global, base}} + \frac{k_{\text{total, diag}} \cdot L_{\text{st}}^3}{3E} \tag{G.9}$$

3. **Option 'enclosing skin structure':** An external thin-film skin of thickness t_{skin} is wrapped around the main radius R_{st}, adding additional inertia of this thin-walled tube:

$$I_{\text{tube}} = \pi \cdot R_{\text{st}}^3 \cdot \left(\frac{t_{\text{skin}}}{1000}\right) \tag{G.10}$$

$$I_{\text{global}} = I_{\text{global, base}} + I_{\text{tube}} \tag{G.11}$$

Launch Environment and Load Cases

The design must be able to survive multiple flight phases, of which the two most critical phases are the *Aerodynamic Phase* and *End-of-Flight Phase*, both characterised by a combined axial (a_{long}) and lateral (a_{lat}) acceleration. These accelerations are scaled by a global factor of safety, FoS, which is 2.0 in the case of composite materials according to (ECSS [49]):

$$a_{\text{long, case}} = a_{\text{long}} \cdot \text{FoS} \cdot g \tag{G.12}$$

$$a_{\text{lat, case}} = a_{\text{lat}} \cdot \text{FoS} \cdot g \tag{G.13}$$

The load cases evaluated during the search for design parameters are aligned with the load cases summarised in Table 4.1 and Table 5.1.

The total structural and payload mass m_{st} translates into the following global force resultants for each individual load case:

- **Compressive Axial Force per Beam Column:**

$$F_{\text{beam, case}} = \frac{a_{\text{long, case}} \cdot m_{\text{st}}}{N_{\text{beams}}} \tag{G.14}$$

- **Global Bending Moment Resultant:** Investigated at the mounting interface where the structure meets the spacecraft bus:

$$M_{\text{global, case}} = \frac{(a_{\text{lat, case}} \cdot m_{\text{st}}) \cdot L_{\text{st}}}{2} \tag{G.15}$$

Combined Loading Assessment

During the real launch, a simultaneous combined loading will occur, where both the axial and lateral accelerations will be applied. Structural validation then shifts from isolated load case limits to coupled load cases and beam-column interaction relations.

Superposition of Stresses

The nominal axial compressive stress (σ_{axial}) is uniformly distributed across the main beams, while the global bending moment introduces a linear flexural stress distribution (σ_{bending}) across the structure's radius:

$$\sigma_{\text{axial}} = \frac{F_{\text{beam, case}}}{A} \tag{G.16}$$

$$\sigma_{\text{bending}} = \frac{M_{\text{global, case}} \cdot R_{\text{st}}}{I_{\text{global}}} \tag{G.17}$$

To account for sign-dependency of asymmetric loading, the stress values are verified on both extreme edges of the global cross-section:

$$\sigma_{\text{compression\_side}} = \sigma_{\text{axial}} + \sigma_{\text{bending}} \tag{G.18}$$

$$\sigma_{\text{tension\_side}} = \sigma_{\text{bending}} - \sigma_{\text{axial}} \tag{G.19}$$

Material yielding constraints dictate that the maximum localized stresses must remain below the allowable yield threshold:

$$\sigma_{\text{compression\_side}} \leqslant \sigma_{\text{compression}} \tag{G.20}$$

$$\sigma_{\text{tension\_side}} \leqslant \sigma_{\text{tension}} \tag{G.21}$$

Beam-Column Buckling Stability

To evaluate structural stability under coupled axial compression and bending moments, the individual columns are checked using the interaction ratio that includes the Euler buckling capacity. The effective length, L_{eff}, of the critical segment depends on the support ring spacing:

$$L_{\text{eff}} = \begin{cases} K_{\text{free}} \cdot L_{\text{st}} & \text{if } n_{\text{rings}} = 0 \\ \max\left(K_{\text{supported}} \cdot \dfrac{L_{\text{st}}}{2},\ K_{\text{free}} \cdot \dfrac{L_{\text{st}}}{2}\right) & \text{if } n_{\text{rings}} = 1 \\ K_{\text{supported}} \cdot \dfrac{L_{\text{st}}}{2} & \text{if } n_{\text{rings}} = 2 \\ K_{\text{supported}} \cdot \dfrac{L_{\text{st}}}{n_{\text{rings}}} & \text{if } n_{\text{rings}} \geqslant 3 \end{cases} \tag{G.22}$$

The critical Euler buckling load, P_{cr}, is defined as:

$$P_{\text{cr}} = \frac{\pi^2 \cdot E \cdot I}{L_{\text{eff}}^2} \tag{G.23}$$

The stability check requires that the combined action of axial force and bending stress satisfies the following beam-column interaction inequality:

$$\text{Interaction Ratio (IR)} = \frac{F_{\text{beam, case}}}{P_{\text{cr}}} + \frac{\sigma_{\text{bending}}}{\sigma_{\text{compression}}} \leqslant 1.0 \tag{G.24}$$

Grid-Search Optimization Logic

The optimizer maps out a predefined continuous parameter space spanning outer diameters ($D \in [50, 300]$ mm) and wall thicknesses ($t \in [1, 10]$ mm).

Objective Function Formulation

The optimization objective is to identify a design vector including D, t, and the number of support rings / structures that minimizes the total structural mass M_{total}. Which is defined by the sum of longitudinal beams, support rings, additional lateral support structures.

$$\min_{D,t} \quad M_{\text{total}} = m_{\text{beams}} + m_{\text{rings, total}} + m_{\text{lateral}} \tag{G.25}$$

Where the individual masses are computed directly from the material density, ρ, and the geometry:

$$m_{\text{beams}} = \rho \cdot N_{\text{beams}} \cdot A \cdot L_{\text{st}} \tag{G.26}$$

$$m_{\text{rings, total}} = n_{\text{rings}} \cdot \rho \cdot A \cdot L_{\text{ring\_perimeter}} \tag{G.27}$$

$$L_{\text{ring\_perimeter}} = \begin{cases} 2\pi R_{\text{st}} & \text{if section\_type} = \text{"circular"} \\ 2R_{\text{st}} \cdot N_{\text{beams}} \sin\left(\dfrac{\pi}{N_{\text{beams}}}\right) & \text{if section\_type} = \text{"octagonal"} \end{cases} \tag{G.28}$$

$$m_{\text{lateral}} = \begin{cases} 0 & \text{if lateral\_opt} = \text{'none'} \\ 8 \cdot A \cdot \rho \cdot L_{\text{diag}} \cdot n_{\text{segments}} & \text{if lateral\_opt} = \text{'diagonal'} \\ \rho \cdot 2\pi R_{\text{st}} \cdot \left(\dfrac{t_{\text{skin}}}{1000}\right) \cdot L_{\text{st}} & \text{if lateral\_opt} = \text{'skin'} \end{cases} \tag{G.29}$$

Algorithmic Filtering Sequence

For each design pair $(D_{\text{try}}, t_{\text{try}})$, the code evaluates constraints using the following logic:

1. Execute baseline check to identify the minimum required ring count (n_{rings}) and the lightest viable lateral reinforcement option (lateral_opt) under nominal loading.
2. Calculate the cross-section geometry (A, I) and apply the parallel axis theorem to determine the total structure stiffness (I_{global}).
3. loop through both flight phases and for each phase, compute the specific loading conditions ($F_{\text{beam, case}}, M_{\text{global, case}}$).
4. Compute combined stresses on the compression side ($\sigma_{\text{compression\_side}}$) and tension side ($\sigma_{\text{tension\_side}}$).
5. Compute the Euler buckling capacity (P_{cr}) and evaluate the beam-column stability interaction ratio (IR).
6. If any phase exceeds the material strength limits ($\sigma_{\text{compression}}, \sigma_{\text{tension}}$) or exceeds an interaction index of 1.0, the current geometry is deemed infeasible and discarded. The code moves to the next pair.
7. If the candidate configuration satisfies all constraints across both load cases, its total mass (M_{total}) is compared against the current global minimum mass configuration. If the current candidate has lower mass than the previous best, it replaces the design vector.

The final output represent a first-order approximation of the optimal lightweight structural configuration that meets the material strength and geometric stability requirements across the two critical launch phases.

H
C/C-SiC Material Property Determination

This appendix describes the procedure used to determine the orthotropic material properties of C/C-SiC to obtain a full FEM compatible material definition. The study done by (Koutsounanos [38]) provides a comprehensive list of measured material properties, but not all parameters required for the COMSOL software. Therefore, the missing material properties are estimated using an additional study by (Ullah et al. [51]). The methodology in this appendix shows the assumptions and scaling done to obtain the final material properties as summarized in Table 4.2.

Table H.1: C/C-SiC material properties as reported by (Koutsounanos [38]), based on collaborative investigation of Arceon's material and based on LSI processed material.

Property	Unit	Value
Density	kg/m^3	1900 – 2000
Porosity	%	2 – 5
Tensile Strength	MPa	80 – 190
Failure Strain	%	0.15 – 0.35
Shear Strength	MPa	55 – 60
Young's Modulus	GPa	50 – 70
Compression Strength	MPa	210 – 320
Flexural Strength	MPa	160 – 300
Fibre Volume Content	%	55 – 65
Coefficient of Thermal Expansion $\parallel$	10^{-6}K^{-1}	-1.1 – 4.4
Coefficient of Thermal Expansion $\perp$	10^{-6}K^{-1}	2.1 – 7.0
Thermal Conductivity $\parallel$	W/(m·K)	17.0 – 22.6
Thermal Conductivity $\perp$	W/(m·K)	7.5 – 10.3
Specific Heat Capacity	J/(kg·K)	690 – 1550

Elastic Properties	E11 (MPa)	E22 (MPa)	E33 (MPa)	G12 (MPa)	G23 (MPa)	G31 (MPa)	v12	v13	v23
Case 01 Vf = 0.2	55,700	55,700	48,100	26,500	20,300	20,300	0.261	0.222	0.222
Case 02 Vf = 0.4	57,700	57,700	42,800	31,300	18,500	18,500	0.299	0.216	0.216
Case 03 Vf = 0.6	60,600	60,600	38,300	36,500	16,800	16,800	0.336	0.210	0.210
Case 04 Vf = 0.7	61,800	61,800	39,400	39,000	16,800	16,800	0.369	0.215	0.215
Case 05 Vf = 0.8	63,000	63,000	33,800	41,800	14,900	14,900	0.372	0.202	0.202

Figure H.1: Elastic material properties of the mesoscale model at different fibre volume fractions using the ANSYS material designer module as provided in the study of (Ullah et al. [51]).

As Table H.1 indicates a fibre volume fraction of 55% - 65%, it can be safely assumed that an average volume fraction of 60% can be used as current estimate. Figure H.1 can then be used to scale the missing values to match the values as provided by (Koutsounanos [38]).

$$\frac{E_3}{E_1} = \frac{38300 \text{ MPa}}{60600 \text{ MPa}} \approx 0.632 \qquad \rightarrow \qquad E_3 \approx 0.632\, E_1 \tag{H.1}$$

Which can then be used as a scaling factor to obtain an assumption for E3 when E1 $\approx$ E2 $\approx$ 70 GPa. This would lead to an E3 $\approx$ 44240 MPa.

It is also possible to determine G12 using Poisson's ratio as indicated in Figure H.1, following:

$$G_{12} \approx \frac{E_1}{2(1+\nu_{12})} = \frac{70000 \text{ MPa}}{2(1+0.336)} \approx 26198 \tag{H.2}$$

A similar ratio can then be obtained to determine the remaining shear modulus, as followed:

$$\frac{G_{23}}{G_{12}} = \frac{16800 \text{ MPa}}{36500 \text{ MPa}} \approx 0.460 \qquad \rightarrow \qquad G_{23} \approx 0.460\, G_{12} \tag{H.3}$$

Combining the ratio with the obtained value for G12 allows for approximation of G23 $\approx$ 12051 MPa.

Lastly, the Poisson's ratios can also be determined based on the following expression:

$$\nu_{21} = \nu_{12}\frac{E_2}{E_1} \tag{H.4}$$

Where for this specific case E2 = E1, thus the Poisson's ratios are also the same. The same principle can be applied to determination of the other two Poisson's ratios, resulting in ratios respectively of 0.336, 0.133, and 0.133.

The remaining values for coefficient of thermal expansion and thermal conductivity are provided by (Koutsounanos [38]) and the applied values are summarized in Table 4.2.

I

Supplementary Trade-Off Data

This appendix contains additional data and procedural information on the trade-off process as present in subsection 4.6.2. The tables and scoring system as discussed in this appendix has been used to obtain the trade-off with a high degree of confidence.

Table I.2 shows the criteria that have been used to assess each concept. These are some of the major design drivers and/or requirements. The list is compiled with assessable metrics at this stage of the study, with thermal behaviour for example still missing. This is due to the fact that the thermal behaviour has not been assessed, as this does not provide valuable insights into these 'incomplete' designs. The weights assigned to each criteria are based on importance of the metric, with internal discussions leading to these final weights. A sensitivity analysis on this weight distribution can be concluded based on Table I.4 to Table I.7, indicating that the trade-off is persistently resulting in the same result.

Table I.3 shows the quantitative data belonging to each individual criteria, with a specific scoring system of 1–4. Table I.1 provides a textual definition for the scores. The choice has been made to use a scoring system of 1–4, while in later stages the verification against requirements can be done binary (pass / fail), the focus in this trade-off is mutual comparison between concepts. At the same time, it provides an indication on whether the concepts already satisfy these requirements are not.

Before combining the trade-off definitions with the COMSOL data to create the final trade-off comparison, it is important to note two additional factors. Firstly, a knock-down-factor (KDF) has been applied to the obtained critical buckling factor from the COMSOL data. According to section 8.7.2 of ECSS-E-HB-32-24A, a KDF is a reduction factor applied, for instance, to buckling assessment to account for differences between the real world and the simulated world. The buckling KDF accounts for geometrical imperfections, residual stresses, and simplifications inherent to simulations (boundary conditions, pre-buckling deformations, etc.) (ECSS [78]). A conservative buckling KDF of 0.5 has been applied at this stage, meaning that the obtained COMSOL CBF is multiplied by 0.5 before inserting it into the final trade-off.

Secondly, a KDF has been applied to the material tensile and compressive strength limits, with a KDF of 0.9 for metals and 0.8 for composite materials. This allows for margin between the theoretical material limit and the design allowable limit. This KDF accounts for material imperfections. The tensile and compressive strengths are multiplied by this KDF before the COMSOL data is compared against these material properties for determination of the margin of safety (MoS). The MoS is determined according to ECSS-E-ST-32C Rev.1, section 4.5.16 (ECSS [79]). This section discusses the margin of safety which follows the relation below:

$$MoS = \frac{\text{design allowable load}}{\text{design limit load} \times FOS} - 1 \tag{I.1}$$

Where the loads can be replaced by stresses at this stage, because the load-stress relationship is linear for the current COMSOL assessment. The FOS has already been applied within the loads of COMSOL and should thus not be taken into account a second time at this stage. The design allowable stress is the lowest value of the material's tensile/compressive strength after applying the material KDF. The design limit stress is the obtained stress from COMSOL after applying the loads.

Table I.1: Clarifying definitions of the scoring system of 1 to 4.

Score	Definition
1	Unacceptable
2	Marginally Unacceptable
3	Marginally Acceptable
4	Acceptable

Table I.2: Trade-off criteria for the assessment of different concepts under conditions provided by the launch environment.

Trade-Off Criteria				
Criterion	**Unit**	**Goal**	**Weight**	**Explanation**
Total Structural Mass	kg	Minimize	0.125	The total mass of the structure is one of the primary drivers and indicators of costs and feasibility.
Eight-Beam Volume	m^3	Minimize	0.125	The volume of an individual longitudinal beam indicates how much volume the structure occupies, which is less volume available for collecting area.
Aerodynamic Phase Max Stress / MoS	MPa	Minimize	0.12	The maximum stress during the aerodynamic phase is an indicator of how well the structure performs under a combined acceleration loading.
Aerodynamic Phase Max Displacement	mm	Minimize	0.11	The maximum displacement during the aerodynamic phase is an indicator of how well the structure performs under a combined acceleration loading.
Aerodynamic Phase Critical Buckling Factor	–	Maximize	0.07	The critical buckling factor shows how well the structure is able to resist buckling of the structure, most critical for the load cases with a combined load.
End-of-Flight Phase Max Stress / MoS	MPa	Minimize	0.12	The maximum stress during the end-of-flight phase is an indicator of how well the structure performs under a combined acceleration loading.
End-of-Flight Phase Max Displacement	mm	Minimize	0.11	The maximum displacement during the end-of-flight phase is an indicator of how well the structure performs under a combined acceleration loading.
End-of-Flight Phase Critical Buckling Factor	–	Maximize	0.05	The critical buckling factor shows how well the structure is able to resist buckling of the structure, most critical for the load cases with a combined load.
Longitudinal Eigenfrequency	Hz	20 +	0.05	The longitudinal eigenfrequency is a measure of the structure's response to frequency input. Has to adhere to the launch manual requirements.
Lateral Eigenfrequency	Hz	6 +	0.12	The lateral eigenfrequency is a measure of the structure's response to frequency input. Has to adhere to the launch manual requirements.

Table I.3: Scoring definitions of each criterion, with a scoring system of 4 for each criterion. The definitions have been made quantitative to allow for comparisons based on numerical data from COMSOL simulations. MoS = Margin of Safety. CBF = Critical Buckling Factor

Individual Score Definitions		
Criterion	**Score**	**Definition**
Total Structural Mass	1	> 25 % heavier than the lowest mass.
	2	Within + 15 – 25 % of the lowest mass.
	3	Within + 15 % of the lowest mass.
	4	The lowest structural mass.
Eight-Beam Volume	1	> 25 % more volume than the lowest volume.
	2	Within + 15 – 25 % of the lowest volume.
	3	Within + 15 % of the lowest volume.
	4	The lowest structural eight-beam volume.
Aerodynamic Phase Max Stress / MoS	1	MoS < -0.3
	2	-0.3 < MoS < 0
	3	0 < MoS < 0.3
	4	MoS > 0.3
Aerodynamic Phase Max Displacement	1	Lateral displacement > 150 mm
	2	125 mm < Lateral displacement < 150 mm
	3	100 mm < Lateral displacement < 125 mm
	4	Lateral displacement < 100 mm
Aerodynamic Phase Critical Buckling Factor	1	CBF < 1.5
	2	1.5 < CBF < 2
	3	2 < CBF < 4
	4	CBF > 4.0
End-of-Flight Phase Max Stress / MoS	1	MoS < -0.3
	2	-0.3 < MoS < 0
	3	0 < MoS < 0.3
	4	MoS > 0.3
End-of-Flight Phase Max Displacement	1	Lateral displacement > 150 mm
	2	125 mm < Lateral displacement < 150 mm
	3	100 mm < Lateral displacement < 125 mm
	4	Lateral displacement < 100 mm
End-of-Flight Phase Critical Buckling Factor	1	CBF < 1.5
	2	1.5 < CBF < 2
	3	2 < CBF < 4
	4	CBF > 4.0
Longitudinal Eigenfrequency	1	f_{long} < 15 Hz
	2	15 Hz < f_{long} < 20 Hz
	3	20 Hz < f_{long} < 25 Hz
	4	f_{long} > 25 Hz
Lateral Eigenfrequency	1	$f_{lateral}$ < 4 Hz
	2	4 Hz < $f_{lateral}$ < 6 Hz
	3	6 Hz < $f_{lateral}$ < 8 Hz
	4	$f_{lateral}$ > 8 Hz

Table I.4: Final trade-off table based on metrics defined and discussed in Appendix I and obtained data from COMSOL simulations. Adjusted weights with the aim to investigate sensitivity to weight changes. Focus is less on mass and volume and more on buckling.

Final Conceptual Trade-Off Scores												
			Concept 1		Concept 2		Concept 3		Concept 4		Concept 5	
		Material:	C/C-SiC		M40J/PMT-F33		M55J/PMT-F33		Al-7075-T6		CF/PEEK	
		Support rings:	2	5	3	5	2	5	3	5	3	5
Criterion		Weight	Score		Score		Score		Score		Score	
Total Structural Mass		0.10	1	1	4	4	1	1	1	1	3	3
Eight-Beam Volume		0.10	1		4		1		1		2	
Aerodynamic Phase	MoS	0.12	1	1	1	2	1	2	2	3	2	2
	Max Disp.	0.11	1	4	1	3	1	4	1	1	1	2
	CBF	0.10	3	3	3	3	3	4	1	1	2	3
End-of-Flight Phase	MoS	0.12	1	2	3	4	2	4	4	4	4	4
	Max Disp.	0.10	3	4	3	4	3	4	1	4	2	4
	CBF	0.10	3	4	4	4	4	4	1	1	3	3
Longitudinal Eigenfrequency		0.05	4	4	4	4	4	4	4	4	4	4
Lateral Eigenfrequency		0.10	1	2	1	1	1	2	1	1	1	1
		Total Score:	1.750	2.500	2.690	3.250	1.970	2.960	1.630	2.050	2.330	2.740
			2.125		2.970		2.465		1.840		2.535	

Table I.5: Final trade-off table based on metrics defined and discussed in Appendix I and obtained data from COMSOL simulations. Adjusted weights with the aim to investigate sensitivity to weight changes. Focus is more on mass and volume, equally across frequencies and less on stress and displacements.

Final Conceptual Trade-Off Scores												
			Concept 1		Concept 2		Concept 3		Concept 4		Concept 5	
		Material:	C/C-SiC		M40J/PMT-F33		M55J/PMT-F33		Al-7075-T6		CF/PEEK	
		Support rings:	2	5	3	5	2	5	3	5	3	5
Criterion		Weight	Score		Score		Score		Score		Score	
Total Structural Mass		0.13	1	1	4	4	1	1	1	1	3	3
Eight-Beam Volume		0.13	1		4		1		1		2	
Aerodynamic Phase	MoS	0.10	1	1	1	2	1	2	2	3	2	2
	Max Disp.	0.10	1	4	1	3	1	4	1	1	1	2
	CBF	0.07	3	3	3	3	3	4	1	1	2	3
End-of-Flight Phase	MoS	0.10	1	2	3	4	2	4	4	4	4	4
	Max Disp.	0.10	3	4	3	4	3	4	1	4	2	4
	CBF	0.07	3	4	4	4	4	4	1	1	3	3
Longitudinal Eigenfrequency		0.10	4	4	4	4	4	4	4	4	4	4
Lateral Eigenfrequency		0.10	1	2	1	1	1	2	1	1	1	1
		Total Score:	1.780	2.450	2.830	3.330	1.950	2.820	1.700	2.100	2.400	2.770
			2.115		3.080		2.385		1.900		2.585	

Table I.6: Final trade-off table based on metrics defined and discussed in Appendix I and obtained data from COMSOL simulations. Adjusted weights with the aim to investigate sensitivity to weight changes. Focus is less on mass, volume and frequencies, more on aerodynamic phase.

Final Conceptual Trade-Off Scores												
			Concept 1		Concept 2		Concept 3		Concept 4		Concept 5	
		Material:	C/C-SiC		M40J/PMT-F33		M55J/PMT-F33		Al-7075-T6		CF/PEEK	
		Support rings:	2	5	3	5	2	5	3	5	3	5
Criterion		Weight	Score		Score		Score		Score		Score	
Total Structural Mass		0.09	1	1	4	4	1	1	1	1	3	3
Eight-Beam Volume		0.09	1		4		1		1		2	
Aerodynamic Phase	MoS	0.13	1	1	1	2	1	2	2	3	2	2
	Max Disp.	0.13	1	4	1	3	1	4	1	1	1	2
	CBF	0.13	3	3	3	3	3	4	1	1	2	3
End-of-Flight Phase	MoS	0.10	1	2	3	4	2	4	4	4	4	4
	Max Disp.	0.10	3	4	3	4	3	4	1	4	2	4
	CBF	0.10	3	4	4	4	4	4	1	1	3	3
Longitudinal Eigenfrequency		0.065	4	4	4	4	4	4	4	4	4	4
Lateral Eigenfrequency		0.065	1	2	1	1	1	2	1	1	1	1
		Total Score:	1.855	2.610	2.695	3.285	2.055	3.070	1.625	2.055	2.325	2.785
			2.233		2.990		2.563		1.840		2.555	

Table I.7: Final trade-off table based on metrics defined and discussed in Appendix I and obtained data from COMSOL simulations. Adjusted weights with the aim to investigate sensitivity to weight changes. Focus on critical metrics like MoS (aerodynamic phase), max displacement, lateral frequency, and critical buckling (aerodynamic phase).

Final Conceptual Trade-Off Scores												
			Concept 1		Concept 2		Concept 3		Concept 4		Concept 5	
		Material:	C/C-SiC		M40J/PMT-F33		M55J/PMT-F33		Al-7075-T6		CF/PEEK	
		Support rings:	2	5	3	5	2	5	3	5	3	5
Criterion		Weight	Score		Score		Score		Score		Score	
Total Structural Mass		0.09	1	1	4	4	1	1	1	1	3	3
Eight-Beam Volume		0.09	1		4		1		1		2	
Aerodynamic Phase	MoS	0.14	1	1	1	2	1	2	2	3	2	2
	Max Disp.	0.14	1	4	1	3	1	4	1	1	1	2
	CBF	0.13	3	3	3	3	3	4	1	1	2	3
End-of-Flight Phase	MoS	0.10	1	2	3	4	2	4	4	4	4	4
	Max Disp.	0.10	3	4	3	4	3	4	1	4	2	4
	CBF	0.05	3	4	4	4	4	4	1	1	3	3
Longitudinal Eigenfrequency		0.02	4	4	4	4	4	4	4	4	4	4
Lateral Eigenfrequency		0.14	1	2	1	1	1	2	1	1	1	1
		Total Score:	1.620	2.430	2.410	3.030	1.770	2.900	1.500	1.940	2.100	2.570
			2.025		2.720		2.335		1.720		2.335	

J
Additional Model Visualizations

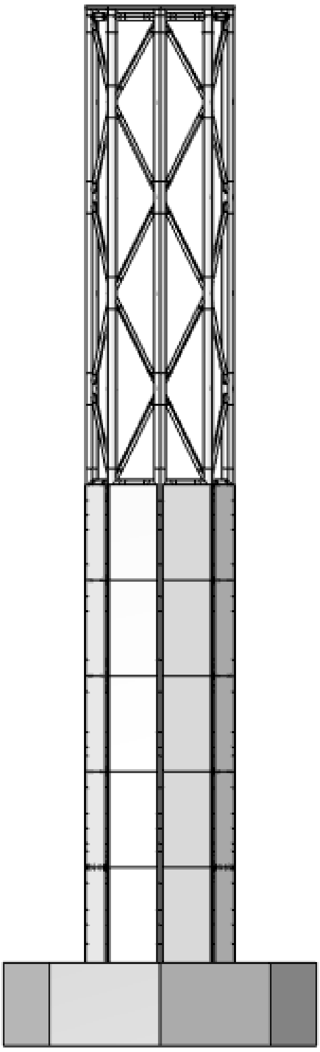

(a) The final structural configuration of the single-octagon structural design, including half mylar and solar panels. SO-HP

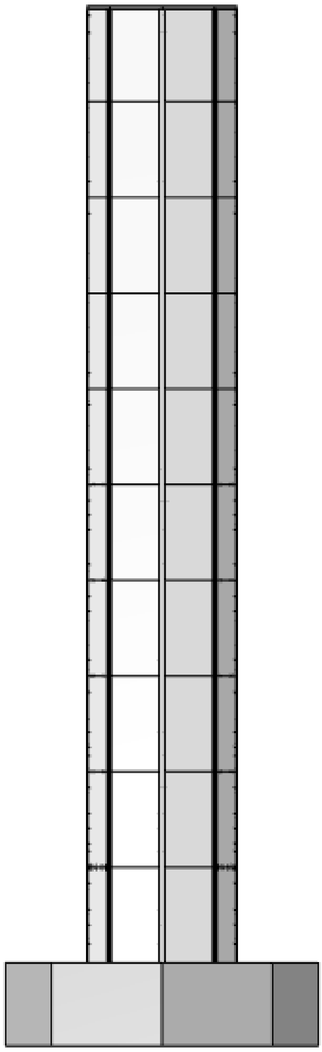

(b) The final structural configuration of the single-octagon structural design, including full mylar and solar panels.

Figure J.1: Two final single-octagon configurations, either including full or half coverage of mylar and solar panels. SO-FP

K
Mesh Convergence Study

To ensure maximum efficiency, a mesh convergence study was done to determine which mesh refinement is sufficient to reach converged results. Implementing the minimum mesh refinement saves unnecessary use of computational resources during simulations.

For this convergence study, the base model of the M40J/PMT-F33 concept with 5 support rings, as shown in Figure 4.6a, was used. Simulations on the launch conditions have been executed for 4 different predefined, by COMSOL, mesh sizes. *Fine*, *Finer*, *Extra Fine*, and *Extremely Fine*. The raw data on stresses, displacement, and critical buckling factors can be seen in Table K.1.

Table K.1: Mesh convergence study performed on the trade-off model of M40J/PMT-F33 with a total of 5 support rings. The mesh sizes are based on predefined mesh refinement within COMSOL.

Mesh Convergence Study									
		Material:	M40J/PMT-F33						
		Mesh Size:	Fine		Finer		Extra Fine		Extremely Fine
		Domain Elem:	1418		4212		7213		11046
		Boundary Elem:	13580		58076		278618		637110
		Edge Elem:	6448		12544		29152		44656
Criterion		Unit	Value	Change	Value	Change	Value	Change	Value
Total Structural Mass		kg	151.74	0.4%	152.31	0.0%	152.33	0.0%	152.33
Eight-Beam Volume		m^3	3.30	0.0%	3.30	0.0%	3.30	0.0%	3.30
Aerodynamic Phase	Max Stress	MPa	247.65	31.7%	326.24	-7.9%	300.40	3.0%	309.42
	Max Disp.	mm	94.62	16.8%	110.46	3.0%	113.76	-0.6%	113.13
	CBF	-	10.92	-24.9%	8.20	-17.9%	6.74	-5.8%	6.35
End-of-Flight Phase	Max Stress	MPa	138.36	31.6%	182.05	-8.0%	167.41	2.4%	171.46
	Max Disp.	mm	52.57	16.7%	61.36	3.0%	63.20	-0.6%	62.85
	CBF	-	16.82	-18.8%	13.66	-14.9%	11.62	-5.9%	10.93
Lateral Eigenfrequency		Hz	3.51	-7.1%	3.27	-1.4%	3.22	0.3%	3.23
		Run Time (s):	156	× 1.7	427	× 5.4	2725	× 11.3	33478

It can be seen that most metrics do not significantly change when going from *Extra Fine* to *Extremely Fine*, with all of them within the 3% convergence acceptance. The only metrics not yet converged are the buckling factors, which still change by +5%, but as this metric is not the most critical at this stage and the time gained by not refining to extremely fine is significant, they are considered acceptable. The run time required for the specific model with extra fine mesh is roughly 45 minutes, which increased to nearly 10 hours for the extremely fine mesh. Later models included an increasing number of support structures and thus elements, making even the *Extra Fine* refinement too heavy for standard hardware. Subsequently, the mesh has been made coarser for quick iterations, with the aim to refine sufficiently when utilizing the DelftBlue High Performance Computer (HPC).

L

CFRP/Aluminium SC Bus Connection

This appendix contains several images, Figure L.1, that visualize a potential design to connect thin-walled circular CFRP beams to a perpendicular aluminium surface. The design has been made based on an arbitrary 1 mm thick CFRP beam, with an outer diameter of 187.2 mm. The red aluminium part has been modelled with a $D = 197.2$ mm, $d = 187.2$ mm, and $h = 350$ mm. Of the height, 80 mm is sunken into the aluminium spacecraft bus. This red component contains 18 holes at 3 different heights for later injection of the adhesive. The pitch of the thread for both parts (red and green) is set to 2.1°, to maximize the threads and thus surface area. The green aluminium part has a $D = 185.2$ mm, $d = 170.0$ mm, and $h = 200$ mm

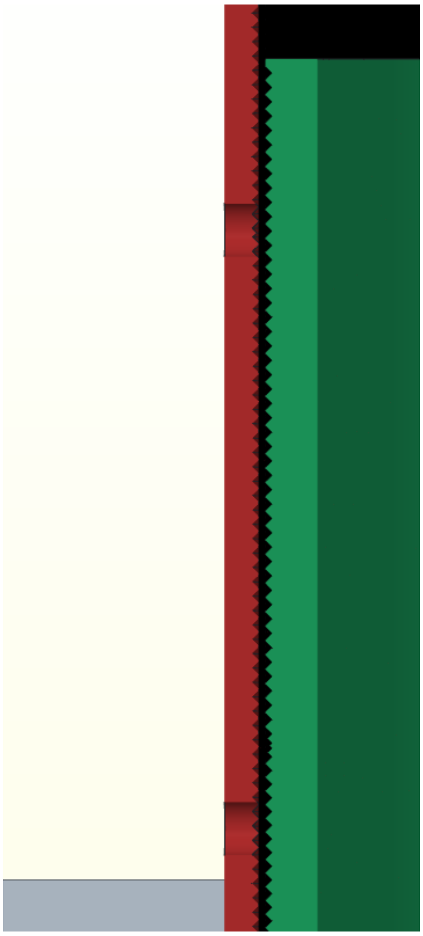

(a) A zoomed image of the CFRP/aluminium connection, depicting clear injections holes and two-way threading.

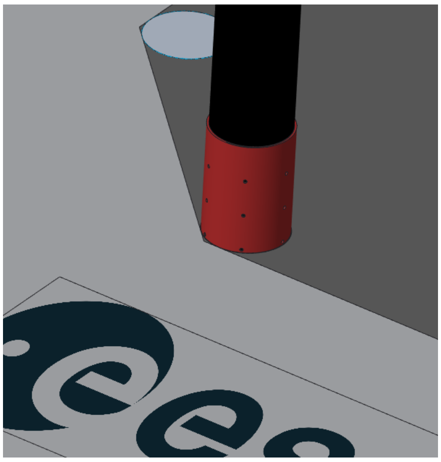

(b) Image of the outside look of the SC bus connection.

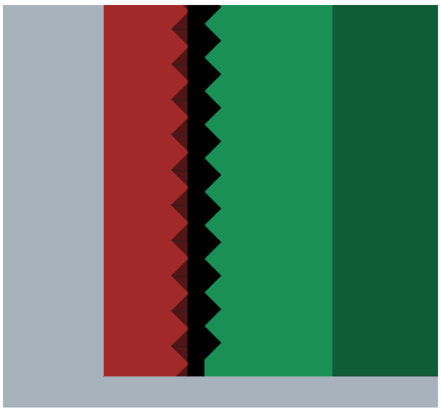

(c) An even more zoomed image of the connection, clearly depicting the available space for the epoxy to fill and adhere to both materials.

Figure L.1: Three images that show a relatively simple design, with arbitrary diameters that should be based on the thickness and diameter of the CFRP beams. The inner/outer surfaces of the aluminium components (red / green) are threaded in two directions, clockwise (CW) and counter-clockwise (CCW).

M
Final Design Parameter Definition

This appendix contains two visualizations of the 'naked' structural designs, without the mylar and solar panels. The images contain parameter identifications and definitions, providing an insight into the parameter values of the structures. Figure M.1a depicts the single-octagon configuration with parameters of the final design, whereas Figure M.1b shows the multi-octagon structure with parameters. The remaining parameters of the multi-octagon structure that are not depicted are therefore the same as in the single-octagon structure.

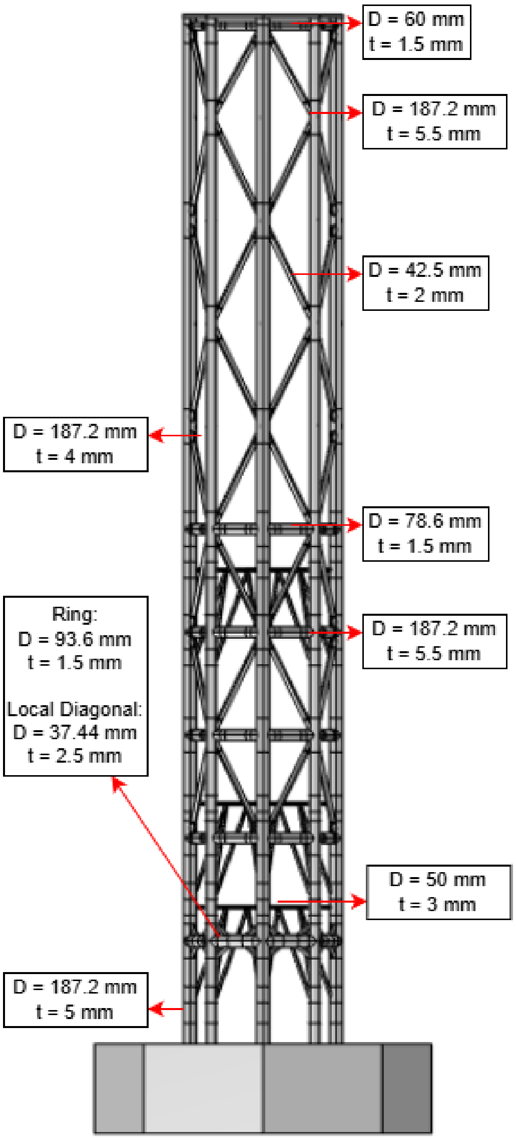

(a) The final single-octagon structure with parameter definitions.

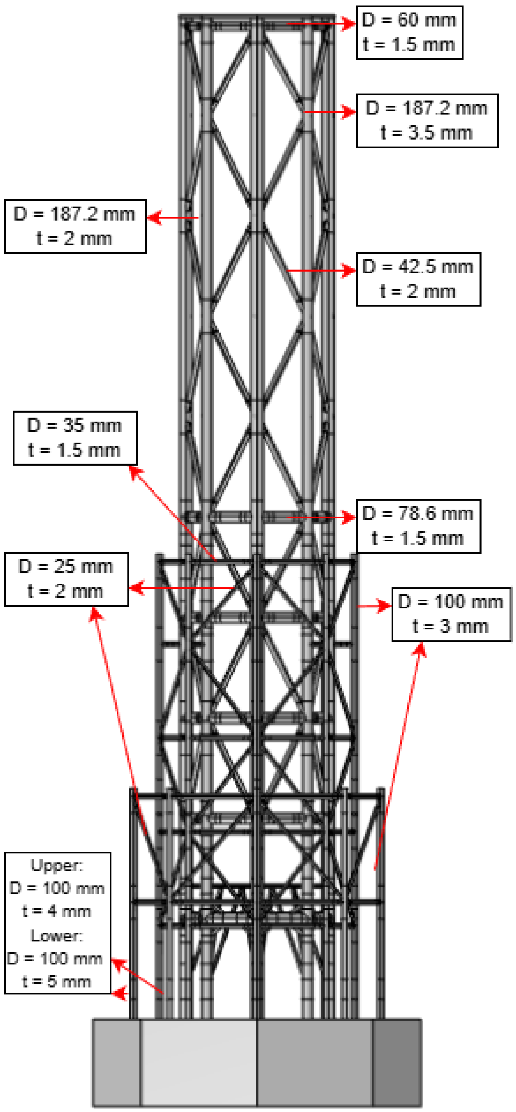

(b) The final multi-octagon structure with parameter definitions.

Figure M.1: The two final bare configurations with parameter locations.

N
Emissivity and Absorptivity Properties

This appendix discusses the derivation and the approximation of thermal properties for the different surface boundaries of the structural model. Some emissivity and absorptivity properties have been found in online sources, while others are approximated to obtain effective properties. A distinction is made between the two spectral bands, solar and ambient, which are separated by the wavelength 2.5μm.

Multi-Layer Insulation (MLI)

To maintain a relatively simple model, the MLI is modelled as a single surface, while in reality the MLI consist of 10 – 50 individual layers, separated by a fine netting. The governing heat flux equation is given by (Kanda, Matsumoto, and Yamaguchi [80]):

$$q = \frac{\sigma\left(T_{in}^4 - T_{out}^4\right)}{\frac{1}{\epsilon_{in}} + \frac{2(N-1)}{\epsilon_{middle}} + \frac{1}{\epsilon_{out}} - N} \tag{N.1}$$

where q is the net radiative heat flux passing through the shielding in W/m^2, σ is the Stefan-Boltzmann constant (5.670×10^{-8} W/(m^{2}K^4), T_{in} & T_{out} the temperatures of the innermost and outermost boundary layers [K], and N the number of physical layers.

Heat transfer inside the MLI is assumed to occur only via radiation and minimal contact between layers.

To accurately model the MLI, it is of importance to know the material of the different layers, the number of layers, and the thermal properties of the respective materials. A common practice is to have an outer layer of aluminized Teflon, an arbitrary number of inner embossed double-aluminized Kapton layers and a single-aluminized innermost layer. The aluminized Teflon FEP has a solar absorptivity of <20% and can thus be assumed to be worst-case 20%. The IR emissivity is 75 – 85% and can thus be assumed 80%. The inner double-aluminized Kapton layers have a solar absorptivity of <0.15% and an IR emissivity of <0.04%. Safe assumptions are thus to implement 0.15% and 0.04%. The inner-most single-aluminized layer has solar absorptivity of <0.45% and an IR emittance of >0.71%. It is safe to assume respective values of 0.45% and 0.71% (Gilmore [66], SQUID3 Space [81], SQUID3 Space [82]).

Based on these values, the equivalent emissivity limit can be determined as follows:

$$\epsilon^* = \frac{1}{\frac{1}{\epsilon_{in}} + \frac{2(N-1)}{\epsilon_{middle}} + \frac{1}{\epsilon_{out}} - N} \tag{N.2}$$

Spacecraft Bus

The bottom of the spacecraft bus can be assumed to act as radiator surface, for which often a coating is used, such as AZ-93 white paint. The bottom surface of the spacecraft bus has been given the absorptivity and emissivity properties of this coating, which dictates an absorptivity of 0.91 and an emissivity of 0.15 (AZ Technology, Inc. [83]).

The remaining exposed surfaces of the spacecraft bus are covered in MLI properties, as these parts of a spacecraft are often insulated for thermal regulation.

Spacecraft Lid

For the spacecraft lid, several options could be considered, but for the sake of simplicity, the lid has been given the properties of aluminium, specifically anodized aluminium. In reality the lid design will be much more detailed and most likely quite different. Additionally, during operation the lid will be opened and thus act thermally different from the current modelling. The anodized aluminium absorptivity and emissivity are respectively 0.27 and 0.76 (Henninger [84]).

Solar Panels

The solar panels are on the outside covered in solar cells, while on the inside are just bare GFRP. To represent the front side properly as a uniform boundary, the solar cell coverage can be implemented to obtain an effective absorptivity. The governing equation is:

$$\alpha_{front,\ eff} = f_{cell} \cdot \alpha_{cell} \cdot (1 - \eta) + f_{gfrp} \cdot \alpha_{gfrp} \tag{N.3}$$

Where f_{cell} is the fractional solar cell coverage, which is assumed to be 0.9 (90%), resulting in the fractional GFRP exposure to be 0.1 (10%). The solar absorptivity of triple-junction GaAs solar cells, α_{cell}, is 0.92 (92%) and the emissivity is 0.85. For bare GFRP, the solar absorptivity of 0.51 is taken, and emissivity of 0.75 (Spectrolab, Inc. [85], Duarte et al. [86]). The electrical efficiency, η is determined to be 35% based on multi-junction GaAs solar cells, a further development of the triple-junction GaAs solar cells. The result is a front side solar absorptivity of $\alpha_{front,\ eff} = 0.5892$.

Similarly, the effective emissivity of the front side solar panels can be determined:

$$\epsilon_{front,\ eff} = f_{cell} \cdot \epsilon_{cell} + f_{gfrp} \cdot \epsilon_{gfrp} \tag{N.4}$$

The effective front side emissivity becomes $\epsilon_{front,\ eff} = 0.816$

CFRP Structure

Based on the dark and non-reflective nature of CFRP, a solar absorptivity of 0.90 was assumed with a thermal emissivity factor of 0.85, which are both acceptable approximations at this stage.

O

First-Order Approximation MLI Effectiveness

This appendix describes the analytical approximation to assess the effectiveness of the MLI heat shield. The assessment quantifies on a first-order basis how much of the incoming solar radiation would penetrate the heat shield. This appendix makes use of the properties and data from Appendix N and subsection 5.5.4.

The calculations are based on a combination of solar panels and MLI. Heat transfer by conduction through MLI, convection, and radiation originating from sources other than the solar panel or the sun are neglected. The focus in this approximation lies on a single solar panel area with an area of 1.5 × 0.8 m.

Symbol	Definition	Unit
S	Incident solar flux	$\mathrm{W/m^2}$
α	Solar absorptivity	–
ε	Thermal emissivity	–
q''	Heat flux	$\mathrm{W/m^2}$
Q	Heat transfer rate	W
T	Surface temperature	K
A	Radiating surface area	$\mathrm{m^2}$
R_{rad}	Radiative resistance	–
N_{gap}	Number of radiative gaps	–
σ	Stefan–Boltzmann constant	$\mathrm{W\,m^{-2}\,K^{-4}}$

This configuration contains the MLI, but also contains solar panels in front of the MLI. The solar radiation does not directly interact with the MLI, but the solar panel absorbs the solar radiation and re-emits it as infrared radiation to the MLI. The absorbed solar flux on the front surface of the solar panel can be calculated using:

$$q''_{\mathrm{abs}} = \alpha_{\mathrm{front}} \cdot S \tag{O.1}$$

where α_{front} is the solar absorptivity of the front surface of the solar panel, 0.5892, which results in:

$$q''_{\mathrm{abs}} = 0.5892 \cdot 1361 \approx 801.9\ \mathrm{W/m^2} \tag{O.2}$$

The absorbed solar radiation is assumed to be emitted from the solar panel towards the MLI. As a first-order approximation, the equilibrium temperature of the solar panel is obtained by equating the absorbed solar radiation to the thermal radiation emitted by the panel.

$$q''_{\mathrm{abs}} = \varepsilon_{\mathrm{front}} \cdot \sigma \cdot T_{\mathrm{panel}}^4 \tag{O.3}$$

where $\varepsilon_{\mathrm{front}}$ is the thermal emissivity of the solar-panel surface (0.816) and σ is the Stefan–Boltzmann constant,

$$\sigma = 5.67 \times 10^{-8}\ \mathrm{W\,m^{-2}\,K^{-4}} \tag{O.4}$$

As a result, the solar panel temperature becomes:

$$T_{\mathrm{panel}} = \left(\frac{q''_{\mathrm{abs}}}{\varepsilon_{\mathrm{front}} \cdot \sigma} \right)^{1/4} \approx 362.84\ \mathrm{K} \approx 89.69\ ^{\circ}\mathrm{C} \tag{O.5}$$

The temperature is then used as the hot side temperature of the radiative resistance network. For this solar panel configuration, the MLI is not exposed to direct solar radiation, thus an additional radiative resistance is present between the rear of the solar panel and the outer MLI layer. The resistance between the rear side of the solar panel and the outer MLI layer is:

$$R_{\text{gap},1} = \frac{1}{\varepsilon_{\text{panel,rear}}} + \frac{1}{\varepsilon_{\text{MLI,outer}}} - 1 \approx 1.583 \tag{O.6}$$

The resistance for the MLI layers is:

$$R_{\text{MLI}} = N_{\text{gap}} \left(\frac{1}{\varepsilon_{\text{MLI},1}} + \frac{1}{\varepsilon_{\text{MLI},2}} - 1 \right) \approx 784 \tag{O.7}$$

The resistance between the innermost MLI layer and the CFRP structure is:

$$R_{\text{gap},2} = \frac{1}{\varepsilon_{\text{MLI,inner}}} + \frac{1}{\varepsilon_{\text{CFRP}}} - 1 \approx 1.585 \tag{O.8}$$

The total radiative resistance for the solar panel and MLI configuration then becomes:

$$R_{\text{total,panel}} = R_{\text{gap},1} + R_{\text{MLI}} + R_{\text{gap},2} \approx 787.168 \tag{O.9}$$

The heat flux that then reaches the CFRP structure can be estimated, assuming T_{CFRP} is 293.15 K:

$$\boxed{q''_{\text{trans,panel}} = \frac{\sigma \left(T_{\text{panel}}^4 - T_{\text{CFRP}}^4 \right)}{R_{\text{total,panel}}}} \tag{O.10}$$

The total heat transferred to the inner structure is obtained by multiplying the heat flux by the considered area, which is a single panel of 1.2 m^2:

$$Q_{\text{trans,panel}} = q''_{\text{trans,panel}} \cdot A \approx \tag{O.11}$$

where the considered area is:

$$A = 1.5 \times 0.8 = 1.2 \text{ m}^2 \tag{O.12}$$

the incident solar flux is:

$$Q_{\text{solar}} = S \cdot A = 1361 \cdot 1.2 \approx 1633 \text{ W} \tag{O.13}$$

and the heat flux transmitted through the MLI is:

$$q''_{\text{trans,panel}} \approx 0.7164 \text{ W/m}^2 \tag{O.14}$$

This results in a total transmitted heat load of:

$$Q_{\text{trans,panel}} \approx 0.72 \cdot 1.2 \approx 0.86 \text{ W} \tag{O.15}$$

The fraction of incident solar power that reaches the inner CFRP structure can be estimated:

$$f_{\text{trans,panel}} = \frac{Q_{\text{trans,panel}}}{Q_{\text{solar}}} = \frac{0.86}{1633} \approx 5.3 \times 10^{-4} \tag{O.16}$$

As a percentage of the incident solar power:

$$\boxed{f_{\text{trans,panel}} \approx 0.053\%} \tag{O.17}$$

Only approximately 0.05% of the incident solar power is estimated to go through the solar panel, MLI, and thus reaches the CFRP structure.

P
Micrometeoroid Impact Plots

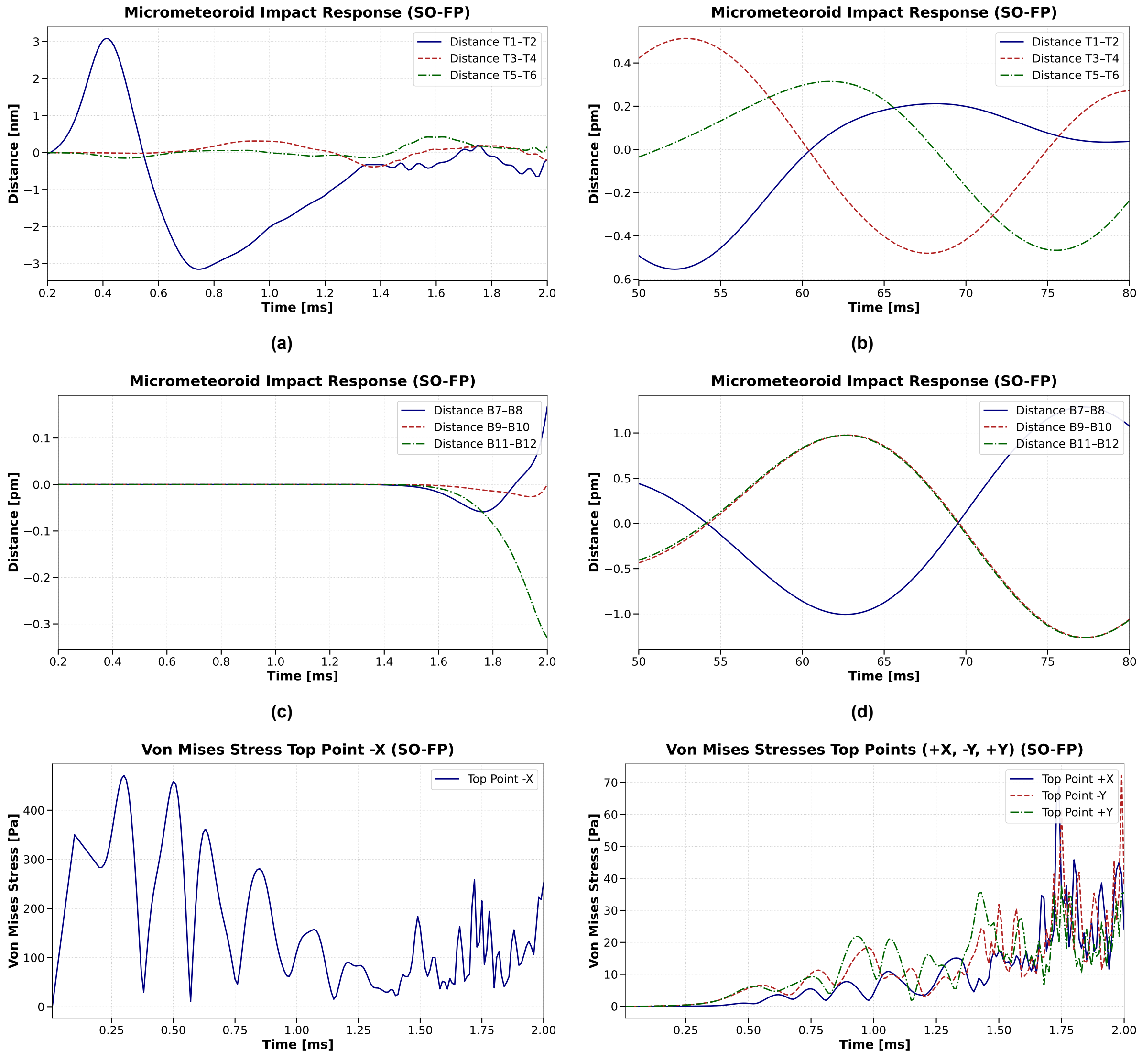

Figure P.1: **a)** Response during time interval 0.2 –2.0 ms of lateral distances between three node pairs at the tip of the spacecraft. **b)** Response during time interval 50 – 80 ms of lateral distances between three node pairs at the tip of the spacecraft. **c)** Response during time interval 0.2 – 2.0 ms of lateral distances between three node pairs at the lower region of the spacecraft. **d)** Response during time interval 50 – 80 ms of lateral distances between three node pairs at the lower region of the spacecraft. **e)** Response during time interval 0.2 – 2.0 ms of von Mises stress at nodal location -X at the tip of the spacecraft. **f)** Response during time interval 50 – 80 ms of von Mises stress at nodal location +X, -Y, and +Y at the tip of the spacecraft.

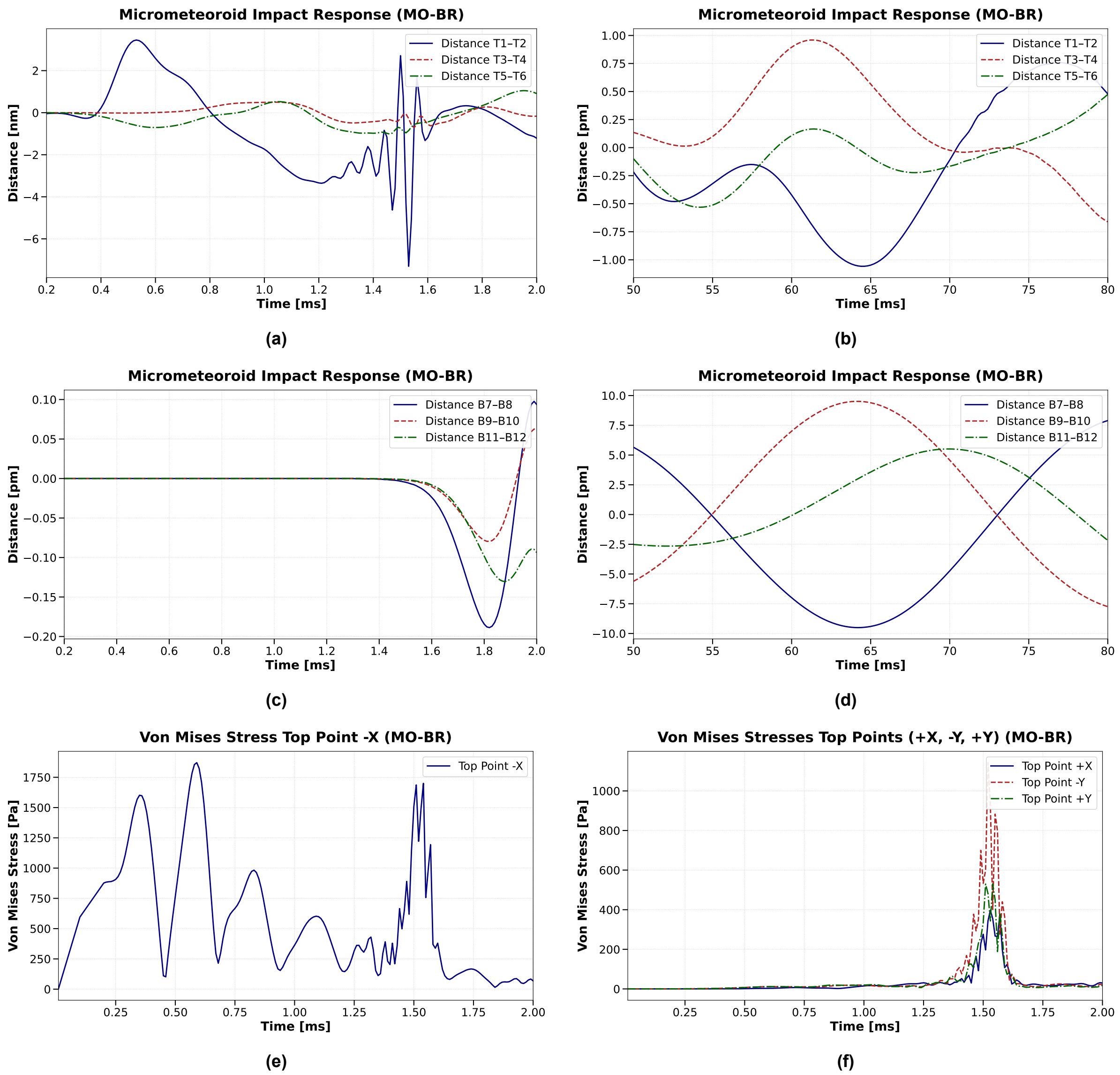

Figure P.2: a) Response during time interval 0.2 –2.0 ms of lateral distances between three node pairs at the tip of the spacecraft. **b)** Response during time interval 50 – 80 ms of lateral distances between three node pairs at the tip of the spacecraft. **c)** Response during time interval 0.2 – 2.0 ms of lateral distances between three node pairs at the lower region of the spacecraft. **d)** Response during time interval 50 – 80 ms of lateral distances between three node pairs at the lower region of the spacecraft. **e)** Response during time interval 0.2 – 2.0 ms of von Mises stress at nodal location -X at the tip of the spacecraft. **f)** Response during time interval 50 – 80 ms of von Mises stress at nodal location +X, -Y, and +Y at the tip of the spacecraft.